The Dissertation Committee for Marina Claudia Geraldina Frederik Certifies that this is the approved version of the following dissertation:

MORPHOLOGY AND STRUCTURE OF THE ACCRETIONARY PRISM OFFSHORE NORTH SUMATRA, INDONESIA AND OFFSHORE KODIAK ISLAND, USA - A COMPARISON TO SEEK A LINK BETWEEN PRISM FORMATION AND HAZARD POTENTIAL

Committee:

Sean P. S. Gulick, Supervisor

James A. Austin, Jr., Co-Supervisor

Nathan L.B. Bangs

Luc L. Lavier

Jaime D. Barnes

Lisa C. McNeill

MORPHOLOGY AND STRUCTURE OF THE ACCRETIONARY PRISM OFFSHORE NORTH SUMATRA, INDONESIA AND OFFSHORE KODIAK ISLAND, USA - A COMPARISON TO SEEK A LINK BETWEEN PRISM FORMATION AND HAZARD POTENTIAL

by

Marina Claudia Geraldina Frederik, B.S., M.S. D.EA., M.S.

Dissertation

Presented to the Faculty of the Graduate School of

The University of Texas at Austin

in Partial Fulfillment

of the Requirements

for the Degree of

Doctor of Philosophy

The University of Texas at Austin

August 2016

Dedication

To my mother and father for their love and constant support

Acknowledgements

Many people have helped me throughout my studies at UT from the beginning until the completion of my dissertation. First of all, I acknowledge my advisor, Sean Gulick, for his dedication, patience and his passion for science. He is truly an excellent mentor and role model. I also acknowledge my co-advisor, James Austin, for his guidance, dedication, attention to detail and excellent writing skills. He taught me to be detail-oriented when writing scientific papers. I am fortunate to have them as my advisors.

My committee members are experts in their fields with busy schedules but always have time for discussion or my questions. I thank Nathan Bangs for serving as a member and appreciate his insights to writing a journal manuscript and his seismic interpretation skills. I thank Luc Lavier for serving as a member and for his support during revisions of my Tectonics paper. I thank Jamie Barnes for serving as a member and for allowing me to serve as TA in her geology classes. I thank Lisa McNeill to serve as a member and as a reviewer for my Tectonics paper. I look forward to working with her in the upcoming IODP 362 Sumatra expedition.

Philip Guerrero in the Jackson School is the best graduate advisor. I thank Philip for his advice and patience answering my questions. Specifically at UTIG, I thank Dan Duncan for always being available to help and discuss bathymetric data challenges. I thank Marcy Davis for always being available to answer Fledermaus questions or other software. Her baked goods are always delicious! I thank Steffen Saustrup for his help in seismic data and Landmark challenges. I thank Dallas Dunlap, undeniably the guru of Landmark. Many thanks to Mark Wiederspahn and John Gerboc, who are ever helpful

and just an email away for my IT situations. I thank John Goff for helping me on GMT scripts and bathymetry interpretations. I thank Nick Hayman who introduced me to the Tenryu Canyon and to whom I can always go for discussions on structural geology. Many thanks to Nancy Hard who is always helpful, cheerful, and friendly; I thank you for your friendship. Thanks to Shuoshuo Han for her advice on my dissertation; Rodrigo Fernandez for his help in bathymetry challenges and advice on my dissertation; Judy Sansom for help on any financial related matter. She is always cheerful and friendly. I thank Rosalind Gamble for always being friendly and helpful. My deep appreciation to all UTIG personnel and graduate students for their attention and kindness while I grieve for the passing of my mother, weeks before my defense.

I thank John Miller from USGS Denver, who took the time to teach me seismic processing using the software ProMAX for the Kodiak area. From BPPT, I thank Yusuf Djajadihardja for introducing me to the world of tsunamigenic earthquakes. Many thanks to Udrekh for his constant support during my five years of study and the various preparation of the upcoming IODP 362 expedition.

Among my fellow graduates, I thank Kylara Martin, who showed me the ropes when I arrived in UT. I thank Bobby Reece, who is always calm in every situation and available to help or discuss science and graduate life. Pinar Gotkas is a wonderful office-mate who also worked on weekends. Maureen Walton is also a great office-mate, always helpful, and a model on working efficiently. Amanda Calle is a delightful friend and office-mate, always helpful and calm. Sebastian Ramirez, who can be serious and funny at the same time, is always available for discussion. Yawen is a wonderful friend, thank you for your friendship. I thank John Swartz, who is always helpful and cheerful.

I thank my Austinite-Indonesian friends, Hannah, Ida, Rita, Elly, Maggie, Lily, Esther, and many more, for their prayers, support and friendship, and the delicious Indonesian food I always look forward to.

Most of all, I want to thank my parents who always believe in me, they are my rock. I am forever in their debt.

Morphology and structure of the accretionary prism offshore North Sumatra, Indonesia and offshore Kodiak Island, USA - A comparison to seek a link between prism formation and hazard potential

Marina Claudia Geraldina Frederik, Ph.D.
The University of Texas at Austin, 2016

Supervisors: Sean P. S. Gulick and James A. Austin, Jr.

Sumatra and Kodiak Islands experienced recent megathrust earthquakes with devastating tsunami; recurrence of large earthquakes is predicted. Studies of the accretionary prism offshore of northern Sumatra, 1-7°N and 92-97°E, reveal a steep outer slope (5-12°), a plateau ~100-120 km wide, and a steep inner slope adjacent to the Aceh Basin. Three primary structural zones are consistent along strike where a predominantly landward vergence zone exists from the deformation front for a distance ~70 km landward. An extended landward vergence zone is not common; for northern Sumatra, a seaward dipping rigid backstop may be the reason, which assists subsequent younger accreted sediment to form the observed zone. The prism toe region shows prominent mass failures presumably related to activation of thrust faults and/or the shaking in response to the 2004 Sumatra-Andaman earthquake (Mw 9.1). These seafloor changes suggest that the 2004 rupture energy reached near the accretionary prism toe. The rigid backstop in the inner wedge together with the suggested dynamic backstop within the outer wedge, and the consolidated sediment on the outer slope form a rigid block dynamically, which

together allows earthquake rupture to propagate under it and farther seaward toward the Sunda Trench, resulting in enhanced tsunami potential. Along the Aleutian Trench offshore of Kodiak Island, 145-155° W and 55-58° N, exist a distinct horizon, associated with the onset of the Surveyor Fan sedimentation along which the preferred zone forms. Most if not all of the sediment beneath this horizon seemed subducted, smoothing the high relief of the subducting plate. Subduction of large-buried seamounts begins with creation of a proto-thrust zone seaward of the existing deformation front. As a seamount reaches the deformation front, steepening of the prism toe occurs by formation of out-of-sequence thrusts. Upon further subduction, a deformation front jump occurs where the outer limit of proto-thrust zone becomes the new deformation front. This study contributes insights to other subduction zones with similar characteristics such as thick incoming sediment, subducting seamounts, and/or recent megathrust events. This study also underlines the need to establish fundamental time series data sets for mitigation efforts in hazard-prone areas.

Table of Contents

List of Tables

List of Figures

Chapter 1: Introduction

This dissertation presents studies of two subduction zones, offshore northern Sumatra, Indonesia and offshore Kodiak Island, Alaska. At both locations, the accretionary prisms are formed from the thick sediment scraped from the subducting oceanic plate, both oceanic plates contain ridges and seamounts, and they recently experienced great earthquakes. During the 1964 Alaska and 2004 Sumatra-Andaman events, each earthquake produced tsunami that devastated surrounding coastal areas.

Chapters 2 and 3 comprised of studies on offshore of northern Sumatra. Chapter 2 utilized the various survey data acquired since the 2004 event, conducted in the effort to better understand this margin. Specific work I conducted in this study is collecting bathymetric data from five surveys, pre-process and manually cleaning those that are raw data, and then merging them. From the merged bathymetric data, I interpret the vergence of the anticlines by comparing the steepness of the slopes. As the seismic data were already processed, I worked on interpretation of each profiles and validation of folds' vergence direction, which I then used to produce the structural zones across the prism. The bathymetric and seismic data help gain insight to the morphology of the wide accretionary prism and infer the structure within the inner wedge. Chapter 2 was published in *Tectonics* in 2015 [*Frederik et al.*, 2015]. Chapter 3 focuses on investigating the deformation that occurred at the toe of the prism using time series bathymetric data from before and after the great earthquake. I cleaned and processed the pre-earthquake bathymetric data and explored methods to better utilize these data (i.e., slope and depth) for seafloor depth differences investigation. Chapter 3 is in the final revision and I plan to submit it for publication this summer to Earth and Planetary Science Letters.

Studies on Sumatra are important to local communities as well as areas that might be affected by the resulting tsunami; large earthquakes have occurred over human history and future ones will happen [*McCaffrey*, 2009; *Sieh et al.*, 2015]. Studies of the 2004 event show that seismogenic rupture may have extended close to the Sunda Trench, likely contributing to the associated large tsunami [*Henstock et al.,* 2006; *Mosher et al.,* 2008; *Gulick et al.,* 2011]. My investigation of northern Sumatra extends these studies suggestions by inferring a rigid inner wedge (backstop); where together with the potential dynamic backstop in the outer wedge and the consolidated sediment on the outer slope may be responsible in advancing the rupture energy closer to the Sunda Trench. Furthermore, using the time series bathymetric data, my study presents seafloor deformations at the prism toe most likely caused by the 2004 Sumatra-Andaman earthquake.

Chapter 4 focuses on extending our understanding of processes associated with the subduction of a deeply buried seamount. Even though the oceanic plates are covered with seamounts and ridges, those buried under thick sediment are not common worldwide. Generally, only those subduction zones located proximal to a large-active submarine fan would result in the subduction of deeply buried seamounts/ridges. Convergence of the Yakutat microplate and Pacific Plate with the North America Plate results in the St. Elias orogeny and Aleutian Trench, respectively. Erosion from this mountain range produces one of the largest submarine fans in the world, the Surveyor Fan. Offshore of Kodiak Island, there have been multiple geology and geophysical surveys since 1970s, mainly with a focus on finding hydrocarbon resources and later for defining the United States Exclusive Economic Zone. I use seismic and drilling data to investigate variation of sediment thickness along the Aleutian Trench and explore seamount subduction processes. I processed some of the seismic lines used in this study to pre-stack depth migration in USGS Denver thanks to the grant I received from GSA; some other data were already processed

and published by USGS. I interpreted the seismic profiles and correlated horizon ages from more recent drill sites, updating those published in the 1970s and 1980s. The manuscript derived from chapter 4 is still in revision and I plan to submit it for publication in Summer 2016 as well. The writing of chapters 2 to 4 into publication material were assisted by my supervisor, co-supervisor, and co-authors.

Chapter 5 presents my conclusions based on these three studies and the role of future investigations. Offshore of Kodiak and northern Sumatra are similar due to the presence of accretionary prism formed from thick sediment and that both experienced recent major earthquake. The dissimilarity may be the sediment properties of the incoming sediment since there is no drilling expeditions offshore northern Sumatra. Compared to northern Sumatra's 2004 earthquake where the rupture may have extended all the way to the Sunda Trench, the Alaska's 1964 may not have extended to the Aleutian Trench [*Plafker*, 1969; *Finn et al.*, 2015; *Haeussler et al.*, 2015]. For future investigation offshore northern Sumatra, study of the sediment properties covering the Indo-Pacific Plate is important in understanding the significance of the sediment in the development of the Sunda accretionary prism. In August-October 2016, IODP 362 will conduct a drilling expedition in the effort to gain insight for the incoming sediment properties and I will serve as a member of the science party to study these physical properties.

Chapter 2: What 2D Multichannel Seismic and Multibeam Bathymetric Data Tell Us about the North Sumatra Wedge Structure and Co-seismic Response[1]

Abstract

Recent large earthquakes have prompted studies to reevaluate seismicity and rupture propagation behavior along the world's major subduction margins. Our study area covers the entire forearc from northwest of northern Sumatra, to west of Simeulue Island; the southern portion of the 2004 tsunamigenic earthquake rupture zone. The accretionary prism width is up to ~180 km; water depths between ~4.5 km near the Sunda Trench and <1 km on forearc high. The wedge consists of a steep outer slope (5-12°), a plateau ~100-120 km wide with anticlinal folds spaced 2-15 km apart, and a steep inner slope adjacent to the Aceh Basin. Analysis of seismic profiles and bathymetry reveal three main structural zones consistent along-strike, from the trench landward: 1) predominantly landward-vergent folds, 2) mixed vergent folds and 3) predominantly seaward- vergent folds. This paper uses those zones to propose a geometry of an underlying rigid backstop. This backstop is seaward dipping and extends from under the Aceh Basin to beneath the mixed vergence zone. A dynamic backstop possibly exists seaward of the rigid backstop, and is responsible for the steep slope of the outer prism. Indurated accreted sediments form the landward-vergence zone. Along with the possible dynamic backstop beneath the outer wedge, and the rigid backstop in the inner wedge, all behave as a solid block co-seismically. This block allows great earthquake rupture to propagate farther seaward toward the Sunda Trench, with resultant hazardous tsunamigenic potential.

[1] Frederik, M.C.G., S.P.S. Gulick, J.A. Austin Jr., N.L.B. Bangs, and Udrekh (2015), What 2-D multichannel seismic and multibeam bathymetric data tell us about the North Sumatra wedge structure and coseismic response, *Tectonics*, 34, doi:10.1002/2014TC003614. Marina's contributions are collect, clean and merge bathymetric data from various surveys, interpret the merged bathymetric data, interpret seismic profiles, and write the manuscript. The co-authors assist in writing of the manuscript.

2.1. Introduction

Most major earthquakes occur along subduction zones and are capable of producing devastating effects, such as tsunamis, as demonstrated by the 2011 Tohoku (~Mw 9.0) and the 2004 Sumatra-Andaman (~Mw 9.1) events. For both of these great earthquakes, a growing number of studies show that seismogenic rupture may have extended close to the trench, likely contributing to the associated large tsunamis. For example, using bathymetric differences recorded between 1999 and 2011, *Fujiwara et al.* [2011] have observed the location of maximum slip for the Tohoku event to be at the Japan Trench, in agreement with slip model [*Pollitz et al.*, 2011]. For northern Sumatra, slip distribution models [*Ammon et al.*, 2005; *Rhie et al.*, 2007] have suggested the displacement also extended towards the Sunda Trench. Therefore, understanding the geophysically observable morphology and structure of an accretionary prism, such as that near the rupture zone of the 2004 Aceh-Andaman event, should help us understand updip rupture propagation during great earthquakes.

Off western Sumatra, the Indian and Australian plates are subducting under the Sunda Block (Fig. 2.1). For Northern Sumatra, the rate of convergence is 50-55 mm/yr [*Prawirodirdjo et al.*, 2000; *McNeill and Henstock*, 2014]. Subduction started with northward movement of the Indian Plate ~100 Ma [*Sclater and Fisher*, 1974; *Molnar and Tapponnier*, 1975]. Influx of Bengal and related Nicobar Fan sediments started during the late Miocene-Pliocene [*Curray and Moore*, 1971]; accretionary wedge formation offshore Sumatra began in the late Miocene [*Curray and Moore*, 1974]. The major source of sediment forming the accretionary prism offshore of northern Sumatra is the Nicobar Fan. However, since the late Pliocene or Pleistocene, the availability of Nicobar Fan sediments may have been restricted by the Ninetyeast Ridge topographic barrier [*Karig et al.*, 1979].

On December 26, 2004, a magnitude ~9.1 earthquake occurred offshore northern Sumatra; its rupture zone extended along a major portion of the subduction zone from Sumatra (Fig. 2.1) to the Andaman Islands [*Ammon et al.*, 2005; *Ishii et al.*, 2005; *Rhie et al.*, 2007]. This great earthquake produced a large tsunami that affected countries neighboring the Indian Ocean and killed over 200,000 people [*Sibuet et al.*, 2007; *Graindorge et al.*, 2008]. The rupture began at a depth of ~50 km and covered an area of ~1,250 x 150 km (187,500 km^2) [*Ammon et al.*, 2005; *Ishii et al.*, 2005; *Banerjee et al.*, 2007; *Rhie et al.*, 2007]. Three months later, in March 2005, another great earthquake (~ Mw 8.7, rupture area ~40,000 km^2) occurred south of the epicenter of the 2004 rupture [*Banerjee et al.*, 2007]. This earthquake did not produce a large tsunami [*Geist et al.*, 2006].

This paper extends our knowledge of the structure and morphology of the accretionary wedge offshore of northern Sumatra, using 2D multichannel seismic (MCS) profiles and a synthesis of multibeam bathymetric data. These results lead us to propose a new geometry of a rigid backstop forming the core of this part of the accretionary wedge, with implications for its seismogenic behavior.

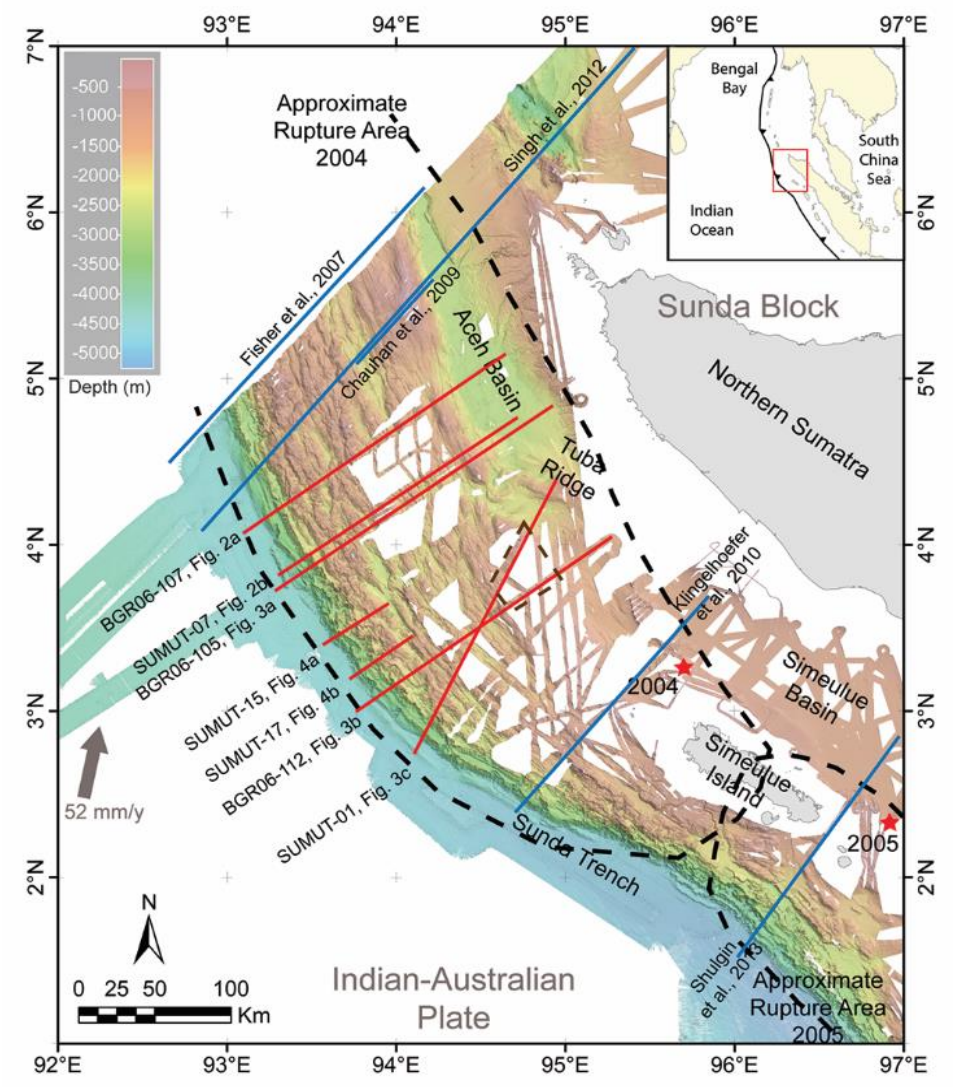

Figure 2.1: Bathymetric and seismic coverage used for this investigation. MCS (red) tracklines superimposed on bathymetric data merged from various sources (Table 2.1). The color bar indicates seafloor depths in meters. The bathymetric data show the complex surficial structural fabric of the accretionary wedge. Red stars denote epicenters of 2004 and 2005 great earthquakes and black dashed lines show associated rupture areas [Briggs *et al.*, 2006]. Brown dashed trapezium shows region of topographical high (Figures 2.3b and 2.3c). Our structural analysis focuses on seven MCS profiles (red lines), labeled from north to south: BGR06-107, SUMUT-07, BGR06-105, SUMUT-15, SUMUT-17, BGR06-112 and SUMUT-01. Blue lines are seismic profile studies published by indicated authors. See the text for details.

2.2. Study Area and Previous Work

Our study area, located between 1-7°N and 92-97°E, extends over the entire forearc, from northwest of northern Sumatra to west of Simeulue Island (Fig. 2.1). The accretionary wedge within our study area is up to ~180 km wide [*Fisher et al.*, 2007], with seafloor depths ranging from ~4.5 km near the Sunda Trench [*Gulick et al.*, 2011] to <1 km on the forearc high proximal to the Aceh (forearc) Basin. The wedge narrows to ~125 km southward around Simeulue Island. This accretionary prism is characterized by complex structures, including both seaward- and landward-vergent thrust zones and piggyback basins with growth strata [*Karig*, 1977; *Henstock et al.*, 2006; *Sibuet et al.*, 2007; *Graindorge et al.*, 2008].

Landward vergence of folded sediments in subduction zones is not generally observed, although such vergence occurs in the Cascadia, southwest Alaska, southwest Japan and northern Panama convergent margins [*Moore and Allwardt*, 1980; *Byrne and Hibbard*, 1987; *Reed et al.*, 1990; *MacKay et al.*, 1992; *Gulick et al.*, 1998]. Landward-vergent structures may form as a result of a seaward-dipping lithification front within the accretionary wedge, or by both the presence and geometry of older, accreted, indurated sediments [*Byrne and Hibbard*, 1987]. Other suggestions for landward vergence have included: low basal shear stress, a young subducting plate, high sedimentation rate, and a low/medium rate of convergence [*Seely*, 1977; *MacKay*, 1995; *Wang and Davis*, 1996; *Gulick et al.*, 1998; *Gutscher et al.*, 2001].

Coulomb wedge theory has been used to show that accretionary wedges at critical state have seafloor slope angles and dip angles of the basal shear plane that are a function of wedge interior strength and basal shear stress [*Davis et al.*, 1983; *Wang and Hu*, 2006]. Offshore of northern Sumatra, the outer slope dip is 1.2°-1.8° [*McNeill and Henstock*, 2014] and the basal dip is 3°-5° [*Singh et al.*, 2012], suggesting that this wedge

is in a subcritical state [*Davis et al.*, 1983]. A subcritical wedge will deform internally to form a steeper taper, but not slide along its base until it achieves a critical state. Conversely, within 50 km from deformation front, the slope angle is 3.3°-3.9° [*McNeill and Henstock*, 2014], which suggests that the taper there is in a critical state [*Davis et al.*, 1983]. For a wedge with continuing accretion at the toe, which is true for northern Sumatra, such a critical state means that the wedge is always deforming internally and sliding along its base to maintain its critical taper.

Other studies have proposed a strong wedge interior off northern Sumatra from observation of shallow thrust faults near the deformation front [*Mosher et al.*, 2008] and extended landward-vergent fold structures, suggestive of both thick and indurated incoming sediment [*Karig*, 1977; *Henstock et al.*, 2006; *Dean et al.*, 2010; *Gulick et al.*, 2011]. Several seismic studies have attempted to map the wedge interior, proposing the existence of backstops of varying geometry. For example, *Chauhan et al.* [2009] and *Singh et al.* [2012] (Fig. 2.1) have interpreted a backthrust which they argue formed the seaward edge of a backstop. This proposed backthrust extends seaward from the western edge of the Aceh Basin, following the ~5 km/s velocity contour at ~4 km depth, before deepening to cross a 6 km/s velocity region at ~18 km depth. Farther southeast, *Klingelhoefer et al.* [2010] (Fig. 2.1) proposed a backstop under the Simeulue Basin on the basis of seismic velocity. They contend that a velocity of 6.3 km/s at ~6 km depth defines the proposed backstop roof, while a 6.8 km/s region at ~21 km depth defines its base. Around Simeulue Island, *Tang et al.* [2013] have also proposed a backstop defined by a roof velocity of 6 km/s at ~8 km depth under the Simeulue Basin, with a dip to ~17 km depth seaward of Simeulue Island.

Our study area is within the southern end of the 2004 rupture zone. Underlying structures differ between the 2004 and 2005 rupture zones [*Kopp et al.*, 2008; *Dean et al.*,

2010; *Shulgin et al.*, 2013], so we do not attempt to extrapolate our results to the south. In our study area (Fig. 2.1), a wide plateau has already been hypothesized to represent a strong prism formed by thick,~4.5 km, sand/silt-prone sediments that have dewatered/lithified near the accretionary front [*Dean et al.*, 2010; *Gulick et al.*, 2011; *Geersen et al.*, 2013]. Another seismic study has also proposed that northern Sumatra accretionary prism contains strong inner wedge material, as expressed by seismic observations of both short- and long-wavelength folds between two prominent forearc highs, along with deformation that apparently occurs only within the youngest sediments near the Sunda Trench [*Fisher et al.*, 2007]. Such a strong prism would allow for a seaward expansion in the updip limit of seismogenesis, with resultant increased tsunamigenic potential. Bathymetric observations by *Henstock et al.* [2006], and visual results from ROV dives [*Moran et al.*, 2005b] confirming the existence of folds and fault-generated scarps at the deformation front, further support the possibility of surface rupture(s) near the Sunda Trench axis.

2.3. Data

Information used for this research consists of multibeam bathymetric and MCS data acquired after the 2004 earthquake. Compiled bathymetric data from various cruises (Table 1) are synthesized in Fig. 2.1. These data were acquired between 2005 and 2009 by The University of Texas at Austin (UT, USA), University of Southampton (UK), Oregon State University (USA), IFREMER (France), BGR (Germany) and Kyoto University (Japan). The merged bathymetric data have a 50 m grid resolution spacing and extend over the entire forearc, from northwest of northern Sumatra to west of Simeulue Island. This merged bathymetric data is also shown in Appendix A, Figure A.1.

Research Vessel	Cruise designation	Dates of acquisition	Multibeam	System information
HMS Scott of the UK Royal Navy	Marine Scientific Research	Jan-Feb 2005	SASS IV	2 sonar arrays operating at 12 KHz, outer beam at 50°-60°, 361 beams and 120° swath
Marion Dufresne II	MD 149	Jul-Aug 2005	SeaFalcon 11	Echosounder operating at 12 KHz, 400-500 beams, and swath
Sonne	184/2	Aug 2005	SIMRAD EM 120	2 transducers operating at 12 KHz, angular coverage < 150° and 191 beams/ping. Emission beam is 2° along track.
	186/1a-186/1c	Oct-Nov 2005		
	186/1d	Jan 2006		
	186/2-186/3	Jan-Mar 2006		
	189/1-189/2	Aug-Oct 2006		
	198/1-198/2	May-Aug 2008		
	200/1-200/2	Jan-Mar 2009		
Natsushima	NT05-02	Feb-Apr 2005	SeaBat 8160	A transducer array operating at 50 KHz, 126 beams and across track beam width 1.5° at
Roger Revelle	Knox05RR	May-Jun 2007	SIMRAD 120	2 transducers operating at 12 KHz, angular coverage < 150° and 191 beams/ping. Emission beam is

Table 2.1: Cruises acquiring multibeam data compiled and merged for this investigation.

The MCS data used in this study are a combination of data acquired by BGR during *Sonne*-186/2 (Jan 25-Mar 15, 2006) and by UT during *Sonne*-198/2 (July 18-August 1, 2008; designated SUMUT). The red lines on Fig. 2.1 represent seven MCS profiles interpreted for this investigation. Different MCS systems were utilized. The SUMUT survey acquired 1,250 km of data using a source array of 12 G-guns (total volume 5,420 in^3), a 2.4 km-long streamer containing 192 channels, and streamer depth of 10 m. Shot interval was 20 s ± 0.2 s. SUMUT recorded 16 s of MCS data with a 2 ms sampling interval. The BGR survey used a source array consisted of 16 G-guns divided into two sub-arrays; total volume was 3,100 in^3. The 3-km-long streamer consisted of 240-channels with a receiver spacing of 12.5 m, towed at a depth of 6 m. The shot interval was 18 s ± 0.3 s, and 14s of MCS data were recorded with a sampling interval of 2 ms.

2.4. Methodology

For the bathymetry, we used CARIS HIPS and SIPS to clean and merge all available bathymetric data (Table 2.1). Prior to editing, these data were set to a horizontal resolution of 50 m, a depth resolution of 1 m, a scale of 1:10,000, and the projection datum was UTM-WGS 84, zone UTM 46N. We cleaned the data interactively, visually inspecting for outliers and artifacts, line-by-line and swath-by-swath. A depth file produced by CARIS was read by the Generic Mapping Tools (GMT) [*Smith and Wessel*, 1990; *Wessel and Smith*, 1991, 1998] to generate the merged bathymetric map (Fig. 2.1).

We processed the MCS data through post-stack time migration, with targeted areas reprocessed through pre-stack time migration. Further processing detail is presented in *Gulick et al.* [2011] and *Martin et al.* [2014]. The BGR MCS data have been presented by *Berglar et al.* [2010], where each seismic profile is processed through post-stack

Kirchhoff time migration. Figures 2-4 show seismic profiles used in this study. All of these profiles are shown in two-way travel time (ms), as shown along the vertical axes.

2.5. Observation

2.5.1. Bathymetry

The accretionary prism offshore of northern Sumatra is composed of a wedge up to ~180 km wide [*Fisher et al.*, 2007], ranging in water depth from ~4.5 km [*Gulick et al.*, 2011] near the Sunda Trench to <1 km on the forearc high west of the Aceh (forearc) Basin. The Aceh Basin has a maximum depth of ~2.5 km [*Berglar et al.*, 2010]. In the south, the wedge narrows to ~125 km around Simeulue Island. Just landward of the deformation front, over an along-strike width of ~20-30 km offshore of Simeulue Island, is a region with steep slopes interpreted as the result of widespread surface erosion; these slopes are steeper than those defined by fold flanks farther landward [*Kopp et al.*, 2008].

Merged bathymetric data reveal that the accretionary wedge is composed of lineated highs and lows oriented primarily along margin strike [*Graindorge et al.*, 2008], with distances of 2-15 km between topographic highs. The widths of the highs are 2-45 km; intervening troughs are 1-8 km wide. Relief of these topographically high regions can be as much as ~1500 m. Dominant along-strike trends of the highs are ~320° in the north and ~290° in the south (Fig. 2.1). For comparison, the deformation front strikes ~330° in the north and ~310° in the south.

We use the compiled bathymetric data to estimate presumed fold vergence by first comparing the steepness of slope flanks within each lineated high, then by checking subsurface structure beneath these highs using the MCS data. Using both the seismic and seafloor data reduces uncertainties regarding the 3D relationships of subsurface folds and seafloor slopes. In all cases, we assume that the steeper seafloor slope associated with a

fold indicates that fold's vergence direction (Fig. 2.2b inset). We acknowledge that steeper slopes may also be the result of surficial erosion, a result of higher order (i.e., minor) thrust faults and/or interactions between folds. To reduce this uncertainty, we verified the existence of thrust fault(s) underlying the steeper slope at the base of observed folds. Using the available MCS data (Figs. 2.2-2.4), we can therefore both validate fold vergence and interpret shallow faults flanking such folds, if they exist at the resolution of our seismic data (Fig. 2.2b insets; see next section). Furthermore, we use dashed lines and/or question marks to represent faults interpreted with less certainty (Figs. 2.2-2.4; Figs. 2.3a, 2.4b insets). We used blue and orange vertical arrows for landward- and seaward-vergent folds, respectively. Some folds are without any arrow, because of uncertainty. *Graindorge et al.* [2008] measured slope gradients on their bathymetric data within the region 1.5-6°N and 92-96°E in order to determine fold vergence; our zone of predominant landward vergence zone is comparable to theirs.

2.5.2. MCS Data

Available MCS profiles (seven red lines, Fig. 2.1) image the upper 1-2 s of the wedge, illustrating that it is affected by complex landward- and seaward-dipping interpreted fault planes. These fault planes generally bound the higher and lower regions observed on the bathymetric data. We interpret the highs as lineated anticlinal structures, exhibiting separations of 2-15 km, between what we interpret as first-order (major) thrust faults and paired conjugate structures; second order (i.e., smaller-scale) faults are generally separated by <1 km, occurring generally within these anticlines. We base our interpretation of any fold's direction of shortening on the related interpretation of vergence, and primary versus backthrust relationships of interpreted thrust faults flanking each fold (Fig. 2.2b inset). Near the Sunda Trench, we can interpret normal faults down to ~8.8 s two-way-

travel time (TWT), the depth of our interpreted pre-décollement (green line, Figs. 2.2-2.4, Fig. 2.2a inset). We interpret the pre-décollement based on its negative polarity (green arrows, Fig. 2.2a, inset). Near the trench, the interpreted landward-vergent fold is an example of fault interaction resulting in the observed landward verging thrust fault that possibly extends toward the décollement (Figs. 2.2-2.3). Within the plateau landward of the trench, faults are harder to identify >2 s below the seafloor. We acknowledge that Figs. 2.2-2.4 are shown with high vertical exaggeration (VE) in order to show greater lateral extents; therefore, we provide subsets with lower VE. Uninterpreted profiles using lower VE are also submitted as supplementary material with subset figures showing interpreted faults.

2.5.2.1. Seismic Profiles BGR06-107 and SUMUT-07

SUMUT-07 (Fig. 2.2b) is approximately parallel to and ~34 km south of BGR06-107 (Figs. 2.1 and 2.2a). Along these profiles, seafloor depths range from ~4,500 m near the trench to ~990 m (Fig. 2.2a, CDP ~31,800) and ~750 m (Fig. 2.2b, CDP ~19,000), ~75 km and ~90 km, respectively, landward from the trench. The widths of the accretionary prism along these profiles are ~165 km (Fig. 2.2a) and ~185 km (Fig. 2.2b), respectively. We interpret the pre-décollement at subsurface depths ranging from ~8.8 s (Fig. 2.2a, CDP 46,500) beneath the Sunda Trench to ~8 s (Fig. 2.2a, CDP ~39,300) to ~9 s (Fig. 2.2b, CDP 32,000) beneath the deformation front [*Dean et al.*, 2010]. From the deformation front to the seaward edge of Aceh Basin, the spacing of interpreted anticlines and intervening synclines ranges from ~2-13 km. Widths of these folds at the seafloor range from <1 to 12 km. Near the trench (Fig. 2.2a inset), several blind (i.e., non-surfacing) normal faults appear to intersect the pre-décollement. The first fold landward of the trench is landward-vergent (CDP ~42,500); it is an example of fault interactions where the observed major

thrust fault possibly extends toward the décollement. Five more interpreted landward-vergent folds are observed from the trench into the prism. The width of this landward-vergent zone is ~65 km. The westernmost seaward-vergent fold occurs at CDP ~31,800, which is also the shallowest part of the wedge on BGR06-107. Toward the Aceh Basin to the east, interpreted folds are predominantly seaward-vergent. The width of the seaward vergent zone is ~80 km. A region of mixed vergence, ~25 km wide, occurs in between, from CDP ~30,000 to ~33,000. We acknowledge that the widths of these vergence zones are an approximate; they represent the span of prevalent vergence direction of folds as confirmed by images of subsurface faulting. For the mixed vergence zone, we estimated its width to encompass the area with fold(s) of both vergence styles (no preferred vergence) bounded by local troughs. On Fig. 2.2b, near the westernmost landward-vergent fold (CDP ~31,500); we interpret blind faults extending downward toward the pre-décollement. A generally landward-vergent zone again occurs nearer the deformation front (CDP ~21,000-32,000), with a width of ~75 km, and a seaward-vergent region extends from CDP ~17,000 for ~90 km towards the Aceh Basin. The fold near CDP ~19,000, interpreted as seaward-vergent, occurs at the shallowest part of the wedge, within a mixed vergence zone ~25 km wide. Piggyback basins (Fig. 2.2a: CDPs 37,700, 26,000, 24,500, and 19,000 and Fig. 2.2b: CDPs 24,500; 21,500; 14,000) are observed scattered across the plateau; in all cases, fanning of infilling sediment suggests syntectonic deposition and continuing compression of fill within these basins [*Sibuet et al.*, 2007]. We interpret the West Andaman Fault (WAF) along the western/seaward edge of the Aceh Basin (Fig. 2.2a) [*Sibuet et al.*, 2007; *Martin et al.*, 2014]. Within the Aceh Basin itself, blind faults appear to crosscut an acoustically strong reflector at ~6 s. *Berglar et al.* [2010] and *Martin et al.* [2014] interpret this strong reflector as the acoustic basement of the Aceh Basin.

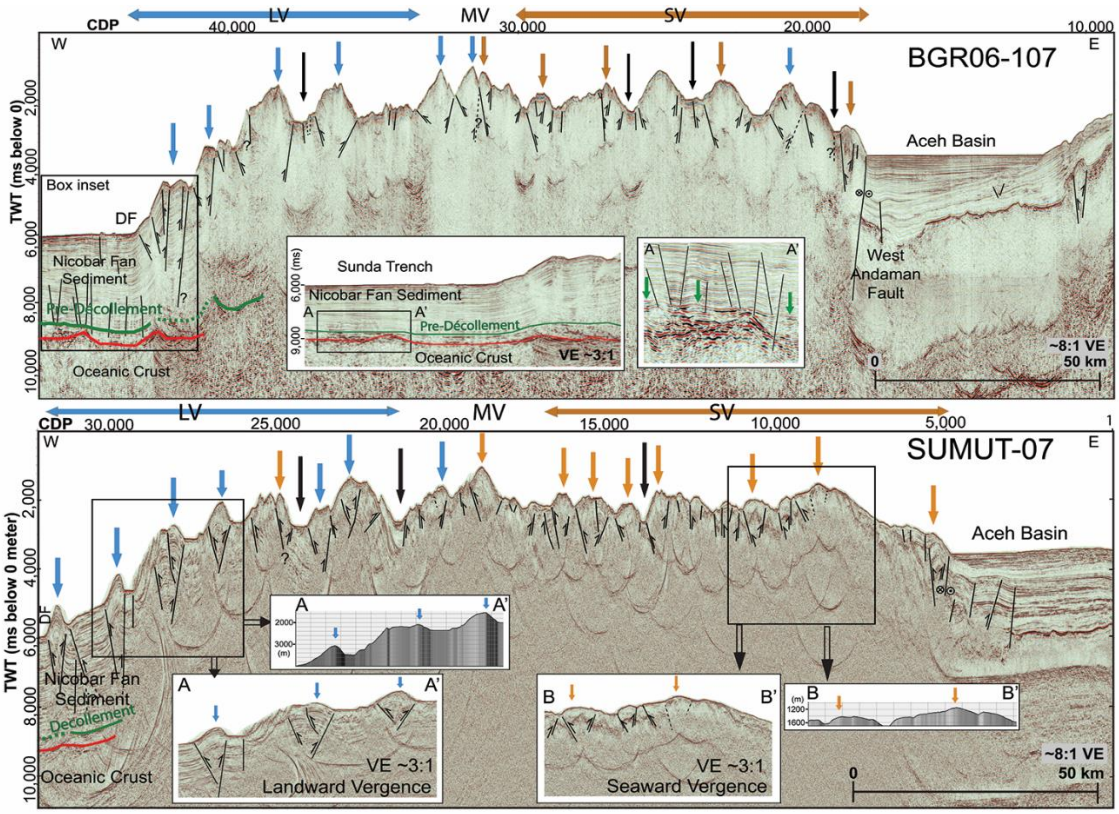

Figure 2.2: Interpreted seismic profiles BGR06-107 (2a), SUMUT-07 (2b). See Figure 2.1 for locations. Figures 2.2-2.3 are interpreted seismic profiles with vertical exaggeration ~8 and ~3 for Figure 2.4. Uninterpreted profiles with lower vertical exaggeration are submitted as supplementary material with some subsets showing interpreted faults. On all profiles, CDP number (upper margin) shows the distance along the length, travel-time depth is shown on the left (ms). Green line is interpreted pre-décollement, red line is interpreted top of oceanic crust, and DF stands for deformation front. Vertical blue, orange, and black arrows indicate interpreted landward-vergent folds, seaward-vergent folds, and piggyback basins, respectively. Our interpreted vergence zone widths are shown with colored horizontal arrows. Horizontal blue arrows (Figure 2.2a: CDPs ~33,000-43,000, Fig 2.2b: CDPs ~21,000-32,000) represent interpreted landward vergence. Horizontal orange arrows (Figure 2.2a: CDPs ~18,000-30,000, Figure 2.2b: CDPs ~5,000-17,000) represent interpreted seaward vergence. Between these two vergence zones (Figure 2.2a: CDPs ~30,000-33.000, Figure 2.2b: CDPs ~17,000-21,000) is a region of mixed vergence. Inset figures in Figure 2.2a show interpreted blind normal faults that crosscut the interpreted pre-décollement. Two inset pairs in Figure 2.2b show bathymetric and seismic data of interpreted landward- and seaward-vergent folds in lower VE.

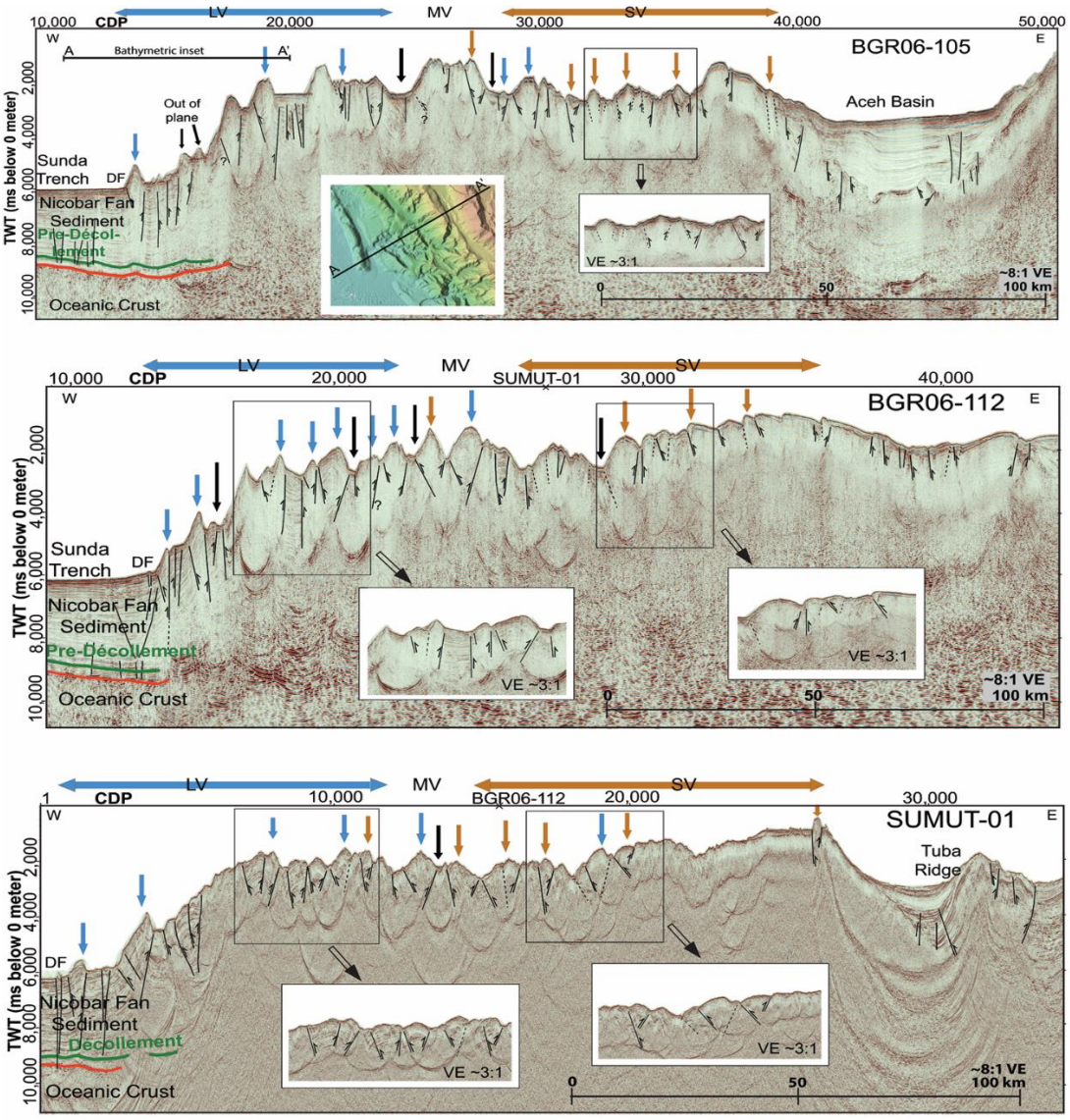

Figure 2.3: Interpreted seismic profile BGR06-105 (2.3a), BGR06-112 (3b), SUMUT-01 (2.3c). See Figure 2.1 for locations and caption of Figure 2.2 for description of annotations. Horizontal blue arrows (2.3a: CDPs ~13,000-25,000, 2.3b: CDPs ~13,000-22,000, 2.3c: CDPs ~1,000-11,000) represent interpreted landward vergence regions. Horizontal orange arrows (2.3a: CDPs ~29,000-40,000, 2.3b: CDPs ~26,000-36,000, 2.3c: CDPs ~15,000-26,000) represent interpreted seaward vergence zones. The region between the two (2.3a: CDPs ~25,000-29,000, 2.3b: CDPs ~22,000-26,000, 2.3c: CDPs ~11,000-15,000) is characterized by mixed vergence. Inset figure in Figure 2.3a shows bathymetric data around the prism toe of massive slope failures. Subsets of seismic data shows interpreted thrust faults with certainty and less certainty (dashed).

2.5.2.2. Seismic Profiles BGR06-105, BGR06-112, and SUMUT-01

Interpreted MCS profile BGR06-105 (Fig. 2.3a) is located ~10 km south of SUMUT-07 and approximately parallel to it (Figs. 2.1 and 2.2b). Seismic profile BGR06-112 (Fig. 2.3b) is located ~85 km south of and is approximately parallel to BGR06-105 (Figs. 2.1 and 2.3a). Seismic profile SUMUT-01 (Fig. 2.3c) crosses the accretionary prism at a ~70° angle (Fig. 2.1). In its southwestern portion, this profile is ~120 km south of BGR06-105, but its northeastern end is only ~34 km south of BGR06-105. Profile SUMUT-01 crosses BGR06-112 at CDP 26,500 (Fig. 2.3b). Profile BGR06-112 crosses SUMUT-01 at CDP 15,600 (Fig. 2.3c). Fig. 2.3 exhibits seafloor depths ranging from ~4,500 m near the trench (Fig. 2.3a: CDP 10,000; Fig. 2.3b: CDP 10,000; Fig. 2.3c: CDP 1) to ~600 m (Fig. 2.3a: CDP 25,400; Fig. 2.3b: 34,750) within the prism, and locally only ~270 m (Fig. 2.3c: CDP 26,300) near the Tuba Ridge [*Malod et al.*, 1993; *Curray*, 2005; *Mosher et al.*, 2008; *Martin et al.*, 2014]. On Fig. 2.3 (profiles BGR06-105, BGR06-112, and SUMUT-01), we interpret the pre-décollement to be at depths ranging from 8.2-9 s [*Dean et al.*, 2010]; near the trench, we interpret "blind" normal faults extending down to the pre-décollement. The spatial distribution of observed vergence regions is similar to that shown by BGR06-107 (Fig. 2.2a) and SUMUT-07 (Fig. 2.2b); predominantly landward and seaward vergence zones exist (Fig. 2.3). We observe at least one piggyback basin on each of these profiles (Fig. 2.3a: CDPs 25,000 and 28,000; Fig. 2.3b: CDP 15,600, 20,100, 22,100, 28,400; Fig. 2.3c: CDP 13,500). In all observed piggyback basins, we presume continued shortening [*Sibuet et al.*, 2007] of the prism, as they are filled by tilted sedimentary strata.

On profile BGR06-105 (Fig. 2.3a), just landward from the trench, between the first and second landward-vergent folds (CDP 13,500 and 18,700, respectively), two isolated folds appear to be seaward-vergent (CDP 15,600 and 17,500). The seaward-

facing sides of these folds appear to be eroded [*Mosher et al.*, 2008], as shown by rough surface texture on the bathymetry data (Fig. 2.1; Fig. 2.3a, inset). Because their appearance has been modified by surficial erosion, we suggest that both of these folds are landward-vergent. Upon examination of the bathymetric data, the symmetrical fold adjacent to the interpreted fold at CDP 15,600 looks instead to be an artifact of the data acquisition (an out-of-plane image), and we conclude therefore that it cannot be used to discern vergence. Zoomed-in figure in Fig. 2.3a shows our fault interpretation; dashed lines represent less certainty and solid lines represent greater certainty.

Profiles BGR06-112 (Fig. 2.3b) and SUMUT-01 (Fig. 2.3c) cross the plateau landward from a region of folded structures near the trench to a topographically higher region with less apparent near-surface deformation (starting at CDP ~30,000, Fig. 2.3b, and at CDP ~19,000, Fig. 2.3c). This elevated, smooth region (dashed brown trapezium, Fig. 2.1) lies northwest of and on-strike with Simeulue Island. Other islands farther southeast along this margin are known to be capped by Quaternary carbonate reefs [*Dorobek*, 2008]. Furthermore, the Simeulue Basin, eastward of Simeulue Island, is known to contain multiple carbonate platforms [*Berglar et al.*, 2008; *Lutz et al.*, 2011]. Based on the proximity of such platforms, its relatively flat top, the pinnacle-like feature on SUMUT-01, and the lack of acoustic penetration associated with it, we conclude that this region is a shallowly submerged carbonate platform. Subsets in Figs. 2.3b and 2.3c show some preserved block-like strata forming the folds where we can interpret faults with confidence.

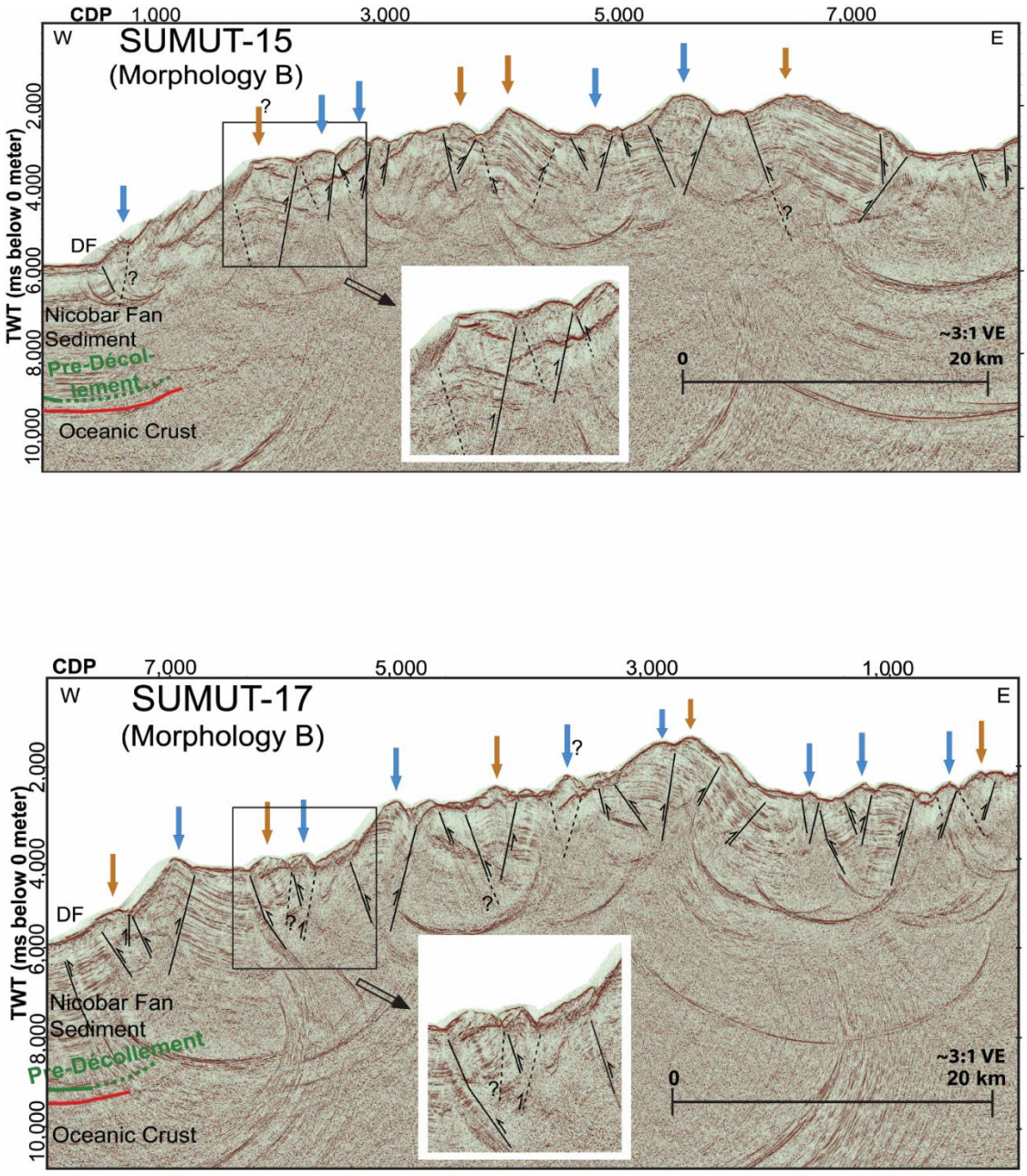

Figure 2.4: Interpreted seismic profiles SUMUT-15 (a) and SUMUT-17 (b). See Figure 2.1 for locations and caption of Figure 2.2 for description of annotations. These profiles transect morphology B [*Henstock et al.*, 2006], where the prism toe consist of a frontal fold with erosion. The lengths of these profiles are ~50 km. Both exhibit predominantly landward vergence (Figures 2.1 and 2.5). Subsets of seismic data show interpreted thrust faults and an example of faults interaction that probably cause the seaward-vergent fold.

2.5.2.3. Seismic Profiles SUMUT-15 and SUMUT-17

Fig. 2.4 shows two ~50 km-long seismic profiles, SUMUT-15 and SUMUT-17 (Fig. 2.1). Based on negative polarity, we interpret a pre-décollement surface on SUMUT-15 at ~9 s (CDP 0) to ~8.5 s (CDP 1,200), and on SUMUT-17 at ~9 s (CDP 8,000) to ~8 s (CDP 7,000). All interpreted faults are within ~2 s of the seafloor. *Henstock et al.* [2006] have proposed two different morphology zones along this part of the deformation front, which they designate A and B, based on topographic distinctions near the toe of slope. They interpret morphology A to be the result of a seaward-dipping thrust fault, yielding a landward-vergent fold, conversely morphology B implies the presence of a landward-dipping thrust fault, causing a seaward-vergent fold. The five profiles shown in Figs. 2.2 and 2.3 transect a seafloor region along the deformation front which has been interpreted as morphology A [*Henstock et al.*, 2006]. Conversely, the profiles in Fig. 2.4 intersect the deformation front called morphology B [*Henstock et al.*, 2006]. Subsurface fault interpretations of SUMUT-15 (Fig. 2.4a) show the region landward of morphology B can be interpreted as predominantly landward-vergent. However, observations along SUMUT-17 (Fig. 2.4b) show that an increased number of seaward-vergent folds on that profile. Subset in Fig. 2.4a shows a fold interpretation uncertainty due to apparent surface erosion. Inset in Fig. 2.4b displays faults interaction and uncertainty in interpretation; both fold vergence styles are observed.

2.6. Discussion

2.6.1. Seafloor Morphology

Observed lineations of bathymetric highs show changes of direction between the northern and southern parts of the forearc (Fig. 2.1). In the northern portion of the study area, the prism toe exhibits generally smooth fold and trough topography [*Henstock et al.*,

2006]. Conversely, the southern part of the toe region is characterized by more slope failures, resulting in more rugged, shorter wavelength topography [*Kopp et al.*, 2008]. The structural trend of the deformation front is 330° in the northern portion, and 310° in the south. However, the strike of fault-controlled ridges landward of the deformation front is ~320° in the northern section and is ~290° in the southern. We suggest that these differences in strike between the deformation front and ridges within the plateau, amounting to ~10° in the northern region and ~20° in the southern part, are the result of slope failures occurring along the deformation front, which occur more extensively in the southern portion of the study area (Fig. 2.1). These frontal slope failures may occur when initial underthrusting of sediments at the deformation front produces oversteepening of the slopes [*Kopp et al.*, 2008]. The along-strike change of structural trend has also been observed by *Dean et al*. [2010] and *McNeill and Henstock* [2014], near where the 96° N Fracture Zone is subducting (~2.5° N). They have pointed out a difference both in prism width and in taper angle north and south of this intersection and conclude that smoothness of the subducting plate, along with sediment thickness and properties, play roles in the differing prism morphology observed.

2.6.2. Wedge Morphology and Structure

Seismic profiles BGR06-107, SUMUT-07, BGR06-105, BGR06-112 and SUMUT-01 (Figs. 2.2-2.3) image the accretionary prism over along-strike distances of ~180 km near the deformation front and ~140 km near the seaward edge of the Aceh Basin. Observed changes in seafloor topography illustrate the complex shallow structure of the prism. Folding and associated bounding (primarily thrust) faults dominate the upper 1-2 s sub-seafloor of prism structure. Fold spacing on all available profiles is similar, ~2-15 km between axes, with fault spacing 1-7 km. Between some anticlines lie

piggyback basins; tilted strata within these basins, extending to the modern seafloor, suggest bounding thrust faults have been recently active and that compression continues across the study area, although timing of onset of deformation is uncertain [*Sibuet et al.*, 2007; *Graindorge et al.*, 2008]. Such piggyback basins are inferred by others as close as ~10 km from the deformation front [*Kopp et al.*, 2008] south of our study area, and as far as ~100 km from the deformation front [*Fisher et al.*, 2007] to the north.

Both extant theories and experiments suggest that the observed extensive landward vergence may occur by any one or a combination of five boundary conditions: 1) low basal shear stress, 2) a seaward-dipping lithification front/backstop, 3) high sedimentation rate, 4) young subducting plate, and/or 5) low/medium rate of convergence [*Seely*, 1977; *Byrne and Hibbard*, 1987; *MacKay*, 1995; *Wang and Davis*, 1996; *Gulick et al.*, 1998; *Gutscher et al.*, 2001]. Using seismic observations along the Sunda subduction zone, *McNeill and Henstock* [2014] propose that the landward vergence zone near the prism toe offshore of northern Sumatra may be due either to low basal shear stress or the presence of a backstop; they observe acoustic evidence of an overpressured layer at depth that has become the pre-décollement (Fig. 2.2a inset) [*Dean et al.*, 2010; *Geersen et al.*, 2013]. There is no consensus on age of the subducting plate; proposed ages range from 52-61 my [*Singh et al.*, 2011] to 21-24 my [*Müller et al.*, 2008]. The rate of convergence is 5-6 cm/yr [*Natawidjaja et al.*, 2007], a low-medium range. Therefore, the relevant boundary conditions for landward vergence offshore of northern Sumatra include boundary conditions 1-3 above. The prevalence of such vergence for many kilometers landward of the deformation front (Fig. 2.5) also suggests that high sedimentation rate is an important controlling variable, as we observe ~4.5 km-thick incoming sediment everywhere along this portion of the Sunda Trench (Figs. 2.2-2.4). Seaward vergence dominates farther south, where incoming sediments are thinner [*Kopp*

and Kukowski, 2003; *Gulick et al.*, 2011; *McNeill and Henstock*, 2014; *Moeremans et al.*, 2014].

One consequence of thick incoming sediment, particularly fan-based sediment that may be sand-/silt-prone, is that coarser-grained material could accelerate dewatering and associated lithification at depth [*Gulick et al.*, 2011; *Geersen et al.*, 2013]. Near the deformation front, we observe blind normal faults that cross-cut the pre-décollement at depths of 8-9 s (Figs 2-3); we suggest that these faults form fluid conduits as deeper layers undergo lithification prior to accretion [*Gulick et al.*, 2011]. Sediments >2-3 km thick that extend over large distances can also trigger dewatering processes before accretion, through increased temperature-driven diagenetic activity [*Geersen et al.*, 2013]. In our seismic profiles, we also suspect induration of shallower wedge sediments because of observed preservation of block-like layering landward of the deformation front (insets, Figs. 2.2b, 2.3b, 2.3c) [*Gulick et al.*, 2011], along with a general lack of acoustic penetration deeper than ~2 s farther landward (Figs. 2.2-2.4). We suggest that these incoming (sediment) blocks have been dewatered and lithified before being accreted, contributing to the strength of the associated wedge interior [*Gulick et al.*, 2011; *Geersen et al.*, 2013].

Northwest of our study area (Fig. 2.1), *Fisher et al.* [2007] have studied a portion of the wedge plateau >100 km wide that is topographically depressed in the center; we note that such a pattern is not representative of the general morphology of the plateau within our study area. On three of our crossing profiles (Figs. 2.2a, 2.2b, 2.3a), we instead observe the shallowest point to be within the plateau, while on two other profiles (Figs. 2.3b and 2.3c), we observe a topographic high, ~60 km wide, with apparently reduced deformation, adjacent to the Aceh Basin. *Fisher et al.* [2007] have suggested that the wide, ~flat plateau implies a strong wedge interior. The observed steep wedge taper at

the deformation front (8°-12° seaward slope of the outer high, 5° dip of the basal décollement [*Fisher et al.*, 2007]) narrows landward of the outer high, which is also consistent with increased strength of the wedge interior [*Davis et al.*, 1983; *Wang and Hu*, 2006]. In comparison, our seismic profiles consistently show both an extended region of landward-vergent folds (Fig. 2.5) and a plateau-wide limit of penetration of ~2 s that may reflect accreted sediment at depth deformed sufficiently to disrupt sedimentary layering. We suggest that these observations also support a strong wedge interior.

In our observations (Figs. 2.2-2.3), the region landward of the trench (bathymetry Morphology A) is predominantly landward-vergent, supporting the hypothesis for that morphology, a seaward-dipping frontal thrust, put forward by *Henstock et al.* [2006]. However, Figs. 2.4a and 2.4b also support predominantly landward vergence within ~50 km of the deformation front landward of Morphology B, contradicting *Henstock et al.* [2006] that such a morphology should be caused by a landward-dipping thrust fault. Our observations, and existing published studies, all confirm that the thickness of incoming sediment is the same throughout our study area. Our seismic observations support an approximately constant pre-décollement depth beneath the deformation front. Therefore, we conclude that the wedge's interior structure must be consistent along strike from 2.5-4.5°N, supporting the existence of seaward-dipping thrust faults (i.e., landward vergence) everywhere along the deformation front within this region (Fig. 2.5) [*McNeill and Henstock*, 2014].

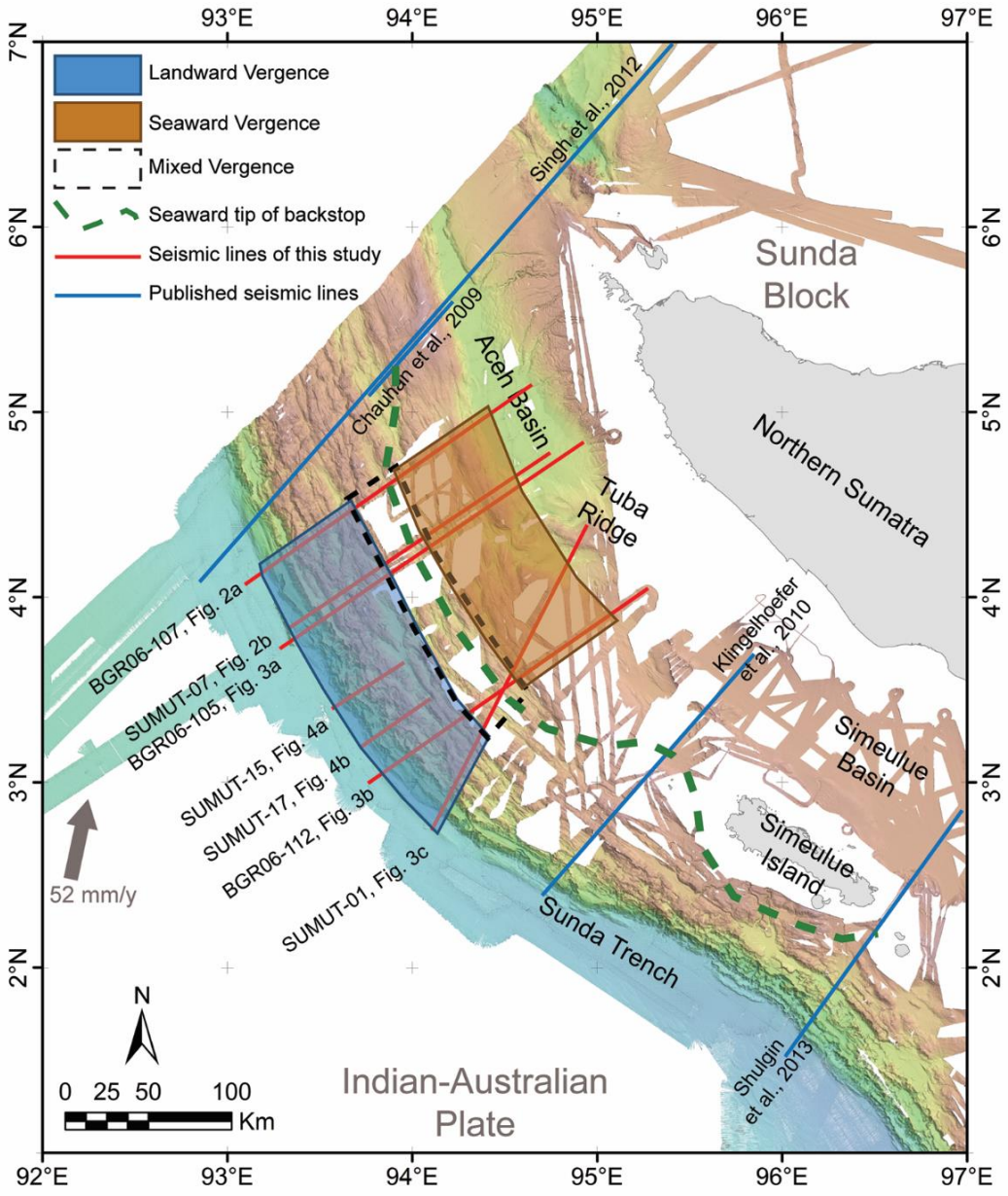

Figure 2.5: Structural classification based upon analysis of the seven seismic profiles (red lines) imaging the northern Sumatra accretionary prism (Figures 2.2-2.4). Blue polygon represents landward vergence zone and orange polygon represents seaward vergence zone. The mixed vergence zone (dashed polygon) lies in between. Dashed green line is our proposed seaward tip (edge) of the rigid backstop that we propose for this part of the wedge.

Our five cross-wedge profiles (Figs. 2.2-2.3) exhibit approximately the same tripartite division of vergence zones: landward-vergent on the seaward side nearer the deformation front, mixed vergence in the middle, and seaward-vergence nearer the Aceh Basin [*McNeill and Henstock*, 2014]. However, the observed widths of these zones vary along strike (Table 2.2). Fig. 2.5 displays a map view summary of the three zones. The zone of mixed vergence includes the shallowest point on the wedge for three of the five cross wedge seismic profiles: BGR06-107 (Fig. 2.2a, ~1,000 m, CDP ~31,800), SUMUT-07 (Fig. 2.2b, ~1,000 m, CDP ~19,000), and BGR05-105 (Fig 2.3a, ~1,100 m, CDP ~27,000). On the other two cross-wedge profiles, the shallowest point of the wedge corresponds to the topographically elevated, smooth region (Figs. 2.3b and 2.3c) within the seaward vergence zone that we have already surmised represent drowned carbonate platforms capping the wedge topography/structures [*Dorobek*, 2008] possibly with some addition vertical tectonics from the adjacent West Andaman Fault [*Martin et al.*, 2014].

	Landward Vergence (km)	Seaward Vergence (km)	Mixed Vergence (km)
BGR06-107 (Fig. 2.2a)	~65	~80	~25
SUMUT-07 (Fig. 2.2b)	~75	~90	~25
BGR06-105 (Fig. 2.3a)	~63	~75	~24
BGR06-112 (Fig. 2.3b)	~55	~90 (include the topography high)	~22
SUMUT-01 (Fig. 2.3c)	~69	~80 (include the topography high)	~23

Table 2.2: Widths of vergence zones along strike (refer to Figure 2.1).

2.6.3. Proposed Backstop Model

A backstop, a distinctive structure within an accretionary prism that is stronger than the subsequent/younger accreting material, represents a buttress against which

accreting material deforms [*Davis et al.*, 1983; *Byrne et al.*, 1993]. Our study of the accretionary prism offshore of northern Sumatra shows that a landward vergence zone is consistently situated landward of the deformation front for a cross-wedge distance up to ~75 km (Table 2.2). Based upon what is proposed from numerical models and sandbox experiments as to how such landward vergence develops [*Davis et al.*, 1983; *Byrne et al.*, 1993; *Gutscher et al.*, 1998], we suggest the existence of a seaward dipping backstop within the wedge east of the landward limit of the mixed vergence zone (Fig. 2.5). Unfortunately, we cannot directly image it.

Our proposed backstop geometry (Fig. 2.6) lies between 2° and 5°N, based on our interpretation of the structure and morphology of this part of the accretionary prism, backstop models in subduction settings [*Byrne et al.*, 1993; *Gutscher et al.*, 2001; *Storti et al.*, 2001], and velocity models developed for this margin [*Klingelhoefer et al.*, 2010; *Singh et al.*, 2012; *Tang et al.*, 2013]. For the northern region of our study area (Fig. 2.1 and 2.6a), we use a velocity model published by *Singh et al.* [2012] as a basis for our backstop interpretation. We interpret the top of the backstop under the Aceh Basin to coincide with a velocity contour of ~5.8 km/s; this velocity represents a reasonable average velocity for continental (i.e., Sunda Block) crust [*Taira et al.*, 1998; *Brocher*, 2005]. For the southern region (Fig. 2.6c), we again estimate the roof of our proposed backstop to approximate the ~5.8 km/s contour [*Klingelhoefer et al.* [2010]. As is true of all velocity models, uncertainty increases with depth. The 5.8 km/s contour may represent an average velocity of continental crust, but that and higher velocities beneath the contour could also represent older accreted material overlying continental crust.

For the central part of the prism in our study area (Fig. 2.1 and 2.6b), we use SUMUT-07 (Fig. 2.2b) as basis for our backstop interpretation; it represents the seven profiles we studied. SUMUT-07 crosses the Aceh Basin, where we observe a strong

acoustic basement reflector at the base of the basin's presumed sedimentary fill. We hypothesize that the roof/top of the material that forms our proposed backstop coincides with that reflector, which occurs at a depth of ~6 s beneath the basin. We estimate this depth to coincide with the ~5.8 km/s contour generated by *Chauhan et al.* [2009], *Klingelhoefer et al.* [2010], *Singh et al.* [2012] and *Shulgin et al.* [2013] (Fig. 2.1), the ~5.5 km/s contour generated by *Tan et al.* [2012], and the strong basement reflector recognized by *Berglar et al.* [2010] in the same area. We cannot estimate either the roof position or slope of the backstop from the west end of Aceh Basin seaward beneath the wedge, since there is no recognizable reflector in this area. However, we can infer a likely geometry based on what is known from accretionary wedge modeling (Figs. 2.6a and 2.6c), specifically results from sandbox experiments [*Byrne et al.*, 1993; *Wang and Davis*, 1996; *Gutscher et al.*, 2001] along with seismic observations from other parts of this margin [*Kopp and Kukowski*, 2003]. All indicate that for seaward-dipping backstops, the shallowest point along a wedge likely coincides with the backstop's seaward toe or edge. The backstop geometry used in sandbox experiments or numerical models to simulate accretionary wedge evolution is generally either rectangular or triangular. In the rectangular case, both seaward and landward edges are vertical; the seaward edge acts like a snowplow, deforming younger incoming sediments [*Davis et al.*, 1983], while the roof is horizontal [*Wang and Davis*, 1996]. In the triangular case, the bottom side rests along the landward-dipping subducting plate and the seaward side forms a seaward-dipping slope [*Byrne et al.*, 1993]. The tip of the triangle between these two sides is located somewhere beneath the wedge, essentially a doorstop lying near or on top of the subducting plate. Model results show that the location of this tip can coincide with the location of the shallowest point of the accretionary wedge [*Byrne et al*., 1993; *Gutscher et al*., 2001]. Our proposed backstop incorporates these model results; we propose a

generally seaward-dipping backstop with a tip beneath the shallowest part of the prism (dashed green line, Fig. 2.5).

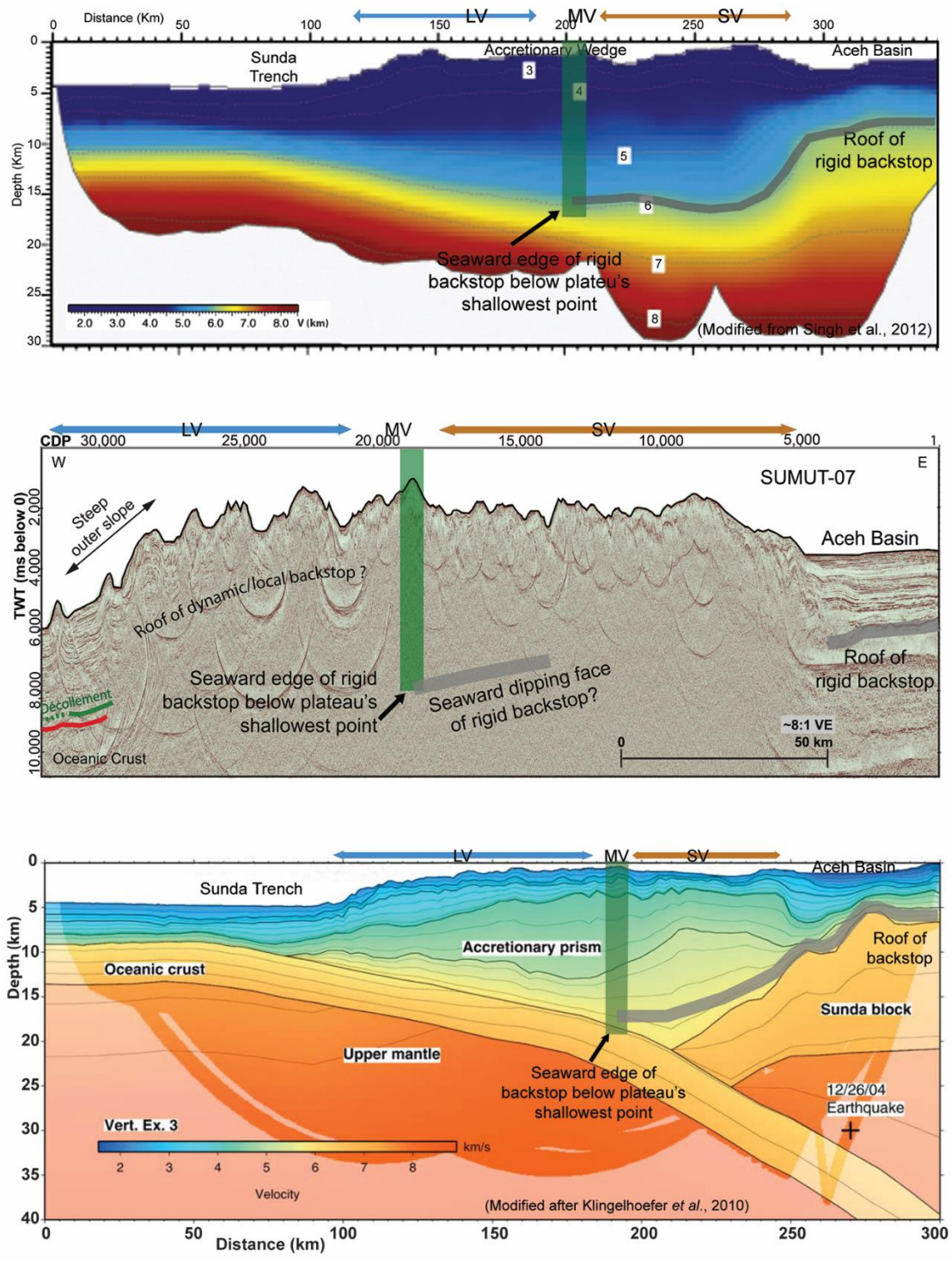

Figure 2.6: Proposed geometry of a backstop within the wedge for region 2-5°N.

Figure 2.6, cont.: Proposed geometry of a backstop within the wedge for region 2-5°N. Refer to Figure 2.1 for location. The thick grey curves in all panels are estimated location and shape of the roof of our proposed backstop. Blue and orange horizontal arrows represent structural zones: landward vergence (LV), seaward vergence (SV). The mixed vergence zone (MV) is between the two zones. a) represent the northern part, based on a velocity model published by *Singh et al*. [2012]. Our proposed roof of the backstop follows the ~5.8 km/s (grey curve). The seaward tip of that backstop is located under the shallowest point of the wedge (green bar), which generally lies within our mixed version zone (Figure 2.5). b) represent the central part of our study area. The roof of the proposed backstop coincides with a strong reflector under the Aceh Basin (grey curve) [*Berglar et al*., 2010]. The seaward tip of the backstop is located under the shallowest point of the wedge (green bar). c) represent the roof geometry of the backstop in the southern part, based on a velocity model of *Klingelhoefer et al*. [2010]. Again, the roof of the backstop follows the ~5.8 km/s (grey curve). In general, we conclude the roof of the backstop from the western edge of the Aceh Basin form a seaward dipping slope and extend into the wedge to the position under the shallowest point of the wedge (green bar).

We can identify the shallowest point on the wedge plateau on three of our five cross-prism profiles (Figs. 2a, 2b, 3a). On Figs. 3b and 3c, interpreted shallow carbonate platforms within the seaward vergence zone lie above this backstop, obscuring what could be the tip of a backstop within our mapped mixed vergence zone. Nonetheless, we suggest that everywhere in our study area the seaward tip of the backstop must lie beneath the mixed vergence zone and the highest point in the wedge excepting the carbonate cap in the southern two profiles. Furthermore, landward of this tip, the roof of the backstop must be seaward-dipping, because it deforms younger wedge sediments into the extended landward vergence zone that we observe towards the Sunda Trench [*Byrne and Hibbard*, 1987]. As stated above, velocity models generated for this part of the margin [*Chauhan et al.*, 2009; *Klingelhoefer et al.*, 2010; *Singh et al.*, 2012; *Shulgin et al.*, 2013; *Tang et al.*, 2013] confirm that this backstop must also be composed of material with a compressional wave velocity in the ~5.5-6.8 km/s range, signifying a composition that approximates either continental crust or older, lithified accreted sediments overlying such crust.

Several studies have proposed backstop models offshore of northern Sumatra with varying results as different input data are used. Close to the deformation front, a backstop is inferred from gravity data suggesting higher sediment densities [*McNeill et al.*, 2006; *McNeill and Henstock*, 2014]. From single channel seismic profiles, a backstop is inferred using observed pattern of near-surface wedge deformation [*Fisher et al.*, 2007; *Mosher et al.*, 2008]. From deep-penetration seismic and tomography, a proposed backstop is extended to the western edge of the Aceh Basin (Fig. 2.6a) [*Chauhan et al.*, 2009; *Singh et al.*, 2012], based on a seaward-dipping reflector in that location. A backstop under the Simeulue Basin (Fig. 2.6c, [*Klingelhoefer et al.*, 2010]) and around Simeulue Island [*Shulgin et al.*, 2013] is inferred based on seismic velocities of ~6-7

km/s. Numerical modeling, incorporating frictional properties of the sediment and associated mantle wedge by *Tan et al.* [2012] suggests that the overriding plate crust acts as a backstop, extending seaward toward the Sunda Trench. Using a compressional wave velocity model, *Tang et al.* [2013] proposed a backstop extending beyond Simeulue Island toward the trench. These diverse observations are essentially in agreement with our proposed backstop model.

While we propose a rigid, seaward-dipping backstop within the inner wedge to be responsible for the observed zone of landward vergence, there is also a possibility of a dynamic backstop farther seaward [*Kopp and Kukowski*, 2003]. A dynamic backstop is defined as sediment accreted against a rigid backstop, and characterized by increasing lithification of accreted material [*Kopp and Kukowski*, 2003]. *McNeill and Henstock* [2014] identify a density anomaly situated near the deformation front that they propose contributes to the slope break and relatively steep frontal slope (5-6°) of the outer wedge; this anomaly could represent such a dynamic backstop, located seaward of our proposed rigid backstop.

The composition of the backstop under the Aceh Basin and adjacent accretionary prism is still being debated. *Berglar et al.* [2008], based on seismic data and core samples down to 3 km depth within Simeulue Basin, have pointed out that their observed acoustic basement is likely pre-Neogene in age, composed either of a preexisting continental shelf [*Rose*, 1983] or forearc sediments deposited in the late Mesozoic-early Tertiary [*Karig et al.*, 1979; *Rose*, 1983]. However, *Martin et al.* [2014] have concluded that the basement of the Aceh Basin is Oligocene or younger. The Nicobar Fan, the presumed primary source of the sediment forming the accretionary prism, has been suggested to be no older than late Miocene-early Pliocene [*Curray and Moore*, 1971; *Bowles et al.*, 1978]; *Curray and Moore* [1974] have suggested that the accretionary prism formed in the late Miocene.

Conversely, velocity models by *Singh et al.* [2008] and *Chauhan et al.* [2009] suggest that Aceh Basin basement is crystalline and part of the Sunda Block, the same as that underlying the Simeulue Basin [*Klingelhoefer et al.*, 2010; *Shulgin et al.*, 2013]. Based on tectonic models, *Barber and Crow* [2003] have proposed that this continental block offshore of northern Sumatra is granite of Jurassic-Cretaceous age. If the estimated seaward extent of our backstop (green dashed line, Fig. 2.5) is accurate, then this backstop may consist of an older sedimentary deposit or be of continental origin. Extant velocity models also support the hypothesis. Regardless, there is a large range among extant backstop age interpretations and further investigation is required.

2.6.4. Implication for Tsunamigenic Earthquakes

How the structure of the Sumatra accretionary wedge links the 2004 great earthquake and its unusually large accompanying tsunami is still not well established. *Gulick et al.* [2011] and *Geersen et al.* [2013] have proposed that due to the thick and potentially indurated nature of incoming sediments, coseismic rupture propagated closer to the trench, enhancing tsunamigenic potential. Our study suggests that the wedge interior, containing a strong backstop inboard and possibly a dynamic backstop outboard, along with rapidly consolidating accreted sediment near the deformation front [*Gulick et al.*, 2011], may together act as a rigid block co-seismically. Effectively, such a model extends velocity-weakening rheology seaward, allowing for coseismic rupture closer to the Sunda Trench and thereby enhancing tsunamigenic potential.

2.7. Conclusions

Structural and morphology interpretations of the accretionary prism offshore of northern Sumatra, based on both seismic and bathymetric data, allow us to observe and infer features within the region of maximum slip for the 2004 Sumatran-Andaman great

earthquake that may have a bearing on tsunamigenic potential. First, differences in strike between the deformation front and ridges within the plateau are suggested to be the result of slope failures occurring along the deformation front, which occur more extensively in the southern portion of the study area. Second, the existence of tilted sediments in piggyback basins suggests recent and continuing activity of flanking thrust faults; ongoing deformation/shortening of the shallow prism is indicated. Third, we observed three prominent structural zones, which are consistent along-strike (Fig. 2.5 and Table 2.2): 1) landward-vergent folds closer to the Sunda Trench, 2) seaward-vergent folds characterizing the eastern plateau towards the Aceh Basin, and 3) an intervening region of mixed-vergent folds. Such an extended region of landward vergence is rarely observed in accretionary prisms around the world; we conclude that this zone suggests the existence of a seaward-dipping backstop. Fourth, we can infer the likely geometry of such a backstop (Fig. 2.6): a) the seaward tip of this backstop lies under the bathymetrically shallowest portion of the wedge (Fig. 2.5), and b) the roof of the backstop under the Aceh Basin is along an acoustically strong reflector at a depth of ~6 s. This backstop may be composed of continental crust of the Sunda Block, or an older, lithified and metamorphosed sedimentary block from a time of earlier accretion. We also allow for the possibility of a dynamic backstop located seaward of the rigid backstop, with a gradient of lithification increasing landward from the trench, to aid in explaining the slope and position of the outermost wedge front.

The existence of a strong inner wedge, based on its morphology and shallow structure, the presence of well-lithified sediment near the deformation front, and a consistent landward vergence zone inboard of the deformation front, all suggest that the northern Sumatra wedge could act as a solid translatable block during an earthquake, allowing rupture energy to propagate toward the Sunda Trench. Other accretionary

prisms that exhibit similar morphology, such as a wide forearc and landward vergence zone, occur in at least portions of the margin of Cascadia and southwest Alaska. We speculate that these margins are especially prone to shallow updip slip during major earthquakes, and is thus prone to damaging tsunamis.

Chapter 3: Evidence for Seafloor Deformation from the 2004 Sumatra-Andaman Earthquake

Abstract

Following the 2004 Sumatra-Andaman great earthquake (Mw 9.1), multiple geophysical surveys were conducted to gain a better understanding of the behavior and mechanism of the earthquake rupture and tsunamigenic event. We present the first study of seafloor depth and slope changes offshore of northern Sumatra, within the region from the northwest of northern Sumatra to west of Simeulue Island, where co-seismic rupture may have reached the Sunda Trench. Pre-earthquake data, from Dec 1997-Jan 1998, and the post-event data, from two surveys in Jan-Feb 2005 and Jul-Aug 2008, have been compared to show such differences. Because of uncertainty in water velocities of the 1998 data, we apply a static vertical shift to the 1998 survey data relative to the 2005 and 2008 surveys using areas seaward of the deformation front and within the Aceh Basin (where no vertical shifts are expected between surveys) for calibration. Using a cell size of 100 m, we focus our observation on two 20 km-long, NE-SW transects comparing the 1998 data with the more recent surveys of the toe of the accretionary prism. We observe evidence of prominent mass failures, which we presume are related to the 2004 earthquake. We also observe vertical shifts interpreted to be motion of thrust faults near the trench also related to the earthquake and responsible for one of the mass failures. Our data suggest that due to the 2004 rupture reaching near the accretionary prism toe, landward-verging thrust faults slipped in response to this stress within two months of the megathrust earthquake. This study highlights the need to establish fundamental time series data sets for mitigation efforts in hazard-prone areas.

3.1. Introduction

Recent great earthquakes such as the 2004 Sumatra-Andaman (Mw 9.1) and 2011 Tohoku-Oki (Mw 9.0) events have heightened the need to re-evaluate our understanding of rupture propagation behavior and co- and post-seismic accretionary prism deformation. One way to observe seafloor deformation associated with major earthquakes is by comparing bathymetric data sets acquired before and after the seismic event. Such an investigation was applied to the rupture zone of the Tohoku-Oki event; from observable bathymetric and subsurface changes, several studies show that seismic slip reached the Japan Trench [*Fujiwara et al.,* 2011; *Kodaira et al.,* 2012; *Strasser et al.,* 2013; *Kawamura et al.,* 2014]. Other studies of the 2011 event used time series bathymetric data to map seafloor changes and infer mass-wasting failures, including slumps [*Kawamura et al.,* 2012; *Strasser et al.,* 2013; *Kawamura et al.,* 2014; *Tappin et al.,* 2014], which they proposed as a cause of tsunamigenesis. However, studies of the 2010 Maule (Mw 8.8) event, where landslides are observed during inter-seismic period, show that time series bathymetric studies observed no submarine landslide related to the event [*Chadwell et al.,* 2010; *Weinrebe et al.,* 2010], except for small (cm thick) slide caused by the aftershocks [*Völker et al.,* 2011] found in core samples.

Northern Sumatra has experienced great earthquakes in the past (*i.e.,* 1394, 1450 and 1861) [*Natawidjaja et al.,* 2004; *Sieh et al.,* 2015] and is likely to experience major earthquakes in the future [*McCaffrey,* 2009]. The 2004 (Mw 9.1) and 2005 (Mw 8.7) events were the first major earthquakes in this region whose effects have been observed with modern technologies, such as global GPS networks, the GRACE and altimetry satellites. In addition, multiple geophysical surveys were conducted offshore of northern Sumatra subsequent to the 2004 seismic event. These studies show that the northern Sumatra

accretionary prism adjacent to the Sunda Trench is composed of a range of structures, such as landward- and seaward-vergent folds and piggyback basins filled with fanning/syn-tectonic sedimentary strata [*Karig*, 1977; *Henstock et al.*, 2006; *Sibuet et al.*, 2007; *Graindorge et al.*, 2008; *McNeill and Henstock*, 2014]. Moreover, predominantly landward-vergent folds extend for up to 70 km from the deformation front [*Frederik et al.*, 2015].

A bathymetric survey of this region by the British Royal Navy in early 2005 identified seafloor disturbances possibly linked to the 2004 earthquake [*Henstock et al.*, 2006], such as fault scarps along the slope facing the Sunda Trench. They proposed that co-seismic slip may have extended close to the Sunda Trench; this hypothesis has since been supported by both slip models and seismic reflection studies [*Ammon et al.*, 2005; *Banerjee et al.*, 2007; *Chlieh et al.*, 2007; *Fisher et al.*, 2007; *Rhie et al.*, 2007; *Seeber et al.*, 2007; *Mosher et al.*, 2008; *Dean et al.*, 2010; *Gulick et al.*, 2011; *Singh et al.*, 2012; *Geersen et al.*, 2013]. The Sumatra Earthquake and Tsunami Offshore Survey (SEATOS) conducted in May 2005 [*Moran and Tappin*, 2005] also observed possible earthquake-related seafloor changes on the frontal slopes at the prism toe, but no changes landward (*i.e.*, to the east) [*Moran et al.*, 2005b; *Moran et al.*, 2005a]. Within the prism toe region, a JAMSTEC survey conducted in early 2005 [*Seeber et al.*, 2007] also identified mass-wasting features and noted suspended sediment clouds, which they suggested could have been triggered by the 2004 earthquake. One of the results from the bathymetric data from "Sumatra Aftershocks" cruise [*Sibuet et al.*, 2007] conducted in July-August 2005 was a structural/seafloor map produced using aftershock distribution. They proposed four thrust faults parallel and landward (at distances of ~35, ~50, ~75, ~150 km from the Sunda Trench); two of these faults (at ~50 km and ~75 km) appeared post-seismically active.

Graindorge et al. [2008] merged bathymetric data from three surveys to produce a seafloor slope map and found steepest slopes (>15-20°) to be near the deformation front.

These studies suggest that there is not yet a consensus on seafloor deformation off northern Sumatra, specifically the existence of co- and post-seismic deformation across observed landward-vergent folds landward of the deformation front. This paper examines seafloor depth changes between December 1997 and August 2008 in this region, with the primary objectives of: 1) identifying such changes within the limits of data resolution, 2) ascertaining whether the observed depth changes relate to the great earthquakes of 2004 and/or 2005, and 3) considering the implications any such seafloor change may have for earthquake rupture processes. This is the first study of seafloor changes near the Sunda Trench that may shed light on co- and post-seismic responses in a region dominated by landward-vergent folds, where 2004 co-seismic rupture may have reached the prism toe and where seafloor deformation may be different from zones dominated by seaward-vergent folds.

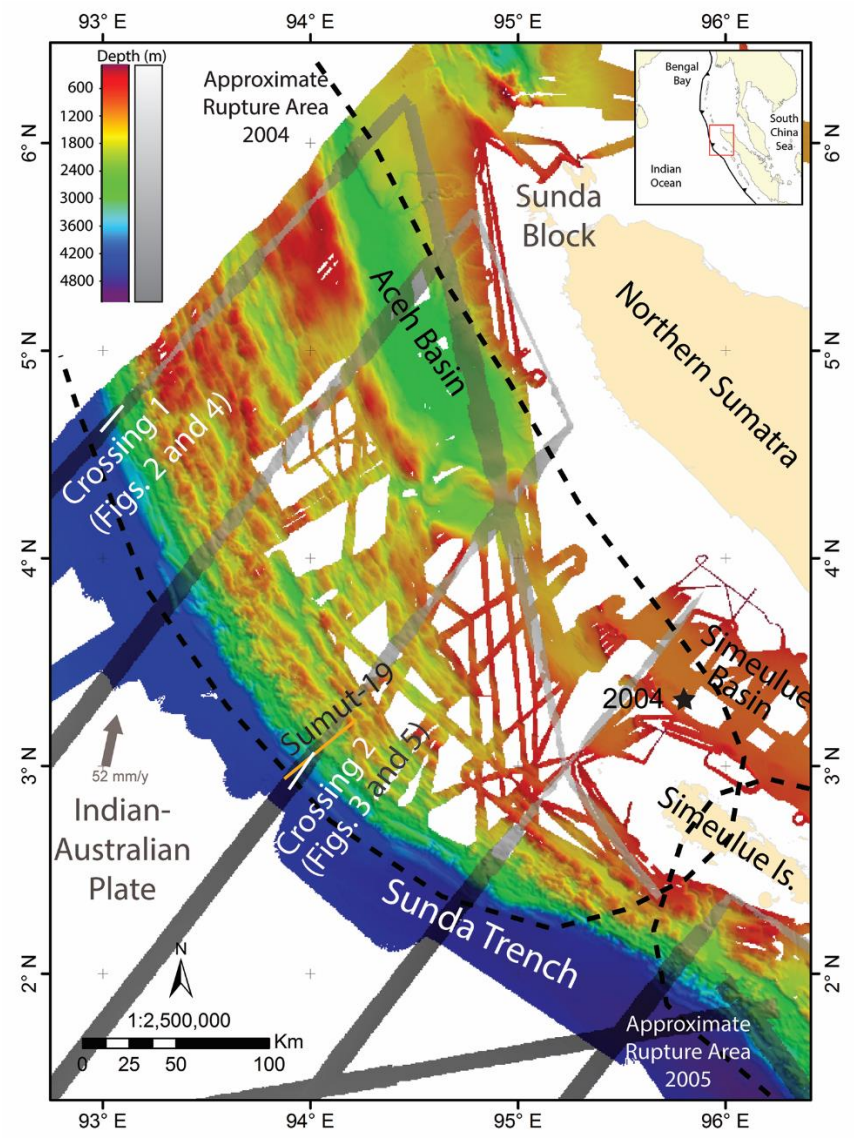

Figure 3.1: Bathymetric coverage and seismic profiles used in this investigation. Merged bathymetric data acquired between 2005 and 2009 are shown using rainbow colors (color bar, upper left). Bathymetric data acquired in 1997-1998 are in greyscale. Black star displays the epicenter of the 2004 Sumatra-Andaman earthquake. Dashed black curves show approximate 2004 and 2005 earthquake rupture zones [*Briggs et al.*, 2006]; the epicenter of the 2005 event is SE of the 2004 epicenter. Orange line is SUMUT-19 seismic profile (Figures 3.3b and 3.3c). Our investigation concentrates on the portions of the frontal deformation zone along the mid-lines of the 1997-1998 acquisition tracks, to minimize errors in the pre-earthquake bathymetric data (white lines, Crossings 1 and 2).

3.2. Data and Methodology

Data used for this research consist of multibeam bathymetry acquired before and after the 2004 earthquake (Table 3.1). Note that data acquisition by *HMS Scott* occurred before the March 28, 2005 earthquake, which provides the opportunity to investigate seafloor disturbances related to the December 26, 2004 earthquake without complicating effects from the subsequent event. We use the *Sonne-SUMUT* data, acquired in 2008, to examine longer-term post-2004 seismic effects and deformation related to the 2005 event. Figure 3.1 displays the merged bathymetric data, a compilation of data acquired between January 2005 and March 2009 sequentially by The British Royal Navy (UK), JAMSTEC (Japan), IFREMER (France), Oregon State University (USA), The University of Texas at Austin (UT, USA), and BGR (Germany). The merged results extend over the entire forearc from northwest of northern Sumatra to west of Simeulue Island. BPPT (Indonesia) acquired the pre-earthquake data in December 1997-January1998, in response to the UN Law of the Sea Convention (Table 3.1). For brevity, we use BJ/1998, SC/2005 and SU/2008 to represent data from the vessels/survey *Baruna Jaya 3* (1997-1998 acquisition), *HMS Scott* (2005 acquisition), and *Sonne-SUMUT* (2008 acquisition), respectively. For this investigation, we primarily use SC/2005 and SU/2008 data, since we want to focus on results from single surveys, not those merged from multiple surveys. We choose SC/2005 data to represent the seafloor state immediately after the 2004 earthquake and SU/2008 data to represent the seafloor state a few years after the event.

We used CARIS HIPS and SIPS to process the original SU/2008 data and CARIS format of BJ/1998 data. We cleaned these data interactively, line-by-line and swath-by-swath by removing outliers and artifacts. We downloaded the SC/2005 data from The University of Southampton-National Oceanography Centre (NOCS) (ftp.noc.soton.ac.uk/pub_sumatra/ hms_scott) in CARIS format. All of the data, prior to

editing, were set to a horizontal resolution of 100 m, a depth resolution of 1 m, and a projection datum of UTM-WGS 84, zone UTM 46N. Along the BJ/1998 track lines, we cropped the swath width to within 500 m of the track line. Within this 1000 m wide stripe, we calculated seafloor depths for a distance of up to 20 km from the prism toe. We chose two focus areas, Crossing 1 and 2 (Figure 3.1). For each focus area, we produced depth differences by subtracting newer (post-2004 earthquake) from older (pre-2004 earthquake) data.

Research Vessel	**Cruise designation**	**Dates of acquisition**	**Multibeam**
Baruna Jaya 3	Digital Marine Resources Mgmt.	Dec 1997-Jan 1998	SIMRAD EM 12
HMS Scott	Marine Scientific Research	Jan-Feb 2005	SASS IV
Sonne (SUMUT)	198/2	July-Aug 2008	SIMRAD EM 120

Table 3.1: Cruises acquiring multibeam data used in this investigation.

For the BJ/1998 data, several problems were encountered during processing:

1. No tide data are available; however, considering the depth of the study area, >2500 m (prism toe region) and tide range is 0.7 m from tide gauges along coast of northern Sumatra and Simeulue Island, we concluded that the lack of the tide data would not contribute to a significant water depth error. Therefore, we applied a zero tide function.
2. No XBT data are available. The SIMRAD 12 system utilizes a data logging software that applies a sound velocity correction to the data during recording.

Comparison between BJ/1998 and SC/2005 data shows that the BJ/1998 data are consistently deeper than SC/2005 data everywhere. We suspect a potential static shift of the BJ/1998 data that we presume is a result of water velocity uncertainty. To correct that, we shifted the BJ/1998 data by applying a constant value (0.9976) derived from the average depth difference identified at six locations (seaward of the deformation front and within the Aceh Basin) of overlapping BJ/1998 and SC/2005 track lines. Appendix B illustrates the locations for determining this constant value. Since all six locations are above the fault that moved during the 2004 great earthquake, we acknowledge that the shifted BJ/1998 data may still contain errors.

3. Presence of data artifacts, such as ripples; we believe that these occur because of the low sampling rate of ship motion in the BJ/1998 data set. At the survey speed of ~8-9 knots, sonar data were acquired only once per 9-13 s, while navigation data were recorded once per second. We smoothed the heave, pitch and roll values in an effort to minimize these artifacts. Appendix C describes our approach.
4. There is no vessel configuration file; the depth surface created has pronounced effects from hull listing when compared to those of newer data. We corrected this manually by adjusting the roll values of each transducer by $\leq 2°$. Appendix D illustrates this process. These corrections are in the end insufficient to remove the listing effect, especially for the outer beams. This is a primary reason why for this study we only use data within 500 m either side of the track line for the BJ/1998 data since depth uncertainty increase with distance from the central swath.

We examined the BJ/1998 data between 1° and 2.5°N and between 3° and 4°N and find that there are many bad depth readings, probably due to rough sea conditions, in

addition to the problems about the dataset mentioned above. We also tested the depth accuracies of the BJ/1998 data compared to the newer (SC/2005 and SU/2008) data. The average standard deviations over a relatively flat area (~3000-3040 m) covered only by BJ/1998 and SC/2005 data are 6 and 2.1 m, respectively. However, the depth accuracies for BJ/1998, SC/2005, and SU/2008 are larger (18-24 m) in two other locations shown in Appendix B. We presume that the lower standard deviation is because measurements are made only along the center swath of SC/2005 track lines. In addition, the small (~4 m) average difference between BJ/1998 and SC/2005 values is probably due to application of zero tide and/or differences in the water velocity corrections between these surveys.

Ultimately, we use the adjusted depth and depth difference for our investigation of potential earthquake-related seafloor changes because of the corrections that we were forced to apply to the pre-earthquake BJ/1998 data. We used ArcGIS to adjust the BJ/1998 data and present the depth differences. We found that over flatter areas, depth (vertical) values of BJ/1998 still vary ±20 m while for SC/2005 depth values vary a few meters only; we use this ±20 m to represent our depth uncertainty for BJ/1998 data. We also plot depth profiles along the central BJ/1998 track lines from the depth adjustment to BJ/1998 data to help illuminate the observed seafloor changes. We tried to avoid using post-earthquake data that occur along the edges of any swath, or at locations where the survey vessel is turning, because depth errors in those locations are always larger.

We concentrate our analysis on two regions, Crossings 1 and 2 (Figure 3.1), along the central swath-width of BJ/1998 (pre-earthquake) data that intersect SC/2005 and SU/2008 post-earthquake data. The white lines near the Sunda Trench in Figure 3.1 represent these two data sets of NE-SW observations; they extend up to 20 km landward from the toe of the accretionary prism.

In this paper, we investigate co- or post-seismic deformation using two overlapping data sets; the first location is Crossing 1, where we measure effects of the 2004 earthquake using BJ/1998 as pre-earthquake and SC/2005 as post-earthquake. The second location is Crossing 2 where we use BJ/1998 as pre-2004 event, SC/2005 as the post-2004 event, and SU/2008 as the post-2005 event. Even though Crossing 2 is outside of the 2005 rupture zone (Figure 3.1), we would like to investigate whether any deformation occurred due to the shaking during the 2005 earthquake. In addition, we want to investigate any long-term seafloor effects (i.e., depth changes) from the 2004 event. We measure depth changes by subtracting post-earthquake from pre-earthquake depth values. For example, in Crossing 1, the data pair is BJ/1998 as pre-2004 event and SC/2005 as post-2004 event; negative depth changes correspond to shoaling and positive is deepening. To verify our observed depth changes, we attempt to validate our findings using subsurface interpretations along one published multichannel seismic (MCS) profile, SUMUT-19, that crosses a frontal fold at a distance of ~7 km from Crossing 2 (Figure 3.1). UT/Austin acquired 1,250 line-km of these data using a source array of 12 G-guns (total volume 5,420 in^3), a 2.4 km-long streamer containing 192 channels, towed at a depth of 10 m during the Sonne-198/2 SUMUT survey (Table 3.1). Shot interval was 20 s ± 0.2 s. SUMUT recorded 16 s of data with a 2 ms sampling interval. We used MCS data processed through post-stack time migration [*Gulick et al.*, 2011; *Martin et al.*, 2014].

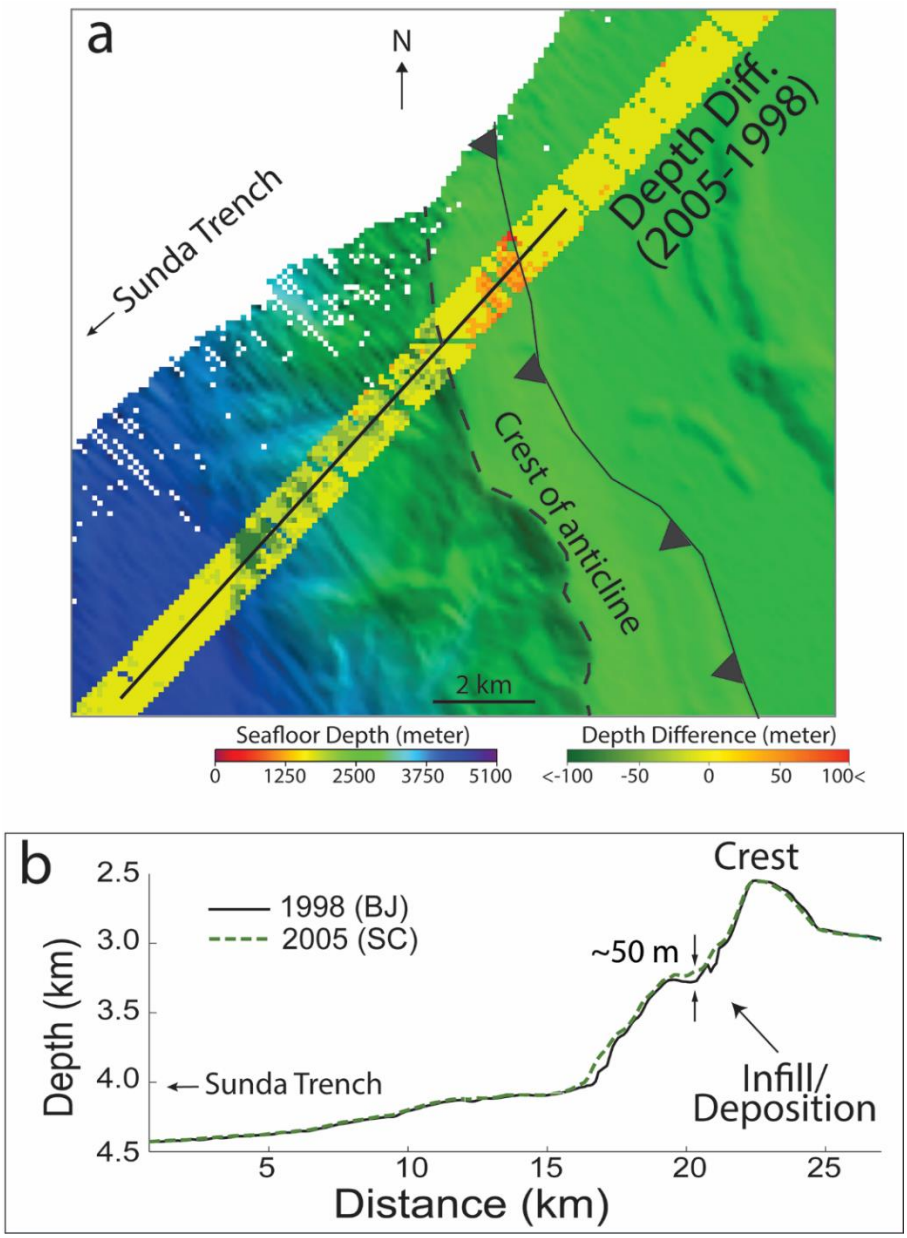

Figure 3.2: Seafloor depth and depth changes along Crossing 1 (refer to Figure 3.1 for location). Dashed line represent crest of the frontal fold. (a) 2005 (SC) bathymetric surface with NE-SW transect of seafloor depth change between 1998 and 2005 for a distance of ~20 km. Within this transect, green indicates shoaling and red represents deepening; depth differences of ± 20 m is shown in yellow, which occur mostly on flatter areas. (b) illustrates depth profile along the central track (black line, Figure 3.2a).

3.3. Observation

The seaward flank of the frontal fold on the north (Crossing 1, Figure 3.2a) exhibits rugged terrain, presumably due to widespread erosion/slumping. At the deformation front, underthrusting of sediments [*Kopp et al.,* 2008], compression, and frontal accretion result in steepening of slopes. Oversteepened slopes are prone to failure [*Piper et al.*, 1999; *Graindorge et al.*, 2008; *Kopp et al.*, 2008; *Strozyk et al.*, 2010]. Other possible causes for submarine landslides include seismic loading, existence of a high pore pressure layer, and rapid accretion and under-consolidation [*Locat and Lee*, 2002]. Along the depth difference transect, we see areas of shoaling (green in Figure 3.2a), suggesting deposition zones, are located more on the seaward flank and areas of deepening (orange in Figure 3.2a) are on the landward flank of the anticline. Yellow color represents depth difference ± 20 m that mostly located on the flatter areas; we use this value to represent our depth uncertainties. On the seaward flank of this frontal fold, along the depth profile in Figure 3.2b, we see prominent shoaling at ~17 km and ~20 km occurred between 1998 and 2005. Depth changes at ~17 km may be ignored because it is within a region of erroneous BJ/1998 depth data. However, a prominent depth change occurs at ~20 km of ~ 50±20 m; this depth difference suggests infilling of a trough.

In the study area on the south (Crossing 2), we also observe a deepening of ~40±20 m (Figure 3.3a, orange), which occurred between 1998 and 2005 on the landward side, near the base of the fold labeled 1. This region of deepening is adjacent to an area of shoaling ~45±20 m (Figure 3.3a, light green).

In addition to a bathymetric difference map, we show seismic line SUMUT-19 that images the subsurface. Along the frontal fold labeled 1, SUMUT-19 transect at location ~7 km from the bathymetric transect (Figure 3.3a and inset map, Figure 3.3b). Based on this

seismic line, we suggest that frontal fold 1 to be landward vergent and draw an interpreted thrust fault extending from the décollement to the seafloor at CDP ~1,400 (Figure 3.3b). Figure 3.3c illustrates the subset of SUMUT-19 (black rectangle, Figure 3.3b). Based on the bathymetric difference map and this seismic line, we suggest that the ~40±20 m deepening is an evidence of slumping and the adjacent shoaling of ~45±20 m is the deposition site (Figure 3.3c). The discontinuous reflectors of the seafloor (zoomed-in figure, upper right, Figure 3.3c) indicate these slumping and deposition. Depth profiles for 1998 (black), 2005 (green) and 2008 (orange) is plotted above the seismic profile in Figure 3.3c. These depth profiles also illustrate the evidence of slumping and deposition that occurred between 1998 and 2005. Remember that the bathymetric transect and the seismic profile map the fold labeled 1 at different locations of the fold (~7 km apart, inset in Figure 3.3b), but both exhibit similar slope failure and deposition nearby. The slumping/erosion is probably because of the faults' motion to oversteepen the gradient of the slope resulting in the observed collapse. The seismic profile SUMUT-19 was acquired in 2008 at the same time as the 2008 bathymetric data. On the depth profiles in Figure 3.3c, we find no appreciable depth difference between 2005 and 2008 suggesting no significant slumping occurred during that period.

We perceive another evidence for erosion/slumping in Crossing 2, which is at the edges of a large interpreted mass wasting feature/gully complex that crosscuts the anticline labeled 3 (Figure 3.3a). Over the crest, we observe a sizeable area of deepening (~45±20 m, orange) between 1998 and 2005, along the edges of the gully. On the seismic profile (Figure 3.3b), under the anticline labeled 3, we interpret thrust fault and other blind (non-surfacing) faults flanking this fold at CDPs 2,800-3,600. Thrust motion of these faults increasing the slope gradient may result in the observed erosion.

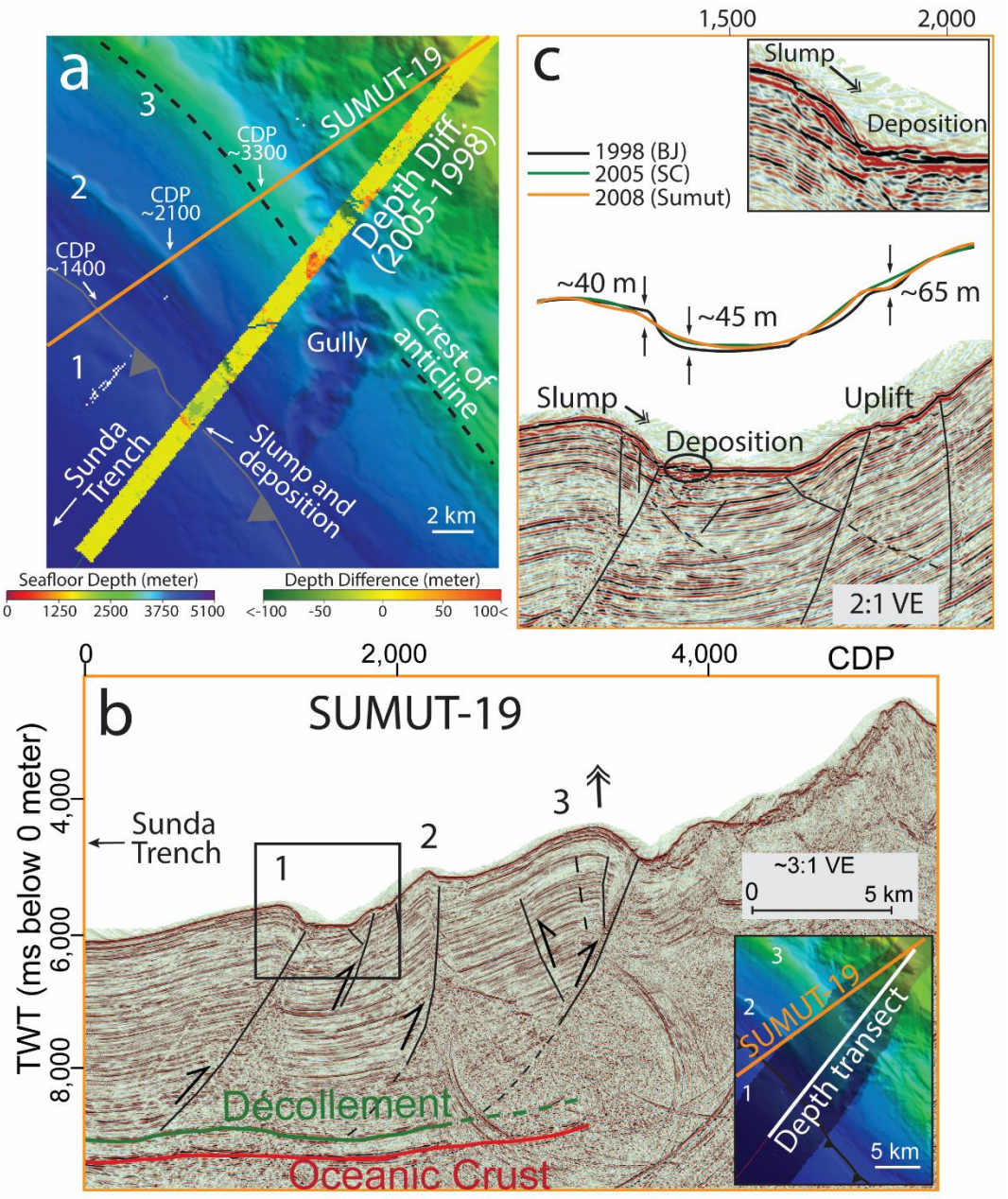

Figure 3.3: Seafloor depth and depth changes along Crossing 2. See Figure 3.2 for caption and description of annotation on Figure 3.3a. (b) Seismic profile SUMUT-19 (refer to Figure 3.1 and bathymetric inset for location). (c) Subset of the seismic profile around the frontal fold (labeled 1) with depth profiles of BJ/1998, SC/2005, and SU/2008 above the seismic profile. Figure on the upper right corner shows a zoom-in of the slump and deposition area.

Within Crossing 2, in addition to erosion, we observe a zone of shoaling of ~65±20 m (Figure 3.3a, green), on the base of the seaward flank of fold labeled 2 that occurred between 1998 and 2005. We interpret surfacing thrust faults at CDPs ~1,800 and 1,950 (Figures 3.3b and 3.3c). Motion of these faults may be responsible for the depth changes observed. Note that these erosion, deposition and uplift observations are all above our depth uncertainty of ±20 m and are the first time-series bathymetric measurements from the 2004 Sumatra-Andaman earthquake region.

3.4. Discussion

Some slip models show that the 2004 coseismic rupture may have extended toward the toe of the accretionary prism [*Ammon et al.*, 2005; *Ishii et al.*, 2005; *Hirata et al.*, 2006; *Banerjee et al.*, 2007; *Rhie et al.*, 2007; *Hu and Wang*, 2012]. According to these models, our Crossings 1 and 2 are located within the region of maximum slip (3-5° N). Our observations of shoaling and deepening, which we suggest as evidence of uplift and slope failure on and around the frontal folds lead us to propose that these seafloor deformations occurred either coseismic or post-seismic of the 2004 event. Specifically, we propose that the coseismic shaking have caused the slope failure on Crossing 1 and the combination of motion of thrust faults and coseismic or post-seismic shaking caused the deformations in Crossing 2 and proximal seismic image.

Our study area is also within the location proposed as the source of the tsunami from satellite altimetry [*Hirata et al.*, 2006] and one of the dual source tsunami from a combination of coastal tide gauge and satellite altimetry [*Fine et al.*, 2005]. The bathymetry (Figures 3.2a) illustrates numerous presumed canyon-like erosion features on the seaward-dipping slope of the frontal fold, facing the Sunda Trench. Such erosional feature is the result from multiple cycles of erosion [*McAdoo et al.*, 2004]. Submarine slumps/landslides

have been observed in accretionary prisms worldwide, and have also been proposed as a cause of tsunami [*Goldfinger et al.*, 2000; *Tappin et al.*, 2001; *Tappin*, 2010; *Kawamura et al.*, 2012; *Tsuji et al.*, 2013; *Kawamura et al.*, 2014]. Other observed causes of changes in the deformation front include seaward re-deposition of accreted sediment [*Kodaira et al.*, 2012; *Strasser et al.*, 2013], fault activity [*Moore et al.*, 2007], and/or gravitational instability caused by earthquakes [*Fujiwara et al.*, 2011; *Kodaira et al.*, 2012].

While we cannot ascertain whether the observed slumping, which we suggest is in response to motion of the interpreted thrust faults as the source of the tsunami, if these deformations occur co-seismically, they may imply that the 2004 rupture likely extended toward the prism toe. The 2004 tsunami may be the combined results of earthquake shaking, motion of individual thrusts, and slumping.

3.4.1. Slope Failure

There are several factors that can instigate submarine slides, such as rapid deposition, seismic loading, and slope gradient of seafloor [*Hampton et al.*, 1996; *McAdoo et al.*, 2004; *ten Brink et al.*, 2009b; *Strozyk et al.*, 2010]. Furthermore, *Urgeles and Camerlenghi* [2013] propose the existence of a subsurface high pore pressure layer may promote slope instability. In submarine slides, the initiation may occur on slope gradient as low as 5° [*ten Brink et al.*, 2009a; *Urgeles and Camerlenghi*, 2013] when combined with shaking from large earthquake [*McAdoo et al.*, 2004; *Tappin et al.*, 2007]. Along Crossing 1 (Figure 3.2), we observe more depth changes on the seaward flank of the frontal fold than on its landward flank. The seaward flank consist of slopes up to 34° which may be the combined result of slope oversteepening due to underthrusting of sediments [*Kopp et al.*, 2008], frontal accretion, and/or compression. We also observe a trough/basin filled by ~50±20 m sediment between 1998 and 2005 (Figure 3. 2b). This landslide may reflect the

horizontal and vertical movement at the prism toe during the earthquake [*Fine et al.*, 2005; *Banerjee et al.*, 2007; *Rhie et al.*, 2007; *Seno and Hirata*, 2007] and may contribute to the cloud of suspended sediment along the prism toe reported during the ROV observation [*Seeber et al.*, 2007] ~100 km south of Crossing 1.

There are two published seismic profiles near Crossing 1. Fisher et al. (2007) use a high-resolution single-channel seismic profile; ~20 km to the north of Crossing 1, to propose that, during the 2004 event, deformation occurred out to the prism toe, leading to tsunamigenesis. *Singh et al.* [2012] using a deep-penetration profile, ~30 km to the south of Crossing 1, interpreted thrust faults flanking the frontal fold. If we can argue that their first two folds (CDP ~1,500 and ~1,600 in Figure 3.3a of *Singh et al*. [2012]) are landward-vergent, and that associated landward-verging thrusts either moved during the 2004 event or moved post-seismically to cause the observed ~50±20 m landslide, then the slope failure in Crossing 1 may also be triggered by fault slip.

Sultan et al. [2009], from core samples of a frontal fold at ~60 km south of Crossing 1, showed that the upper layer (< 6 m) is highly consolidated sediment and contain high pore pressure layer that may be the result of recent seismic event such as the 2004 great earthquake. They also show evidence that series of slope failures have occurred on the seaward flank of the frontal fold. While their core sample locations are not along the same frontal fold where we observe the slope failure (Figure 3.2), their study give insight that on our study area (Crossing 1), excess pore pressure layer probably exist as well and that the great earthquake possibly together with reactivation of landward verging thrust trigger the observed slope failure.

3.4.2. Thrust Fault Slip

Motion of a fault may promote slope instability [*Hampton et al.*, 1996; *McAdoo et al.*, 2004; *Tappin et al.*, 2007]; for example, co-seismic fault slip during the Tohoku-Oki event produced large slumping [*Kodaira et al.*, 2012]. Within Crossing 2, we observe two potential examples of fault slip. The first one is on the landward flank of the frontal fold labeled 1 (Figures 3.3). We observe a deepening of ~40±20 m (orange, Figure 3.3a) next to a region of shoaling of ~45±20 m (light green, Figure 3.3a). We propose mass failure/slumping and associated deposition between 1998 and 2005 on the landward flank of the frontal fold to be caused by reactivation of the interpreted thrust faults, based on subsurface stratigraphic discontinuity and the disturbed seafloor reflector (Figures 3.3b and 3.3c).

The second location for mass wasting due to fault slip is on the fold labeled 3, around the edges of a large gully (Figure 3.3a). On SUMUT-19 (Figure 3.3b), under fold labeled 3, we interpret a thrust fault down to the interpreted décollement and several blind thrust faults. We propose that reactivation of these faults increased the slope gradient and probably in combination with the shaking during the 2004 seismic event, resulting in the slope failure observed.

Adjacent to the zone of slumping on the landward flank of the fold labeled 1, where we observe a zone of deposition (Figure 3.3c). We estimate the area of deposition to be ~700 x 800 m. If the maximum thickness of the deposit is ~45±20 m, then the volume deposited is 0.03 km^3, which is considered a small volume for submarine slide [*Clare et al.*, 2014]. However, the seismic profile SUMUT-19 transects the same frontal fold at ~7 km NW of the bathymetry transect (Figure 3.3b, bathymetry inset). Note that both seismic and depth profiles show evidence of slumping and deposition (Figure 3.3c). If we assume that such slumping to occur all along this ~7 km distance, then the average volume

deposited is ~0.25 km^3, which is considered a large submarine slide [*Clare et al.*, 2014]. Crossing 2 is ~200 km from the 2004 epicenter (Figure 3.1) and is within the area proposed as the zone of tsunami genesis [*Fine et al.*, 2005; *Hirata et al.*, 2006]. Although we cannot constrain whether this slumping/deposition contributed to the 2004 tsunami, we interpret that the slump was caused by motion of the thrust faults in response to the 2004 event in addition to the shaking during the event. Moreover, such volume of landslide over long distances may also contribute to the high suspended sediment observed by *Seeber et al.* [2007] at ~120 km from Crossing 2.

3.4.3. Long-term Changes

Crossing 2 is mapped in 1998 (BJ), 2005 (SC) and 2008 (SU). Note that SC/2005 data were acquired in Jan-Feb 2005. This gives the opportunity to observe seafloor changes related to the 2004 event as well as investigate its long-term changes and/or changes related to the March 2005 earthquake. Our observation show that changes in depth are more prominent between 1998 and 2005 and minimal/no-additional changes between 2005 and 2008 (Figure 3.3). These observations suggest that within the southern portion of the 2004 earthquake rupture area, seafloor deformation occur predominantly co-seismically or within the two months after the 2004 event with little/no-additional long-term effects, and minimal/no changes is caused by the 2005 earthquake, which agree with long-term coastal GPS observation [*Gunawan et al.*, 2014].

3.4.4. Proposed Seismogenic Behavior Model

Existing models propose that during the 2004 great earthquake: 1) the prism wedge moved seaward as a solid block and deforming the prism toe, which increased the tsunami potential [*Fisher et al.*, 2007; *Gulick et al.*, 2011; *Frederik et al.*, 2015], 2) The co-seismic rupture energy traveled along a major thrust fault and surfaced within the prism plateau;

post-seismic slip then occurred along the subsequent thrust faults seaward of the first one [*Sibuet et al.,* 2007], and/or 3) the co-seismic rupture energy traveled along one of the seaward verging thrusts and surfaced at the toe of the prism [*Henstock et al.,* 2006]. All these proposed models suggest that surface deformation should occur near the toe of the prism, co-seismically or post-seismically.

Figure 3.4 shows models for co-seismic and post-seismic rupture patterns relevant to the southern portion of the 2004 great earthquake offshore of northern Sumatra. Based on our observation along two transects, we propose that during the 2004 great earthquake, the co-seismic rupture energy within the region of high stress traveled beneath the strong wedge (Figure 3.4a) continued under the highly consolidated sediment on the outer wedge and propagated towards the prism toe. At the toe, stress transferred to the region of compacted sediment, hence lengthening the velocity-weakening zone [*Gulick et al.,* 2011]. The thrust faults within the landward vergence zone then slipped increasing the adjacent slope gradient and resulting in the observed slump, deposition, and uplift (Figure 3.4b, inset). Co-seismic fault reactivation on the prism toe is reported for the Tohoku-Oki event [*Kodaira et al.,* 2012] that result in slumping. Our model depicts the landward-verging faults motion as post-seismic; however, their reactivation might also occur co-seismically considering the long rupture period [*Banerjee et al.,* 2007; *Chlieh et al.,* 2007].

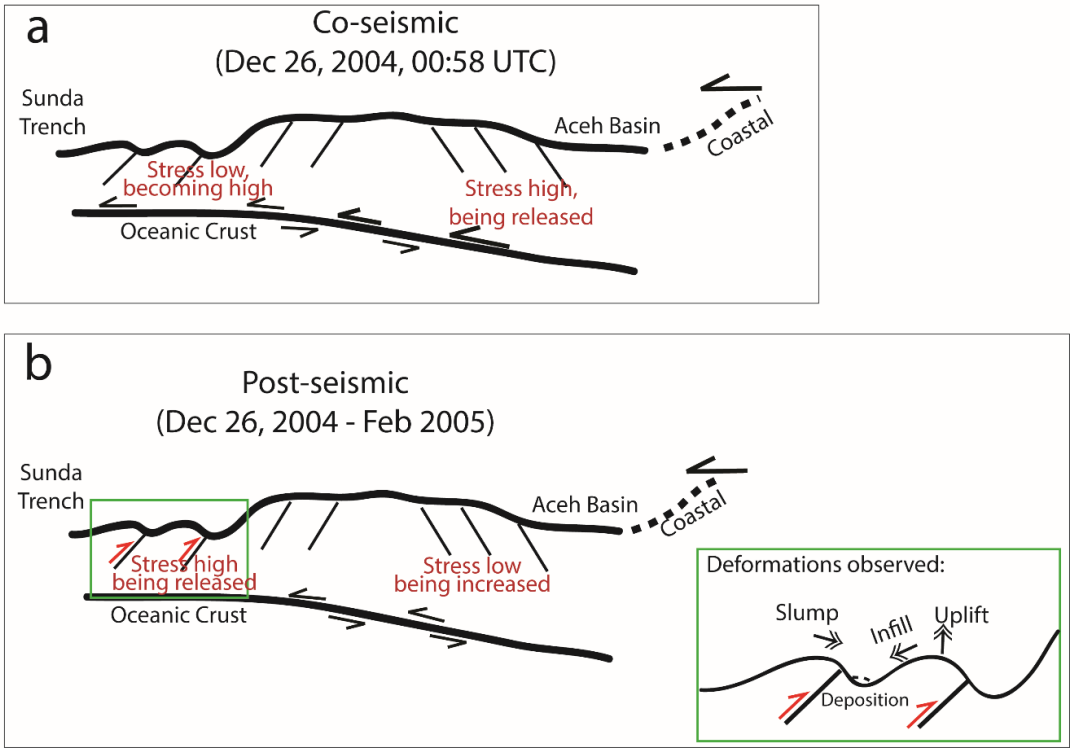

Figure 3.4: Seismogenic behavior models and post-seismic seafloor deformation proposed. Black arrows represent sense of direction for overriding and subducting plates; red arrows represent post-seismic thrust faults activity. Green rectangle displays types of deformation observed within our three study areas.

3.4.5. Size and Distribution of Submarine Slide

Our observation of seafloor depth changes along two transects crossing the southern portion of the 2004 Sumatra rupture area show evidence for mass wasting that may occur either co- and/or post-seismically and from thrust faulting activity. The magnitudes of these changes are larger than the published studies of the 2004 event: vertical displacement <6 m [*Fine et al.*, 2005; *Chlieh et al.*, 2007; *Seno and Hirata*, 2007] based on coastal tide gauge, global GPS network, and satellite altimetry data. Our depth uncertainty may be up to ±20 m and the observed depth changes in the form of slumping and deposition likely related to the 2004 earthquake are still in the scale of 10s of meters or in the form of

landward vergent thrusting in response to the seismic event. We argue that our observed seafloor deformations are realistic considering the seafloor changes during the Tohoku-Oki event based on time series bathymetry are also in the 10s of meters [*Strasser et al.*, 2013; *Kawamura et al.*, 2014]. Crossing 2 in the south shows mass wasting the size of 700 m by 800 m, which we infer to occur along a distance of 7 km from nearby the seismic SUMUT-19 profile. These submarine slide areas may not be as large as that observed in Tohoku [*Kawamura et al.*, 2012; *Kodaira et al.*, 2012; *Strasser et al.*, 2013; *Kawamura et al.*, 2014], however, our observations suggest that the 2004 earthquake caused these mass wasting in agreement with the concentrated suspended sediment observed by *Seeber et al.* [2007].

Studies within the Maule M_w 8.8 earthquake rupture area, where non-seismic related submarine slide have been recorded, did not report observable landslide related to the 2010 seismic event [*Chadwell et al.*, 2010; *Weinrebe et al.*, 2010; *Völker et al.*, 2011]. The small size of submarine slide or the lack of in relation to large earthquake is reported from other margins as well [*Chaytor et al.*, 2009; *Talling*, 2014]. On the contrary, submarine slide studies on Tohoku found evidence of large slumping in multiple areas [*Kawamura et al.*, 2012; *Tappin et al.*, 2014] related to the 2011 event. It is possible that within our study area, mass wasting have also occurred in other areas within the deformation zone, but they are not mapped by the BJ/1998 data. There is also a possibility that during the 2004 major earthquake, slope failures are not widespread as proposed by *Sumner et al.* [2013] from core samples and studies of other margins [*Völker et al.*, 2011; *Talling*, 2014] due to seismic strengthening [*Strozyk et al.*, 2010; *Sawyer and DeVore*, 2015]. This further emphasis the importance of time series base maps for natural hazard studies.

3.5. Conclusions

This paper presents the first study offshore of northern Sumatra of seafloor changes based on bathymetric data collected pre- and post- the great earthquakes of 2004 and 2005. Using data acquired in 1998, 2005, and 2008, we investigate seafloor deformation, which we have related either to co- and post-seismic 2004 effects, or to longer-term post-2004 and/or March 2005 great earthquake effects. This study offshore of northern Sumatra, within a zone of landward vergence, shows locations of mass wasting and recent thrust faults activity in the deformation front, where seismic rupture may have reached the prism toe. Our observation along the two-deformation front transects reveal that in the north (Crossing 1), gravity driven mass wasting occurred on the seaward side of the frontal fold. In the south (Crossing 2), gravity driven mass wasting occurred around the edge of a large gully, and fault motion related slumping on the landward flank of the frontal fold. On all these submarine slides, thrusting motion of the faults under each fold, in response to the 2004 earthquake, may be the cause for slope instabilities that result in the mass wasting. We acknowledge that the presence of high fluid pressure layer may increase slope instability and shaking from the earthquake may trigger the slope failure. These seafloor changes are noticeably larger between 1998 and 2005 compared to the changes between 2005 and 2008, suggesting that they occurred either co-seismically or within 2 months after the 2004 event. Investigations of changes in seafloor morphology resulting from seismic activity are generally rare, because of the lack of seafloor data before and after such events. As major destructive earthquakes occur mainly along subduction zones, this paper also highlights the need to generate necessary long time series of both bathymetric and seismic data, for hazard mitigation and to improve our understanding of great earthquake processes and effects.

Chapter 4: Sediment Characteristics and Subduction Process of Buried Seamounts Offshore of Kodiak Island

Abstract

Seamounts are ubiquitous on the oceanic plate; those situated near convergent margins will eventually undergo subduction. Using six pre-stack depth migrated MCS profiles transecting the Aleutian Trench, we investigate deeply buried seamounts offshore of Kodiak Island, within 145-155° W and 55-58° N. Topography of the subducting Pacific Plate varies owing to seamount chains and fracture zones. We observe a distinct sedimentary horizon exists in all six seismic profiles, above the average height of seamounts, which appear to be the preferred structural detachment zone. Where drilled, this horizon contains gravel-sized debris that marks the onset of intensification of Northern Hemisphere glaciation at ~2.7 Ma. The strata beneath this horizon were deposited prior to the development of the Surveyor Fan and the majority if not all these sediments eventually be subducted. Subducted seamounts cause enhanced surface slope of the accretionary prism that correlates well with the seamount's height. Our observation lead us to propose a model of subduction sequences for deeply buried seamounts offshore of Kodiak Island, which differ from the classic seamount subduction models. Prior to subduction, a proto-thrust zone forms seaward of the deformation front presumably due to convergent stress. This proto-thrust zone later becomes the new deformation front, suggesting of a significant jump of deformation front.

4.1. Introduction

Most studies of seamount subduction are based on partially buried seamount; studies of deeply buried seamounts, such as we present in this paper, are limited. Offshore of Kodiak Island, there are two chains of seamounts, the Kodiak-Bowie and Patton-Murray (Figure 4.1), with heights between 1 and 3 km above the Pacific Plate [*von Huene et al.*,

2012]. Thick sediment (<4 km) in the Aleutian Trench [*Reece et al.*, 2011; *Gulick et al.*, 2015] buried the seamounts located proximal to the trench. Interpretation of MCS profiles acquired in 1969-1970 together with DSDP Leg 18 drill sites north of the Kodiak Island show that there are two sources for the trench fill: downslope slumps and along trench axis sediment flux where the deepest deposit is ~0.6 My [*von Huene*, 1972]. *von Huene et al.* [2012] use bathymetric data and show embayment and rapid slope increase (2 km uplift) as evidence of subducted seamounts situated under the frontal slope northeast of the Kodiak Seamount (Figure 4.1). We present six pre-stack migrated seismic profiles along the Aleutian Trench and observe deeply buried seamounts at various stages of subduction.

Various studies produce numerical/analytical models on seamount subduction. From sandbox models, the incoming seamount/ridge subduction cause a shortening and thickening of the wedge resulting from the convergence [*Lallemand et al.*, 1992]. Directly ahead and above the seamount, an increase of slope gradient of the frontal prism by reactivation of thrust faults [*Dominguez et al.*, 2000]. Upon further subduction, a retreat of the deformation front resulting from slump, creating an embayment [*Lallemand et al.*, 1992; *Dominguez et al.*, 2000]. From a series of seismic profiles in the Hikurangi margin, *Pedley et al.* [2010] show a range of seamounts situated from some distance seaward of the deformation front to those already subducted. They report the effects of seamount subduction on the accretionary prism. The effects include formation of a basin within the deformation front region, development of out-of-sequence thrusts landward and above the seamount that significantly uplift the wedge, sediment subduction, and scar or large-scale sediment collapse (embayment) in the wake of the seamount. Studies in Nankai Trough, Chile Margin, and Costa Rica Margin confirm such deformations of the accretionary prism in relation to seamount subduction [*Park et al.*, 1999; *Von Huene et al.*, 2000; *Laursen et al.*, 2002; *Gulick et al.*, 2004; *von Huene et al.*, 2004]. In addition, *Bangs et al.* [2006] using

3-D seismic in Nankai Trough observed the plate boundary and proposed underplating, deepening of the décollement, to occur in the wake of a subducted seamount.

Using six MCS profiles, this paper investigates deeply buried seamounts offshore Kodiak Island that are being subducted under the North America Plate. The objective is to: 1) investigate variation of sediment thickness along the Aleutian Trench, 2) investigate development of décollement in relation to seamount size, and 3) extend our knowledge on the process of seamount subduction and its effect on the accretionary prism for deeply buried seamounts. We propose a model for such seamount subduction and the resulting deformation of the overlying accretionary prism.

4.2. Background

The Kodiak-Bowie and Patton-Murray Seamount Chains are on top of the 45 My Pacific plate and are heading toward the North America Plate at the rate of 6.4 cm/y [*Fruehn et al.*, 1999; *von Huene et al.*, 2012]. In fact, the Kodiak Seamount (part of the Kodiak-Bowie Seamount Chain), at 2.9 km above the trench sediment, is currently located in the Aleutian Trench (Figure 4.1) and is in the process of colliding with the North America Plate [*von Huene et al.*, 2012]. Along the Aleutian Trench, based on bathymetric and seismic reflection data, subducted seamounts produced frontal prism uplift and on their trailing side produced embayment on the prism toe [*von Huene et al.*, 2012].

Formation of the Aleutian Trench is the result of the Kula-Pacific Plate and the North America Plate collision. The Kula Plate converged at ~20 cm/y with Alaska starting in the Late Cretaceous (~85 Ma) at the onset of a spreading ridge between Kula-Pacific Plate [*Engebretson et al.*, 1985; *Madsen et al.*, 2006]. However, since ~43 Ma, the convergence rate has been constant along the Aleutian Trench at ~5-7 cm/y related to the ceasing of the spreading center [*von Huene et al.*, 1987].

The collision of the Yakutat microplate and Pacific Plate with the North America Plate resulted in the Mount St. Elias orogeny, which in turn produce one of the largest submarine fans, the Surveyor Fan, an area of > 300,000 km^2 [*Reece et al.*, 2011]. Figure 4.1 shows the Surveyor Channel and an estimated outline of the Surveyor Fan Sediment based on seismic reflection data [*Reece et al.*, 2011; *Gulick et al.*, 2015]. Paths to the Surveyor Fan from the St. Elias Mountain range are through the Alsek and Seward-Malaspina-Hubbard Sea Valleys, which feed the 900-km long Surveyor Channel [*Gulick et al.*, 2015]. Between the Kodiak-Bowie and Patton-Murray seamount chains, *Reece et al.* [2011] observed a NE-SW zone of extension and proposed that it created a bathymetric low that directs the Surveyor Channel towards the Aleutian Trench near Kodiak Island. Sources of sediment for the Aleutian Trench come from the Chugach and Prince William Sound Terranes as well as from Mt. St. Elias; the sediment paths are through the Bering-Bagley and Hinchinbrook Sea Valleys, and the Copper River into the eastern terminus of the Aleutian Trench [*Gulick et al.*, 2015]. Farther west, sediment that feeds into the Aleutian Trench is from the Peninsular Terrane, west of the Kodiak Island, through the Cook Inlet, Shelikof Strait, Stevenson Basin, and Albatross Basin [*von Huene et al.*, 1987].

There have been several drilling expeditions conducted in the Gulf of Alaska; Figure 4.1 displays the locations that are offshore Kodiak Island. Sites DSDP 179-182 was conducted in 1971 [*von Huene et al.*, 1973]; site ODP 887 was in 1992 [*Rea et al.*, 1992], and site U1417 was in 2013 [*Jaeger et al.*, 2014]. The expeditions reported that the age of Kodiak seamount and Giacomini seamount is 22.6±1.1 and 19.9±1.0 My, respectively [*Turner et al.*, 1973] and the ages of Patton and Murray Seamounts are 29.7±0.3 My and 27.6±0.2 My, respectively [*Dalrymple et al.*, 1987]. The seamounts are buried under the pre-Surveyor Fan sediment likely since Miocene but not fully buried until Pliocene-Pleistocene time [*Jaeger et al.*, 2014; *Gulick et al.*, 2015]; the sediment packages onlap

onto the flanks of the seamounts and successive depositions are atop the seamounts [*von Huene*, 1972].

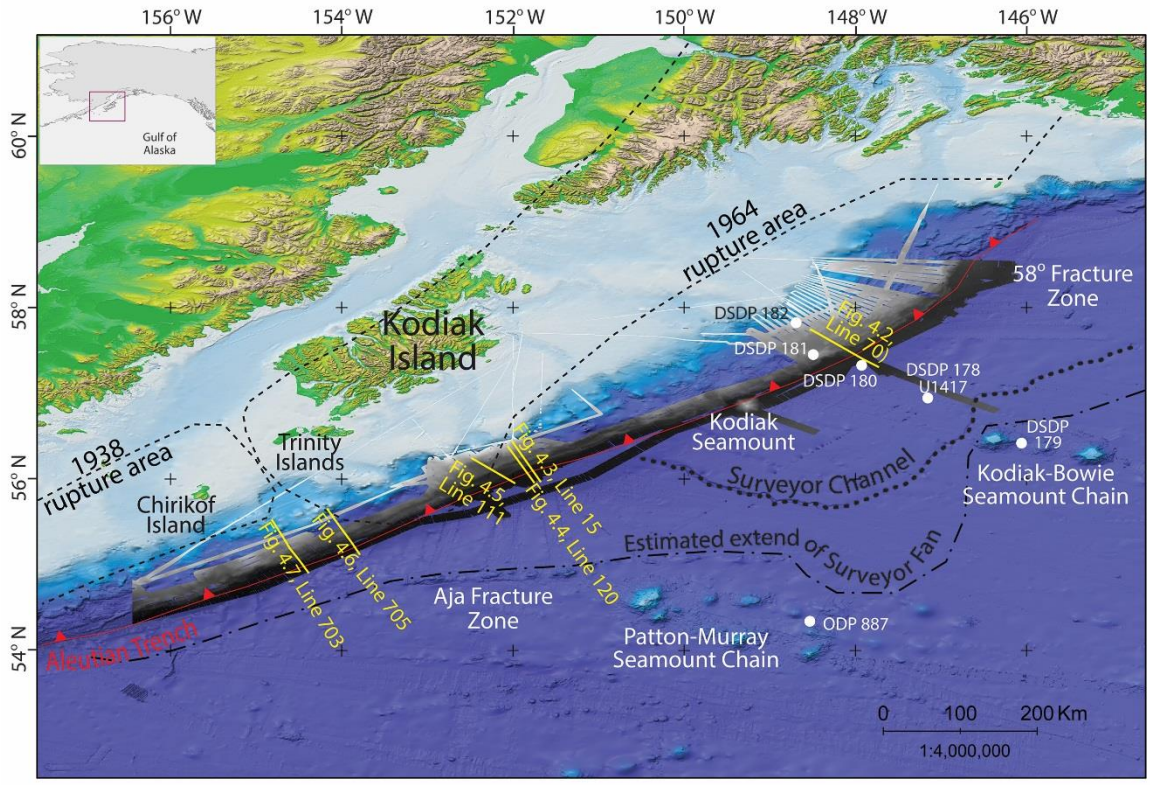

Figure 4.1: Study area offshore of Kodiak Island. Bathymetric data acquired in 1994 is in greyscale. Yellow lines are MCS transect lines and yellow dots are drill sites during DSDP, ODP, and IODP expeditions. Light blue lines are existing seismic lines not used in this study. Bold dashed black line illustrates southern portion of the Surveyor Channel. White line represents the Aleutian Trench. Dashed lines are estimated rupture zone for the 1964 and 1938 earthquakes, respectively.

We adopt the nomenclature introduced by *Reece et al.* [2011] to describe the Surveyor Fan sediment packages in our seismic profiles. Sequence Boundaries I-II and II-III are atop a series of laterally continuous reflectors representing turbidite deposits (Figure 4.2). Reflectors within Sequences II and III are more laterally continuous compared to

those of Sequence I. Sequence I was deposited prior to the formation of the Surveyor Fan; it contain hemipelagic and turbidites sediment, likely of Miocene to Pliocene in age [*Gulick et al.*, 2015]. The onset of sequences II and III are Pliocene (~2.75 Ma) and middle Pleistocene (~1.2 Ma), respectively [Morey et al., in preparation]. Along the Aleutian Trench, the base of the trench fill is ~0.6 My, based on interpretation of MCS profiles acquired in 1969-1970 together with DSDP Leg 18 drill site 180 (Figure 4.1) [*von Huene*, 1972; *von Huene et al.*, 1973]. Cores from IODP Site U1417 within the Surveyor Fan (Figure 4.2) show sediment section a little above 300 m depth, which show gravel-sized debris. This has been interpreted to represents the onset of ice rafted deposition, a response to the intensification of the Northern Hemisphere Glaciation during the Plio-Pleistocene transition (PPT) at ~2.7 Ma [*Jaeger et al.*, 2014; *Gulick et al.*, 2015]. This layer overlies bioturbated mud with interbedded diamict and it is beneath a layer of mud with clast-poor and clast-rich diamict intervals [*Jaeger et al.*, 2014].

Along the Surveyor Channel, thickness of the sediment packages varies. North of the Kodiak-Bowie Seamount Chain, *Reece et al.* [2011] found thick sediment of sequences II and III in contrast to the thick sequence I sediment found on the south of the seamount chain. Drill Site U1417 show evidence of increased sediment flux from the Mount St. Elias orogeny after the PPT, at 2.7 Ma, which show doubling of sedimentation (>10 cm/ky) within a million year [*Jaeger et al.*, 2014; *Gulick et al.*, 2015]. The sedimentation rate for Sequences I, II and III are 30-70 cm/ka, 60-120 cm/ka, and 60-140 cm/ka, respectively [*Gulick et al.*, 2015] (Figure 4.2).

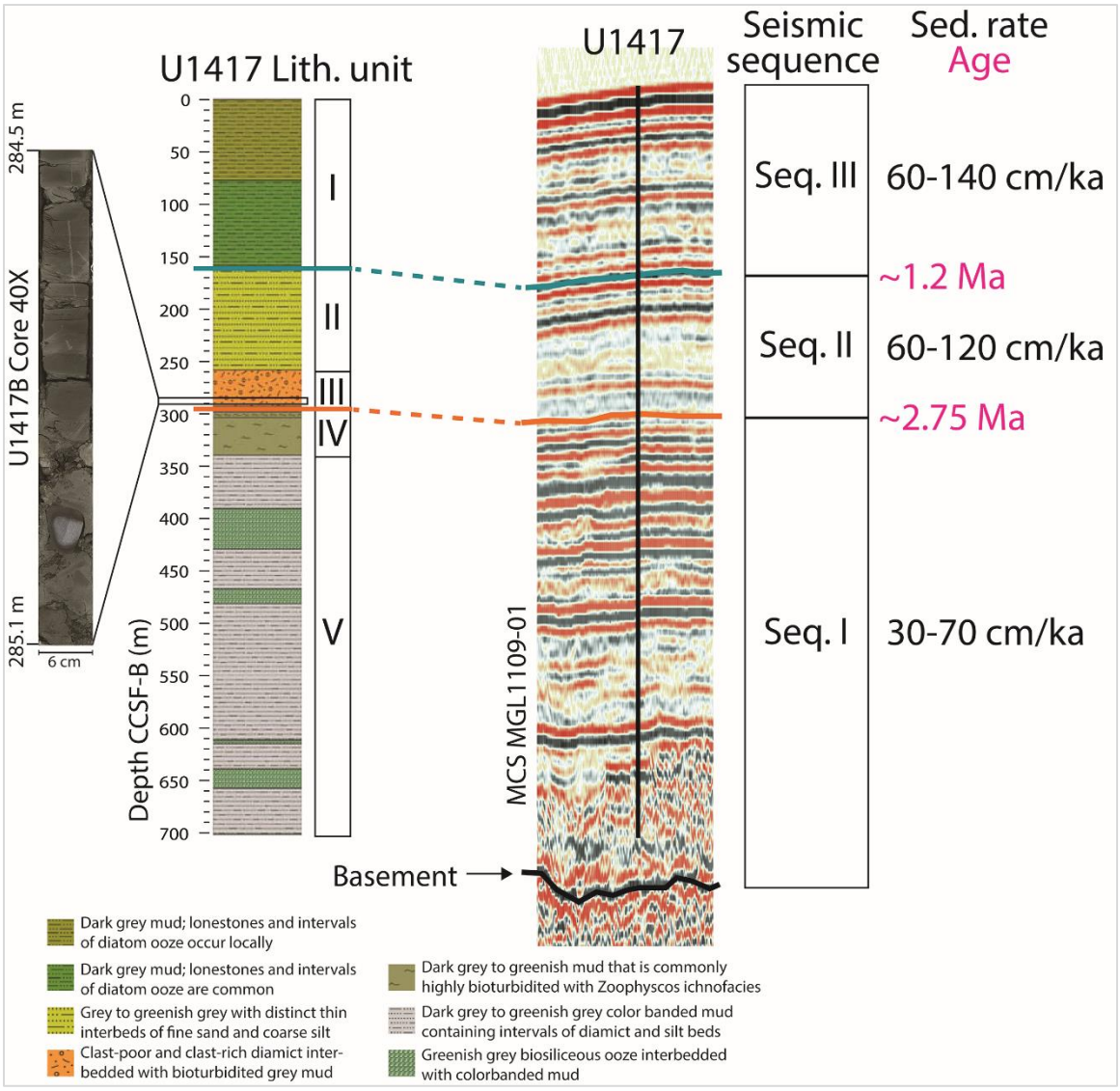

Figures 4.2: Lithology units and core image from site 1417 of IODP Expedition 341, subset of seismic MGL1109-01, seismic sequence nomenclature, sequence boundary ages, and sedimentation rates based on *Reece et al*. [2011], *Gulick et al*. [2015], and *Morey et al*., in prep. Black, orange, and green lines represent the top of oceanic crust, Sequence Boundary I-II, and Sequence Boundary II-III, respectively.

Research Vessel	Cruise designation	Dates of acquisition	System information
Marcus G. Langseth	MGL-1109	June 8-20, 2011	2D MCS, 640 channel, 8 km streamer at 12.5 m spacing, 36 airguns for total volume 6600 inch^3, shot interval 50 m and 4 ms sample rate.
Samuel Phillips Lee	L-7-77-WG	July 3-22, 1977	2D MCS, 24 channel, 2.4 km streamer, with receiver spacing 100 m, 5 airguns for total volume 1326 inch^3, shot interval 50 m and 4 ms sample rate.
	L-7-81-WG	June 11-30, 1981	
	L-8-81-WG	July 4-16, 1981	

Table 4.1: Expeditions acquiring MCS data used in this study.

4.3. Data and Methodology

In this study, we use MCS data acquired between 1975 and 1981 by USGS (Table 4.1) and newer MCS data acquired in support of the United Nations Convention on Law of the Sea in 2011. The six yellow lines on Figure 4.1 represent the MCS profiles.

We processed these MCS data in USGS Denver using the processing software Promax. Data processing included removing bad shot/channel, time variant scaling, automatic gain control, muting, normal move-out, common offset gather, and depth migrating using prestack Kirchhoff depth migration.

In Figure 4.1, we display 100 m resolution bathymetric data acquired by BGR using R/V *Sonne* in 1994 (greyscale) and global bathymetry-elevation data (background) [*Smith and Sandwell*, 1997; *Becker et al.*, 2009]. Multibeam system in R/V *Sonne* is the Atlas Hydrosweep equipped with 59 beams, beam width 2.3°, fan width of 90°, and operating at frequency 15.5 KHz. We received the bathymetric data already cleaned and gridded.

4.4. Observation

4.4.1. Basement and Frontal Wedge Relief

The surface of the Pacific Plate that converges with the North American Plate offshore Kodiak Island is not smooth; it consists of seamounts, guyots, and fracture zones (Figure 4.1). Moreover, Kodiak Seamount is now located in the Aleutian Trench and is in the process of being subducted. On all the seismic profiles, we interpret the top of the oceanic crust by the strong reflector beneath the thick Surveyor Fan, pre-fan sediment and the Aleutian Trench fill. Near the deformation front, from north to south, we interpret the depths of the oceanic crust to be 7,300 m, 9,000 m, 8,800 m, 9,700 m, 7,200 m, and 7,100 m, Figures 4.3 to 4.8, respectively. We observe that along the Aleutian Trench, the deepest basement is proximal to the mouth of the Surveyor Channel (Figure 4.1) consistent with findings of *Reece et al.* [2011]. The range of basement relief is from a relatively smooth (200-400 m, Figures 4.3 and 4.5) to that containing subducted seamounts (up to ~1,600 m in height) (Figure 4.4). Basement topography subducting under the North American Plate is highly variable.

Roughness of basement topography appears to correlate with the surface angle (α) of the prism toe. We measure the surface slopes of the six MCS profiles to within 10 km of the deformation front, the maximum slope of the frontal fold (either the landward or the seaward flank), and the approximate height of subducted seamount (Table 4.2). The profiles with smoother basement surface (Lines 70 and 120, Figures 4.3 and 4.5, respectively) have smaller surface angles within 10 km of the deformation front, while those with rougher surface exhibit larger angles at this distance. Line 705 (Figure 4.7) seems to contradict this observation, where the high basement relief (~1600 m) exhibit angle α of 4° within 10 km of the deformation front, but within 4 km, the angle steepens to

7°. We also observe that subduction of seamounts increases the surface slope of the frontal fold of the accretionary prism. This increase of surface slope correlates well with the height of the subducted seamount, i.e., seamount with height ~1,400 m (Line 15, Figure 4.4) versus that of ~500 m high (Line 703, Figure 4.8). The maximum slope of the frontal fold exhibits a positive correlation with the height of subducted seamount as well. The highest observed seamounts (Lines 15 and 705) are found under frontal folds with the largest slope gradients. An exception of this relationship is on Line 70 (Figure 4.3).

Surface angle (α)	Within 10 km (°)	Max. slope of frontal fold (°)	Seamount height (m)
Line 70 (Fig. 4.3)	4	16	~ 400
Line 15 (Fig. 4.4)	8	19	~ 1400
Line 120 (Fig. 4.5)	5	12	~ 600
Line 111 (Fig. 4.6)	5	6	~ 400
Line 705 (Fig. 4.7)	4	12	~ 1600
Line 703 (Fig. 4.8)	5	8	~ 500

Table 4.2: Surface angle of the frontal prism from the deformation front, maximum slope gradient, and seamount height measured along the six seismic profiles.

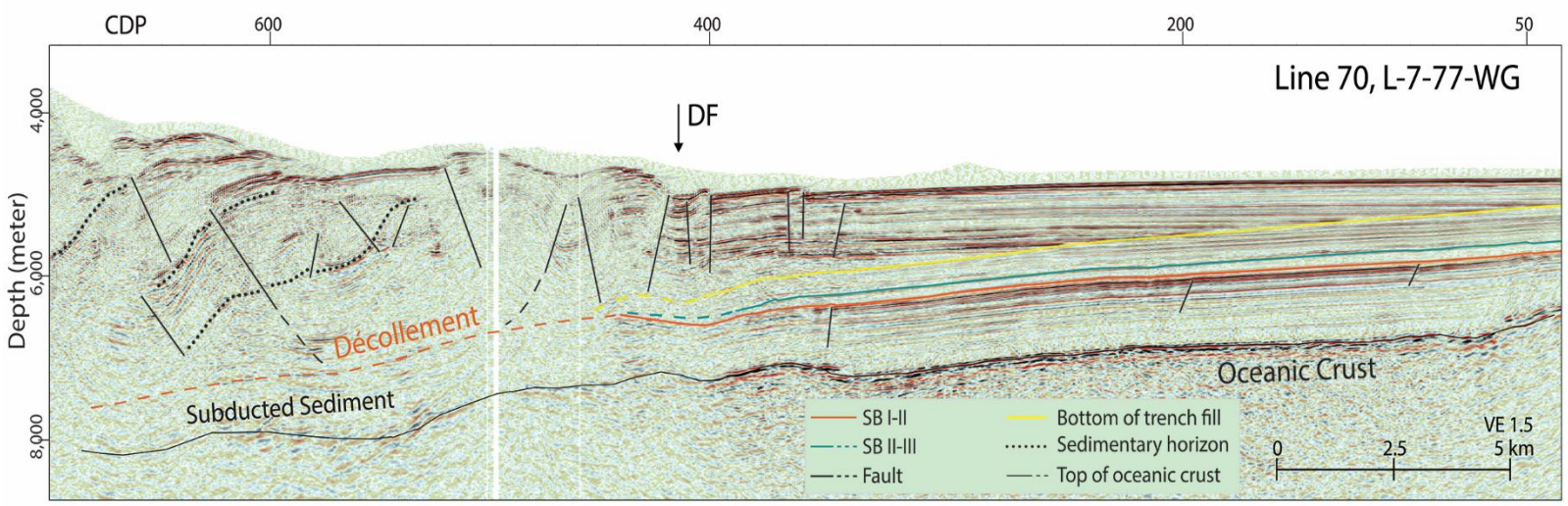

Figure 4.3: MCS profile of Line 70 of survey L-7-77-WG (refer to Figure 4.1 for location). Black lines are top of oceanic crust and interpreted faults, dashed orange line is interpreted décollement, orange line is Sequence Boundary I-II, green line is Sequence Boundary II-III, yellow line is bottom of trench-fill, and dotted lines are interpreted sedimentary boundaries. Dashed lines are those interpreted with less certainty. DF is the deformation front.

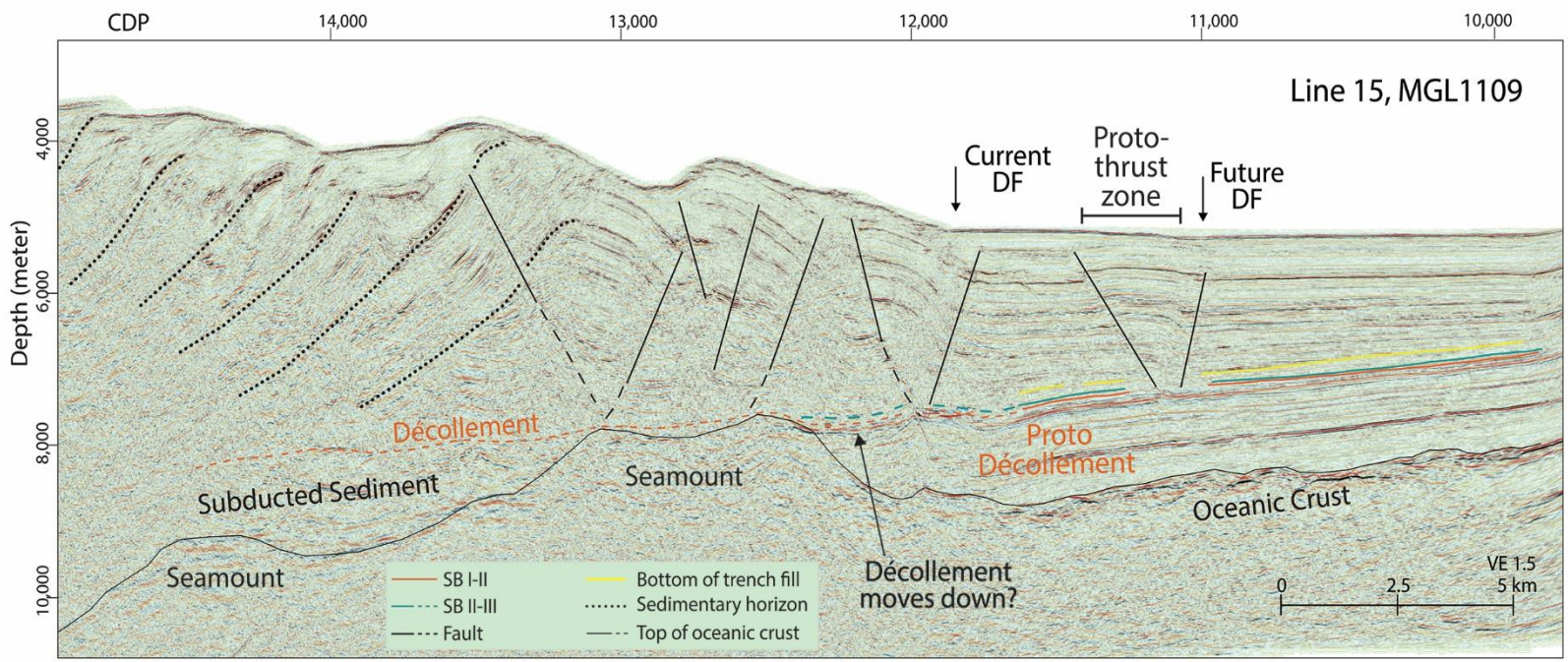

Figure 4.4: MCS profile of Line 15 of survey MGL1109 (refer to Figure 4.1 for location). Refer to Figure 4.3 for caption.

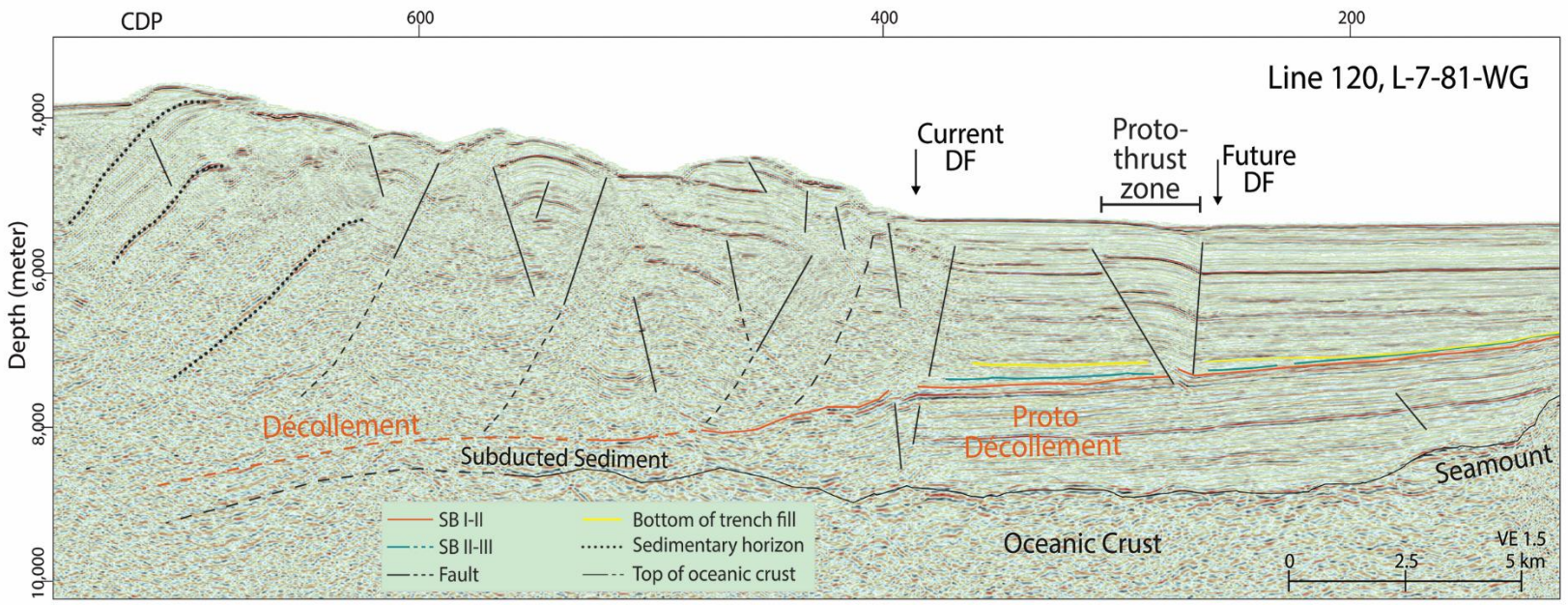

Figure 4.5: MCS profile of 120 of survey L-7-81-WG (refer to Figure 4.1 for location). Refer to Figure 4.3 for caption.

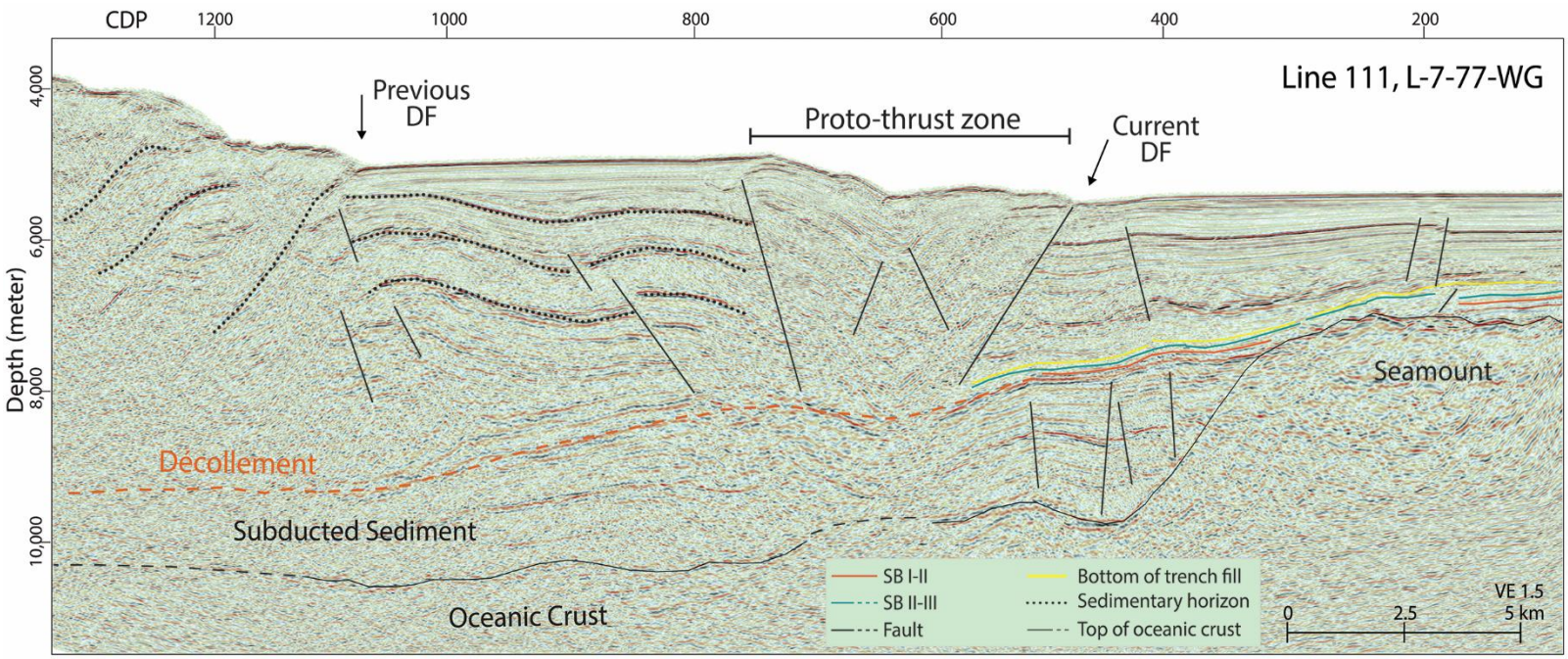

Figure 4.6: MCS profile of Line 111 of survey L-7-77-WG (refer to Figure 4.1 for location). Refer to Figure 4.3 for caption.

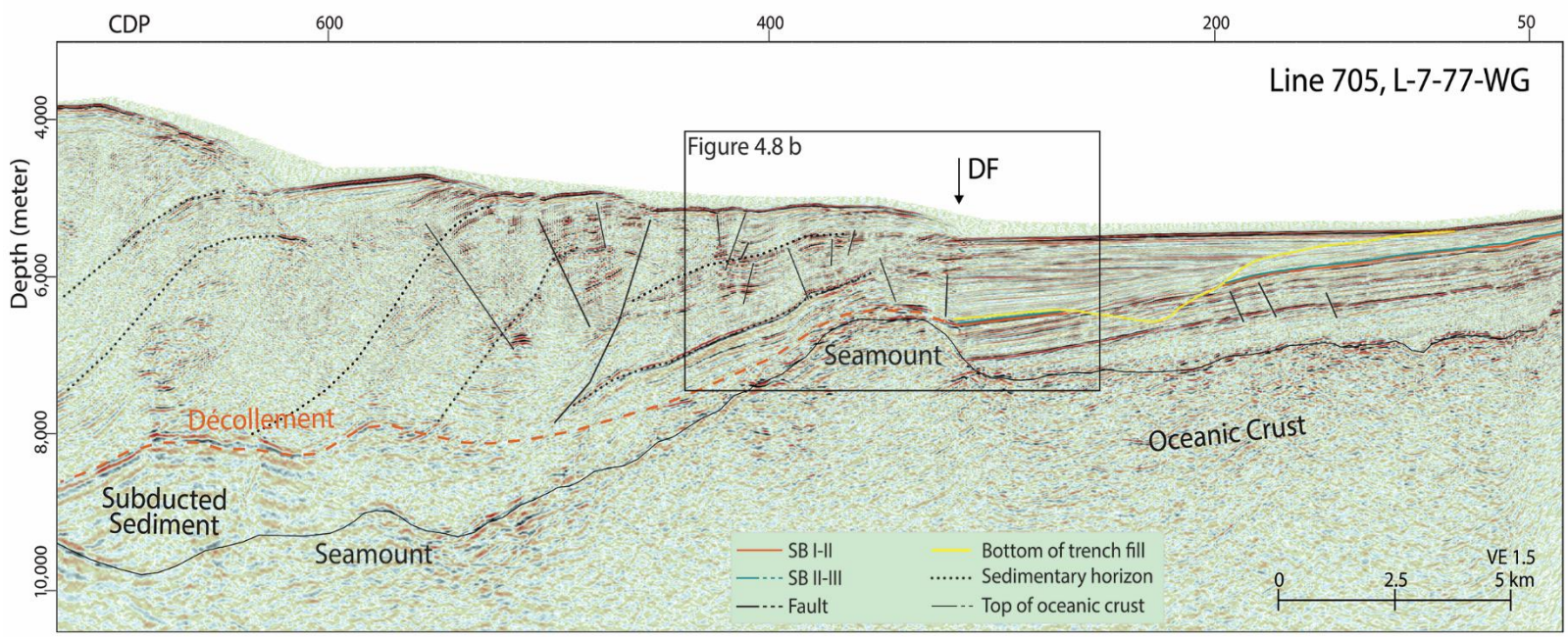

Figure 4.7: MCS profile of Line 705 of survey L-7-77-WG (refer to Figure 4.1 for location). Refer to Figure 4.3 for caption.

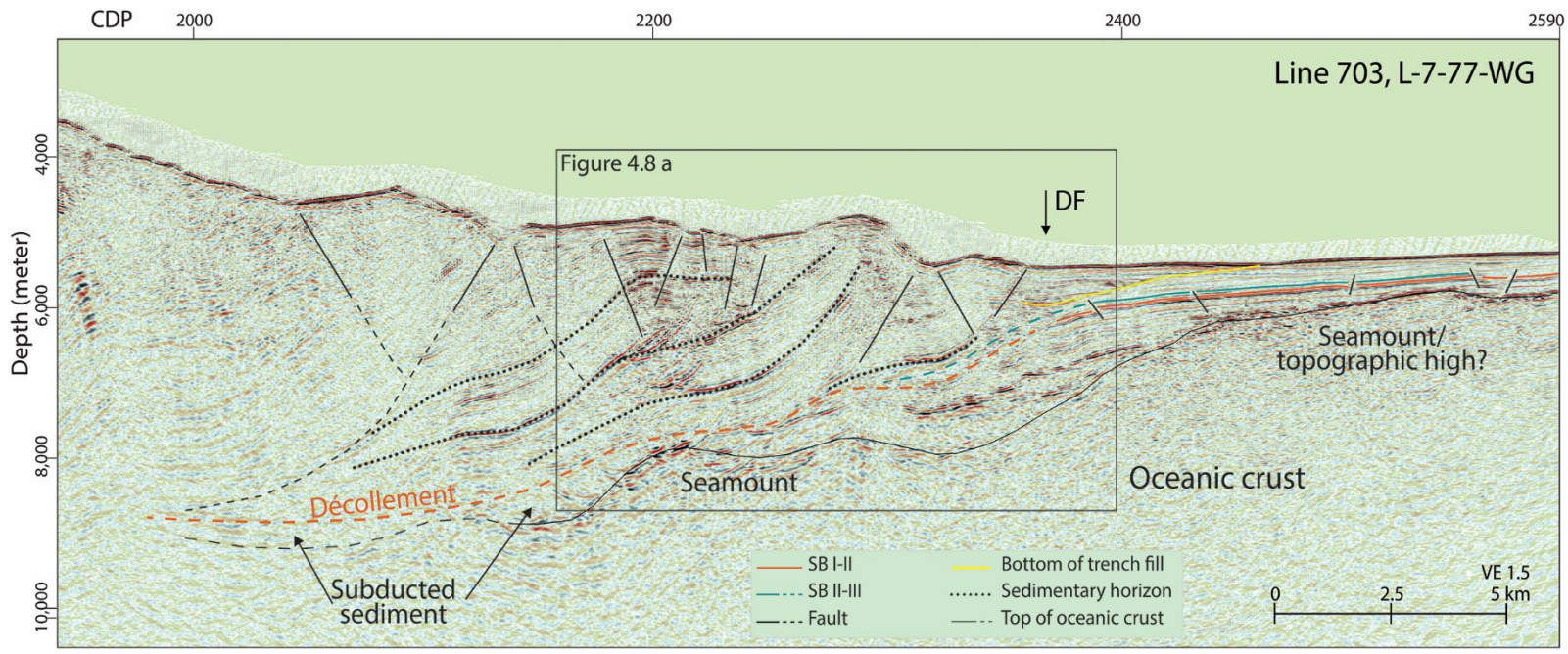

Figure 4.8: MCS profile of Line 703 of survey L-7-77-WG (refer to Figure 4.1 for location). Refer to Figure 4.3 for caption.

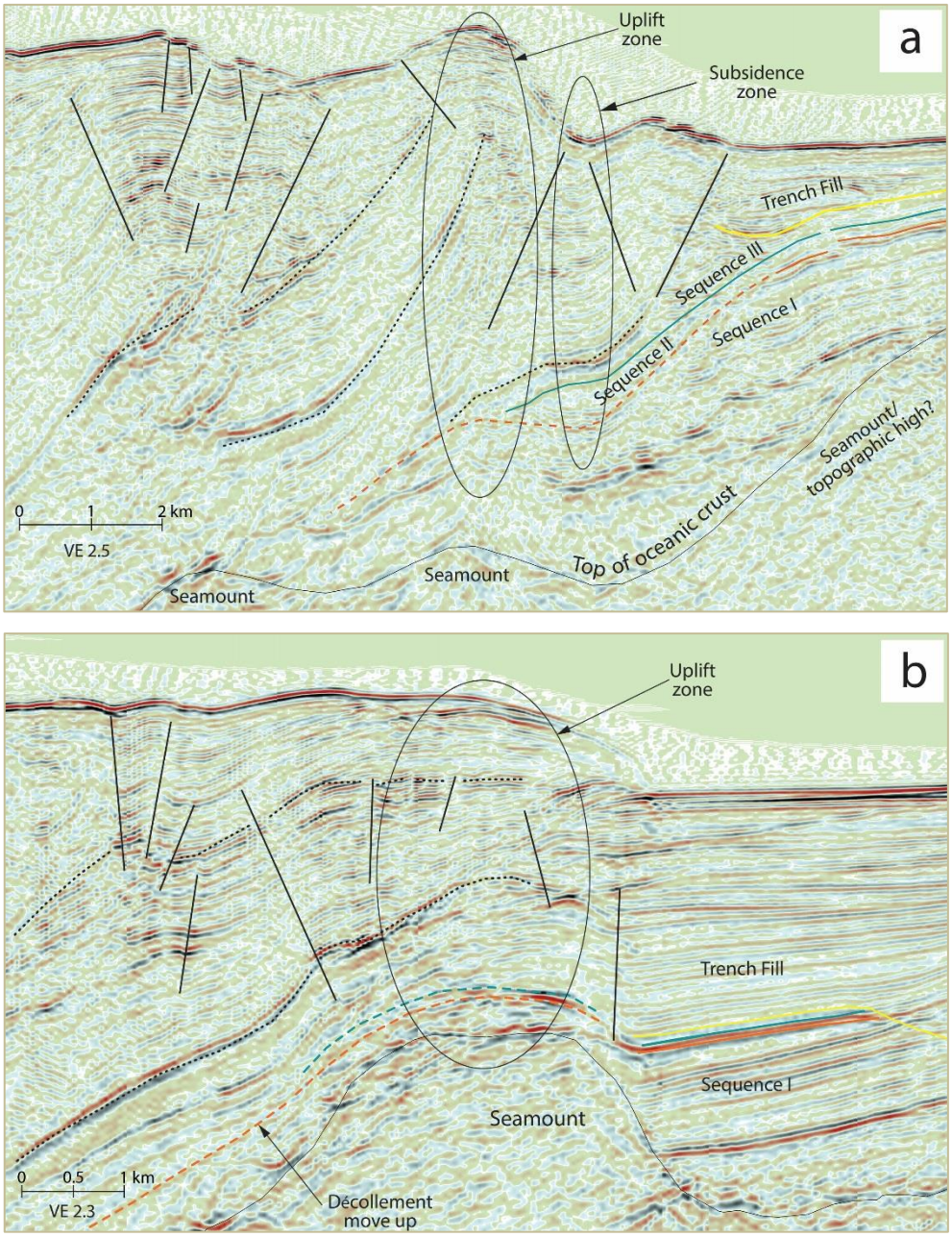

Figure 4.9: Seismic subsets of Lines 703 (a) and 705 (b) to illustrate zones of uplift and subsidence, and uplift of the décollement. Refer to Figures 4.7 and 4.8 for locations.

4.4.2. Sediment Thickness Variation

Sediment thickness within the Aleutian Trench also varies. Table 4.3 presents the thickness of Sequences I to III (refer to Figure 4.1 for locations) as well as the trench fill thickness. Note that our study differ from that of *Reece et al.* [2011] and *Gulick et al.* [2015] where we differentiate the trench fill from the sediment package of Sequence III. The major source of the trench fill is along strike largely from the Bering-Bagley system and the Prince William Sound; Source of Sequence III is from the Malaspina-Hubbard system [*Reece et al.*, 2011; *Gulick et al.*, 2015]. We observe that the thickest trench fill occurs directly in front of the mouth of the Surveyor Channel (Figure 4.1), as shown in Lines 15 (Figure 4.4), 120 (Figure 4.5), and 111 (Figure 4.6). Sequence I is a conformable sediment package above the oceanic basement deposited pre-Surveyor Fan; it contains continuous reflectors that represent alternating turbiditic and hemipelagic layers [*von Huene*, 1972; *Jaeger et al.*, 2014]. Our observations show that sediment thickness near the deformation front for sequences II and III are much thinner than sequence I (Table 4.3) possibly due to compaction under the trench fill. Furthermore, we observe that the trench fill probably cut down to sequence I as interpreted in Line 705 (yellow line, Figure 4.7). These observations show that sediment thicknesses along the Aleutian Trench correlate more with proximity to the mouth of the Surveyor Channel, i.e., delivery of Sequence II and III sediment.

	Trench Fill (meter)	Sequence I (meter)	Sequence II (meter)	Sequence III (meter)
Line 70 (Fig. 4.3)	1300	700	100	300
Line 15 (Fig. 4.4)	2000	1100	100	<100
Line 120 (Fig. 4.5)	1800	1600	<100	<100
Line 111 (Fig. 4.6)	2200	2000	<100	<100
Line 705 (Fig. 4.7)	1100	400	<100	<100
Line 703 (Fig. 4.8)	500	1100	200	200

Table 4.3: Sediment thickness near the deformation front along the Aleutian Trench.

4.4.3. Structural observation

Along our six seismic profiles, we interpret thrust faults and normal faults. The thrust faults are predominantly within the accretionary prism and the normal faults are located seaward of the deformation front. Most of the normal faults are interpreted within Sequence I, although in Lines 111 and 703 (Figures 4.6 and 4.8, respectively), these faults appear to crosscut Sequence Boundary I-II and II-III.

Within the accretionary prism, we observe that many of the thrust faults extend toward the décollement as well as crosscut distinct sedimentary packages. Furthermore, atop a subducting seamount, we observe that several thrust faults are responsible for the uplift of the frontal prism (Lines 15 and 705, Figure 4.4 and 4.7, respectively).

On all six seismic profiles, we interpret the deformation front to be located above the first major thrust that extends toward the décollement. On Lines 15 and 120 (Figures 4.4-4.5), seaward of the deformation front, we interpret a thrust fault and its conjugate down to what we call the proto-décollement and this pair of thrust faults form an area we call a proto-thrust zone. We also interpret a proto-thrust zone in Line 111 (Figure 4.6) located just landward of a large (~2,600 m high) deeply buried (>1,500 m from the seafloor)

subducting seamount. Lines 15, 120, and 111 (Figures 4.4-4.6) transect the Aleutian Trench and map the subsurface within a distance of ~40 km.

Within the accretionary prism, we observe a zone consisting of large-thrust-slices; they are tilted sedimentary packages. We interpret some of these thrust to extend down to the décollement. The thickness of this thrust slice appears to be similar except in Line 703 (Figure 4.8).

4.5. Discussion

4.5.1. Sediment Horizon and Detachment Zone

Depths of the décollement near the Aleutian Trench coincide with the depths of sequence boundary I-II as mapped from U1417 and throughout the Surveyor Fan [*Gulick et al.*, 2015]. On all of our seismic profiles, we interpret the décollement to be the extension of the sequence boundary I-II, i.e., the proto-décollement is likely this boundary and it represents a preferred detachment surface, at least for our six MCS profiles. We suggest that this depth of the detachment is probably due to being above the average maximum height of seamounts approaching the Aleutian Trench combined with a strength contrast in the sediments due to lithology of the Sequence I-II boundary. Drill Site U1417 (Figures 4.1 and 4.2) show gravel-sized ice-rafted debris present at the base of Sequence II overlying a muddier interval at the top of Sequence I at depth a little less than 300 m [*Jaeger et al.*, 2014; *Gulick et al.*, 2015]. Either the coarser interval with its increased porosity or the more clay rich interval just below it, or the contrast in physical properties between may be the cause of the preferential localization of the décollement at this boundary. Based on depths of our interpreted décollement, we propose that most if not all of sequence I is subducted under the accretionary prism with thicknesses dependent on the topography of the basement and proximity to subducted seamounts (Figures 4.3-4.8). The depths of our interpreted

décollement show significant thickness variation of sediment being subducted; we propose that some of the thickening is due to layer parallel compressional stress from seamount subduction.

Our interpreted depth of the décollement as the extension of the Sequence Boundary I-II is a new concept. Previously interpreted décollement position by *von Huene et al.* [1987] using a post-stack migrated version of Line 111 suggested that the seaward extend of the décollement coincides with the seaward verging thrust of the proto-thrust zone and surfaced at CDP ~490. A similar interpretation followed on seismic lines located ~50 km south and parallel to Line 70 (Figure 4.3) and ~130 km south and parallel to Line 703 (Figure 4.8), where the décollement was interpreted to extend and reach the seafloor at the deformation front [*Gutscher et al.*, 1998; *von Huene et al.*, 2012]. We suggest our improved imaging argues instead for a décollement that stays at depth and is correlative with the Sequence I-II boundary.

4.5.2. Sediment Thickness

Sediment thicknesses vary along strike. We observe Sequence I to be the thickest among the three sequences at the trench if the trench fill is viewed as discrete from Sequence III (Table 4.3). At drill site DSDP 178/U1417, some ~80 km away from the Aleutian Trench (Figure 4.1), *Reece et al.* [2011] and *Gulick et al.* [2015] also observed that Sequence I is much thicker than Sequences II and III. The maximum thickness of sequence I is on Line 111 (Figure 4.6) and the minimum is on Line 705 (Figure 4.7) at ~140 km south of Line 111. However, sequence I is thickening again in Line 703, our most distance seismic profile from the Surveyor Channel (Figure 4.1). This apparent thickening may represent the additional sediment from inland through the Shelikof Strait and Tugidak Basin [*von Huene et al.*, 1987]. In contrast to sequence I, sequences II and III do not vary

as much along the Aleutian Trench (Table 4.3). However, temporarily, the trench fill is coeval with Sequence III and varies in thickness along strike significantly. The orogenic sediment flux proximal to the Aleutian Trench discussed in *Gulick et al.* [2015] is therefore to a large part within the trench fill.

Figure 4.2 shows the sedimentation rate for each of the sequences and the core description column shows the thickness of each sequence at site 1417. The seaward edge of Line 70 (Figures 4.1 and 4.3) starts at ~70 km landward of drill site 1417; the thickness of Sequences II and III observed between drill site 1417 and those near the Aleutian Trench on Line 70 (Table 4.3) appear to be comparable, suggesting minimal compaction occur within the ~70 km distance.

4.5.3. Subduction Process of Buried Seamounts

Offshore Kodiak Island, seamounts atop the Pacific Plate are being subducted under the North America Plate at a rate of ~5-7 cm/y [*von Huene et al.*, 1987]. The six MCS profiles give us the opportunity to observe stages of subduction as the profiles capture seamounts situated at several locations with respect to the deformation front. Table 4.2 and Figures 4.3-4.8 show that the increase of surface slope of the frontal prism correlates with higher basement relief [*von Huene et al.*, 2012], i.e., Line 15 (Figure 4.4) versus Line 70 (Figure 4.3). These uplift effects of the frontal folds have been observed in other convergent margins such as the Hikurangi [*Barnes et al.*, 2010; *Pedley et al.*, 2010], Nankai [*Park et al.*, 1999; *Bangs et al.*, 2006], Chile [*Laursen et al.*, 2002], and Costa Rica [*Von Huene et al.*, 2000]. Sandbox models have also successfully produce the same observation [*Lallemand et al.*, 1992; *Lallemand et al.*, 1994; *Dominguez et al.*, 2000].

Based on our six MCS profiles and results of sand box model for subduction of partially buried seamount [*Dominguez et al.*, 2000], we propose a model for the sequences

of subduction for deeply buried seamount offshore of Kodiak Island (Figures 4.10a – 4.10c). The seamount at position 1 (Figure 4.10a) represents the seamount situated seaward of the deformation front, where we propose layer-parallel compressional stress from the incoming seamount activate thrust faults to develop a proto-thrust zone, the pair of thrust faults adjacent to the seamount at position 1. Position 2 in Figure 4.10b represents a seamount situated beneath the deformation front. Uplift of the frontal prism is observed above the seamount as the result of thrust faults reactivation. At this position 2, we propose that the proto-thrust zone become the new position for the deformation front, seaward of the previous location, signifying a seaward jump of the deformation front. Position 3 (Figure 4.10c) represents a seamount at a later stage of subduction. Again, we observe uplift of the wedge above the seamount and slump or subsidence on the trailing flank.

From our six seismic profiles, a specific example for the seamount at position 1 is illustrated in Figure 4.6 (Line 111). We observe a proto-thrust zone at ~9 km seaward of the location that we interpret as the previous deformation front. We propose layer-parallel compressional stress from convergence of the large (~2,600 m tall) deeply buried (>1,500 m sedimentary overburden) seamount produces the observed proto-thrust zone.

Similar proto-thrust zone is observed in the Hikurangi Margin [*Barnes et al.*, 2010] even though the seamount is only partially buried. Figure 4.8 (Line 703) may also represent a seamount at position 1, but we argue that the gradual change of basement relief and/or the minimum height of the seamount may explain the lack of proto-thrust zone. While no sandbox experiments use deeply buried seamounts, we propose that the larger degree of deformation we observe in Line 111 (Figure 4.6) is the result of the tall seamount buried under much thicker sediment. On adjacent seismic profiles (Lines 15 and 120, Figures 4.3 and 4.4, respectively), we also observe similar proto-thrust zone but at smaller magnitudes. While we cannot ascertain whether the same large seamount produced the proto-thrust zone

observed in Lines 111, 15, and 120, we propose that the formation of this zone is in response to the converging seamount; and the size and burial depth of the seamount are responsible to the magnitude of the deformation. Moreover, as the seamount continues toward the frontal prism, the seaward edge of the proto-thrust zone will become the new position of deformation front; an occurrence of a deformation front jump (Figure 4.10b).

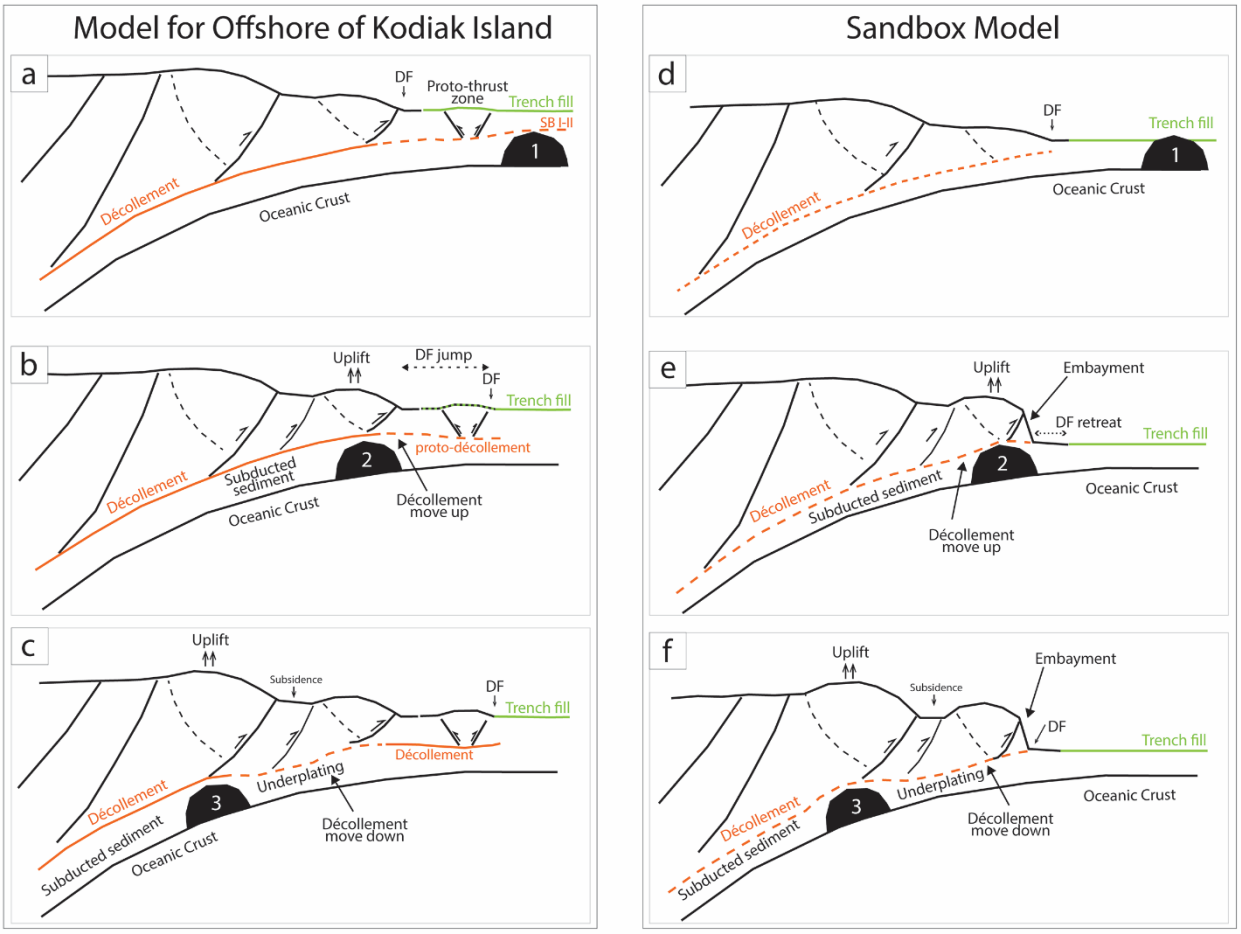

Figure 4.10: Proposed model for the subduction process of a buried seamount offshore of Kodiak Island based on the six seismic data. Left panel (a, b, c) represent progressive locations of a deeply buried seamount. Right panel (d, e, f) illustrate the results of sandbox experiment for partially buried seamount ([*Dominguez et al.*, 2000]). Black lines represent thrust faults, orange line is décollement, and green line is seafloor. DF is deformation front and dashed arrows represent shift of the deformation front's position.

Figures 4.4 and 4.7 represent examples for a seamount at position 2 (Figure 4.10c). At this stage of subduction, deformation of the frontal wedge show surface slope gradient increase to 8° and 4° (Table 4.2), respectively. Note that the increase in basement relief corresponds well with surface slope. This type of deformation is also observed in other margins and has been successfully reproduced in sandbox models. Examples for a seamount at position 3 (Figure 4.10c), and at later stages of subduction, are Figures 4.4, 4.5, 4.7, and 4.8 with various seamount sizes. Again, we observe uplift of the wedge above the seamount and slump or subsidence on the trailing flank. We show in Figure 4.9, a closer look at the zones of uplift and subsidence for Lines 703 and 705.

Underplating, a deepening of the décollement, is observed in other margin such as Nankai [*Bangs et al.*, 2006]. It occurs on the trailing side of the subducted seamount. In our model, we represent this using dashed orange line in Figure 4.10c, behind the seamount at position 3. While we do not observe clear reflectors that illustrate underplated sediments and thus a décollement step down, we acknowledge the possibility of underplating of the former décollement and subducting sediments in the wake of seamount subduction. On our seismic profiles, underplating probably occurs between CDPs 12,000 and 12,500 (Line 15, Figure 4.4).

For the seamount we observed in Line 15 (Figure 4.4), we attempted to infer the seamount's shape using the magnetic anomaly data acquired also during the MGL1109 expedition. We found no correlation with the magnetic anomaly. This observation of magnetic anomaly attenuation is also reported by [*von Huene*, 1972; *von Huene*, 1979] for the slope region around the Kodiak Seamount.

Figures 4.10d – 4.10f exhibit the results of sand box model, modified from *Lallemand et al.* [1992] and *Dominguez et al.* [2000]; we want to compare this model to that of our model offshore of Kodiak Island (Figures 4.10a – 4.10c). The sandbox model

employ partially buried seamount (Figure 4.10d), where the trench fill (green line) is only partially cover the seamount. Upon subduction, uplift of the prism toe above the seamount and subsidence or embayment is observed trailing the seamount (Figure 4.10b). Note that the deformation front has retreated landward from the previous position (Figure 4.10d). Upon further subduction, underplating is observed on the trailing side of the seamount (Figure 4.10f). We want to remark that this sandbox model do not exhibit deformation jump as shown by our model. Furthermore, based on our interpretation of the six seismic profiles, deeply buried seamount may cause a seaward displacement of the deformation front as oppose to the landward retreat of the deformation front that result from the slumping or embayment on the deformation front. This difference may be a fundamental aspect of deeply buried seamounts in cases when the height of the seamount is close to the height of the décollement above the oceanic crust.

With the various seamounts found in convergent margins, there exist numerous publications on seamount subduction; however, publications on deeply buried seamounts are limited. Seamounts located within large submarine fans will be a good start for investigation of deeply buried seamount subduction and test our proposed model. Other than the Surveyor Fan, two large submarine fans near subduction zones are the Bengal and Indus Fans. The eastern part of the Bengal Fan covers the Indo-Pacific Plate that contains seamounts, ridges, and fracture zones. This region will be a good area for investigation of buried seamount subduction and a test for the stages of buried seamount subduction proposed here.

4.6. Conclusions

Six seismic profiles offshore of Kodiak Island allow us to investigate sediment thicknesses along the Aleutian Trench, development and depths of décollement, and

different stages of seamount subduction. The imaged seamounts are deeply buried under the thick Surveyor Fan and the Aleutian Trench fill, which is a rare condition relative to most seamounts on other convergent margins. First, we observe a distinct stratigraphic level on all the seismic data that later becomes the décollement. The lithology of this sedimentary horizon is probably the cause of the preferred zone; gravel-sized ice-rafted sediment representing the onset of intensification of Northern Hemisphere glaciation overlying a muddier interval but also coincides with the average height of the buried seamounts. Second, we observe that the surface slope of the frontal prism along this margin correlates with the height of the subducted seamount on our seismic profiles. Third, large-buried seamounts cause a significant seaward jump of the deformation front through formation of proto-thrust zones and lack of a landward retreat of the deformation front as has been observed for emergent seamounts; we propose such a proto-thrust zone and subsequent seaward step of the deformation front occurs due to increased local convergent stresses in advance of seamount subduction. Further studies are needed to better understand the subduction process of deeply buried seamount, its effect to the accretionary prism, its role on the décollement, and amount of subducted sediment. We propose seamounts or ridges within the Bengal Fan may be good candidates.

Chapter 5: Summary and Future Work

This dissertation presented studies of offshore northern Sumatra, Indonesia and offshore Kodiak Island, Alaska. Both are situated in a convergent margin setting with similar convergence rates. Offshore northern Sumatra, the Indo-Australia Plate collides at an oblique angle with the Sunda Block at 5-6 cm/y; offshore Kodiak, the Pacific Plate converges at right angle with the North America Plate at 6-7 cm/y [*von Huene et al.*, 2012]. The accretionary prisms of both these region are formed from the thick sediment scraped from the subducting oceanic plate. However, the age and properties of the incoming sediment are different. The incoming sediment offshore Kodiak is mainly younger than 5 Ma [*Jaeger et al.*, 2014; *Gulick et al.*, 2015]; those accreted offshore Sumatra is much older, 33-56 Ma, and of silt and sand-rich turbidite sediment [*Gulick et al.*, 2011]. Furthermore, the distance traveled by the sediments to northern Sumatra is about four times longer than to offshore Kodiak. The sediment source for offshore northern Sumatra is the Bengal Fan the result of Mount Himalaya orogeny; the sediment source for offshore Kodiak is the Surveyor Fan the result of Mount St. Elias orogeny. The topography of the oceanic plate also differs; The Pacific Plate is covered with fracture zones and major seamount chains. While the Indo-Australian Plate contains fracture zones, it does not contain seamount chains.

The overall goal for this research is to gain insight into geological factors that influence major seismic events and the development of convergent margins by studying deformation within and near the toe of accretionary prisms relative to the properties (thickness, induration) of the incoming sediments and/or presence of buried seamounts.

Chapter 2 focused on investigating the accretionary prism offshore of northern Sumatra using MCS and merged bathymetric data acquired after the 2004 Sumatra-

Andaman earthquake. I observed the existence of piggyback basins at various distances from the deformation front that suggests continuing shortening of the whole prism. I also observed consistent trend of fold vergence across the accretionary prism where closer to the deformation front is predominantly landward vergent, closer to the forearc Aceh Basin is predominantly seaward vergent, and in between is mixed vergence. These findings together with results of sandbox experiments lead me to propose the existence of a rigid backstop beneath the inner wedge. The top of this backstop coincides with a strong reflector under the Aceh Basin, then dipping down toward the décollement; the seaward tip of the backstop is located under the mixed vergence zone. I propose that this seaward dipping slope of the backstop assists in the formation of the observed extended landward vergence zone. During a major earthquake such as the 2004 event, the rigid backstop together with the dynamic backstop in the outer wedge [*McNeill and Henstock*, 2014], and the highly consolidated sediment on the outer prism [*Gulick et al.*, 2011], all move seaward co-seismically as if a solid block. The rupture energy can propagate beneath and with the block and consequently travel farther toward the Sunda Trench than a less consolidated accretionary prism would allow.

Chapter 3 focused on investigating seafloor deformation at the prism toe caused by the 2004 and/or 2005 seismic events using time series bathymetric data to substantiate the published proposals where seismic rupture reached closer to the Sunda Trench. This is the first study of using pre- and post-great earthquakes bathymetric data to investigate seafloor changes offshore of northern Sumatra. I observed gravitationally driven mass wasting that occurs on the seaward flank of one frontal fold and on the landward flank of another frontal fold. I also observed evidence of erosion around the edge of a large gully situated on a frontal fold. Interpreted thrust faults flanking these frontal folds appear to slip between Dec 24, 2004 and February 2005 and may be responsible for the observed mass wasting and

seafloor shoaling. Insignificant deformations in relation to the 2005 earthquake lead me to conclude that the seafloor deformation patterns are mainly related to the 2004 seismic event and that this southern portion of the 2004 rupture zone experienced little or no effect from the 2005 event.

Chapter 4 presented an investigation of sediment thickness and deeply buried seamounts along the Aleutian Trench. Using six seismic profiles, I find variations on the thickness of sediment package that correlate well with proximity to the Surveyor Channel where it terminates in the trench. The seismic profiles captured seamounts at different distances from the deformation front. As deeply buried seamounts or ridges are not common worldwide, possibly only existing under large submarine fans, these seismic profiles offer a unique opportunity to expand our knowledge on buried seamount subduction processes. I observe a distinct stratigraphic level that becomes the décollement, probably related to the lithology of the boundary and average height of subducting seamounts. The gravel-size lithology of this horizon represents the onset of intensification of Northern Hemisphere glaciation. The sediment package below this horizon, which is the Pre-Surveyor Fan sediment, is later subducted under the accretionary prism, hence smoothing the roughness of the top of subducting plate caused by the numerous seamounts in the Gulf of Alaska. I also observed positive correlation between seamount relief and the surface angles of the frontal prism overlying a subducting seamount. I propose that compressional stress from the incoming large-buried seamount cause the formation of a proto-thrust zone seaward of the current deformation front, which later promotes a significant seaward jump of the deformation front after the seamount is subducted. Further studies are needed to better understand the subduction process of deeply buried seamounts and their effects on the accretionary prism.

The study of northern Sumatra and Kodiak represent only a portion of the world's convergent margins where the majority of significant earthquakes occur. My study may give insights to other convergent margins with similar characteristics (such as thick incoming sediment, wide accretionary prism, or variation on topography of oceanic plate), for example the Cascadia and Makran. Our study on Kodiak shows that the thick pre-Surveyor Fan (Sequence I) and the Surveyor Fan sediment (Sequences II and III) cover most of the incoming seamounts. Furthermore, I propose that most if not all of Sequence I is subducted, essentially creating a much smoother subducting surface. I also observe smooth plate interface on our northern Sumatra study area. Studies on regions with large earthquake occurrence show the relationship of smooth subducting plate with large rupture zone [*Ruff*, 1989; *Heuret et al.*, 2012]; an update to the relationship for limits on earthquake magnitude based on age and convergence rate alone [*Ruff and Kanamori*, 1980]. Regarding the relationship of seamount subduction with earthquake occurrence, *Wang and Bilek* [2011] proposed that seamount subduction rarely produce large earthquake, instead seamount subduction is predominantly aseismic creeping. In addition, *Wang and Bilek* [2014] suggested that high topography variation is shown to hinder large rupture propagation. Both of my study areas, Kodiak and northern Sumatra experienced recent large earthquakes, which support the hypothesis that occurrence of large seismic event tend to correlate with a smooth subducting plate. Further investigation to the physical properties of the incoming sediment may yield additional insight on the controls of megathrust earthquake occurrence.

This research also emphasizes the importance of time series geophysical data and continuous geodetic monitoring for efforts on hazard preparedness and the improvement of our understanding of great earthquake processes and effects. In terms of societal consequences of a seismic event, we propose that in addition to focus on regions within a

seismic gap, we need to consider proximity to densely populated areas and/or major cities as important. Integration of various observation methods such as geodetic, geology, and geophysics instruments are essential in better understanding these hazard prone areas. For that purpose, collaboration of multidiscipline geo-scientists, likely multinational is the most effective way.

Study of the sediment properties covering the Indo-Pacific Plate is important in understanding the significance of the incoming sediment in the development of the accretionary prism and its associated seismogenic and tsunamigenic hazard. In August-October 2016, IODP will conduct expedition number 362 “The Sumatra subduction zone: the role of input materials in shallow seismogenic slip and forearc plateau development”. They will drill the distal incoming sediment down to the basement in hope to understand the sediment evolution prior to being accreted. Representing Indonesia, I will serve as a member of the science party to study the physical properties of the sediment from core samples and log information, and correlate them to seismic data.

Appendix

Appendix A: Supplementary material for Chapter 2

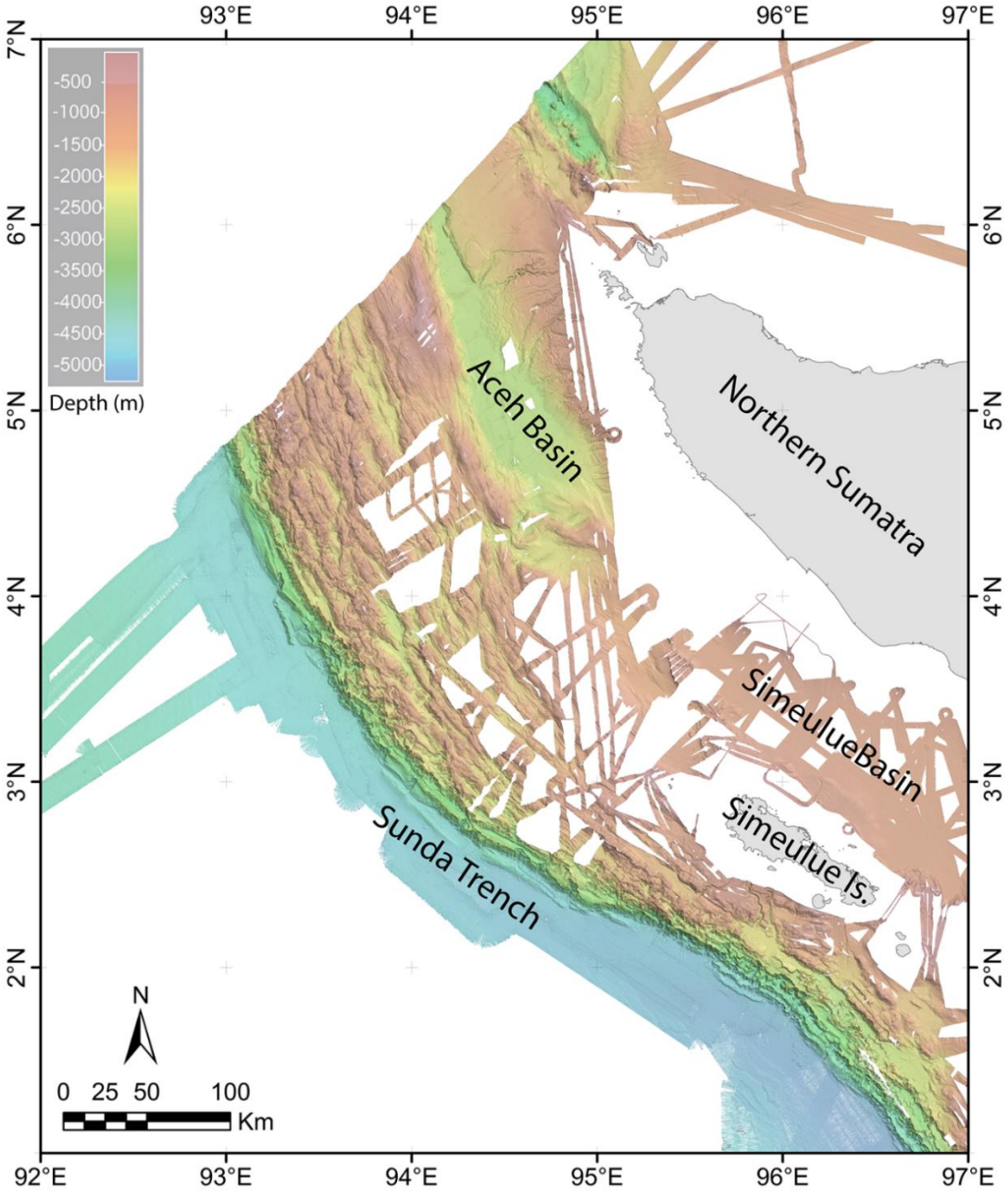

Figure A.1: Bathymetric coverage, compilation of surveys listed in Table 2.1

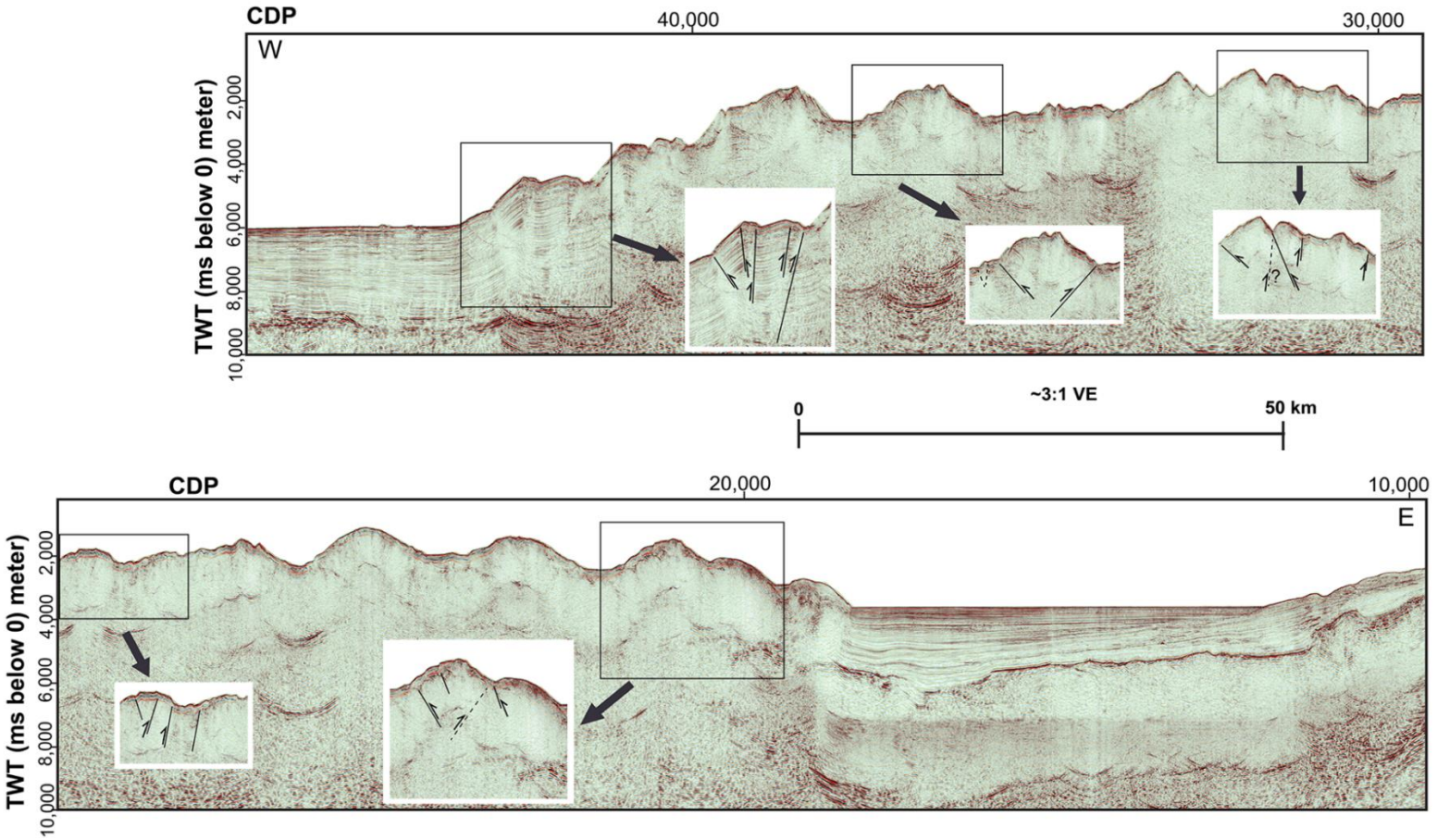

Figure A.2: Supplementary material 1, seismic line BGR06-107

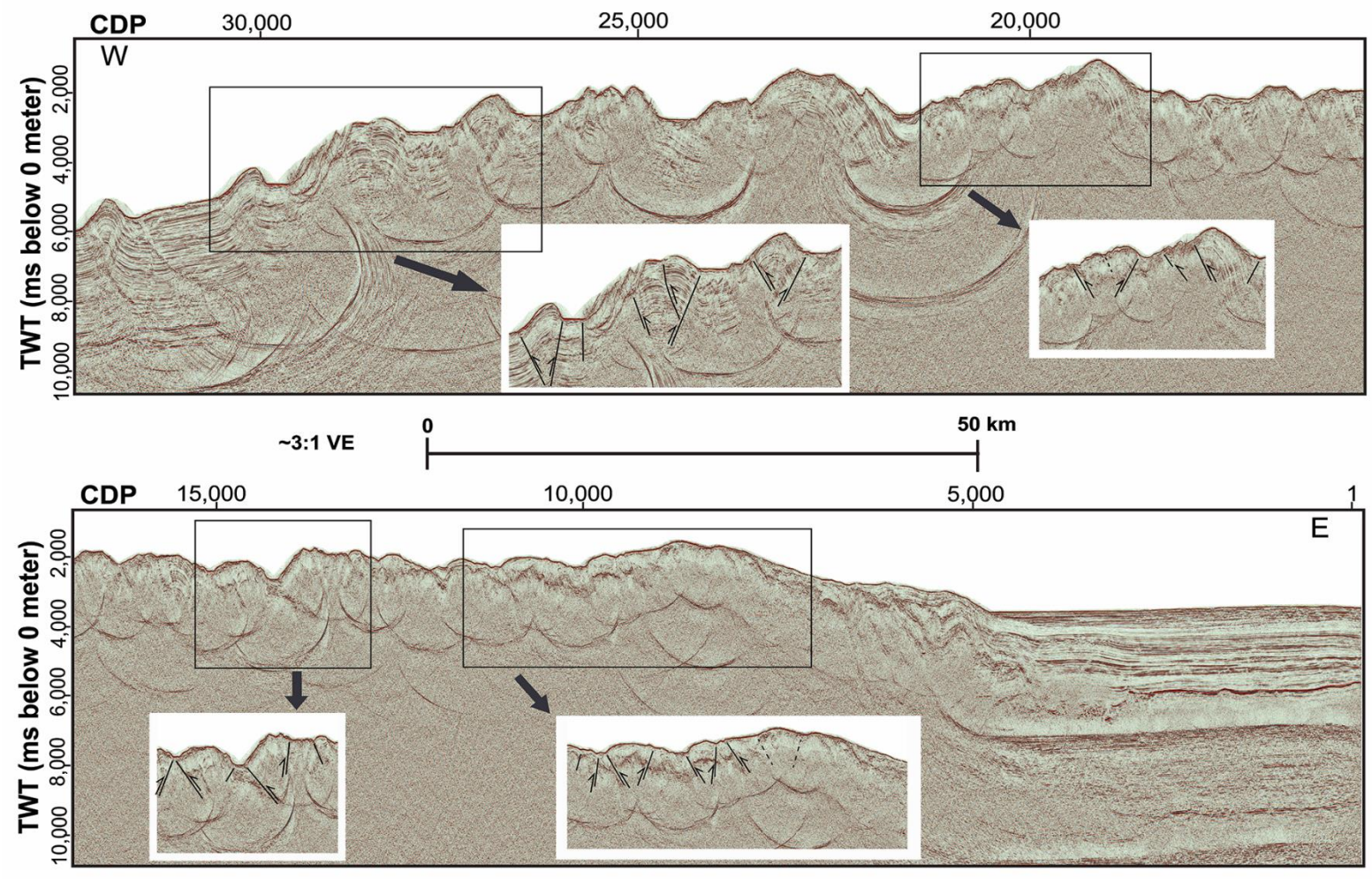

Figure A.3: Supplementary 2, seismic line SUMUT-07

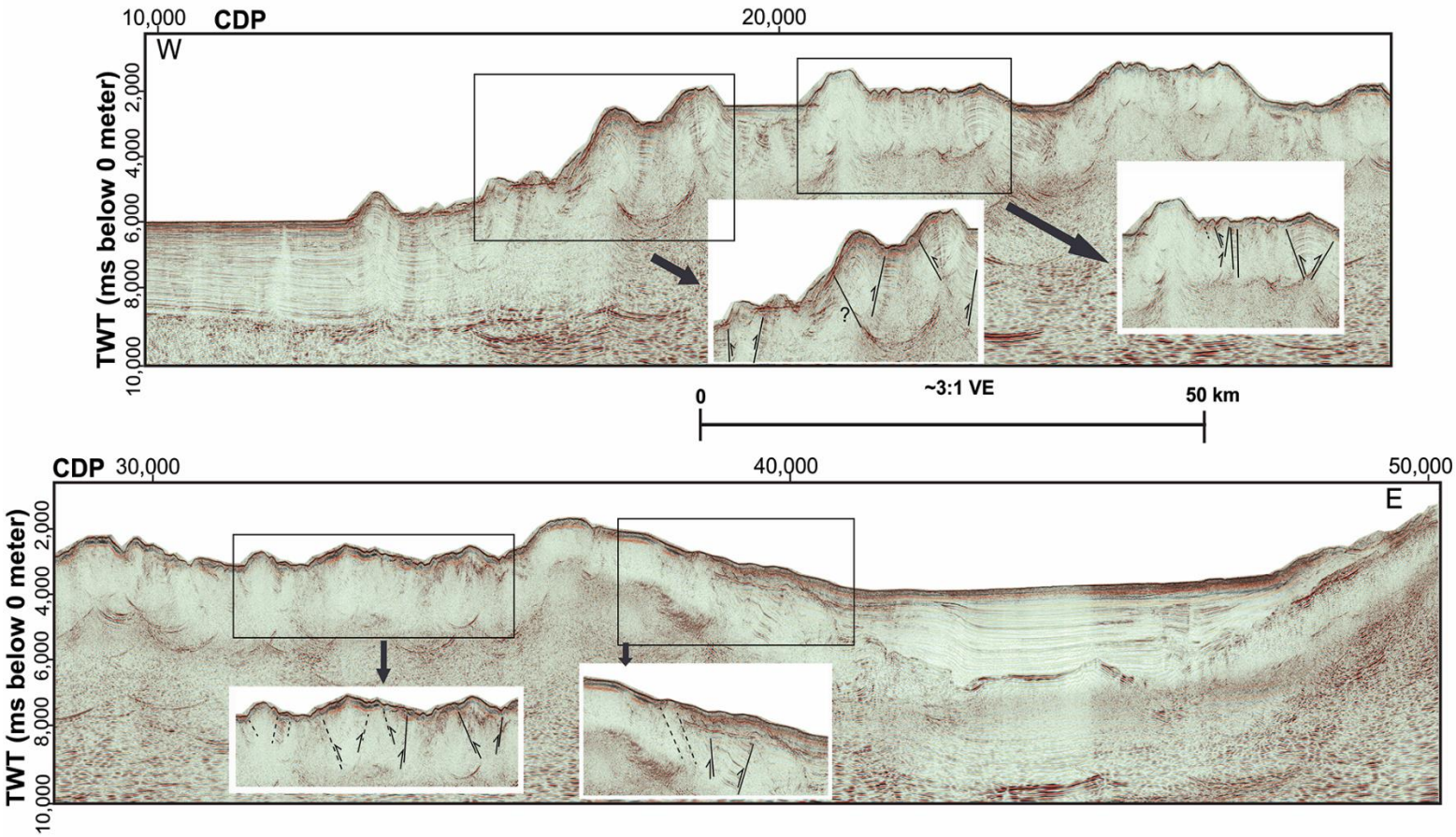

Figure A.4: Supplementary material 3, seismic line BGR06-105

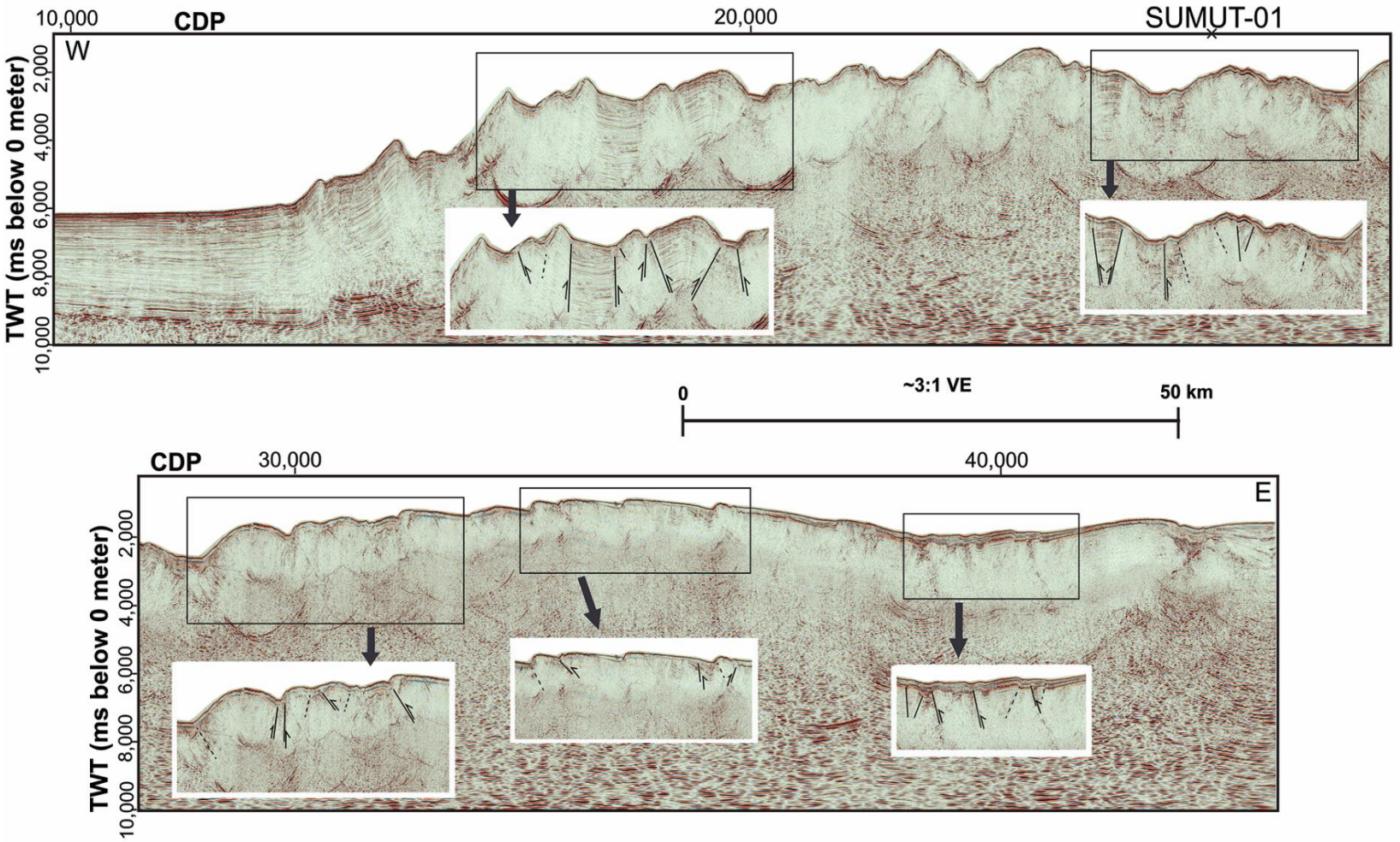

Figure A.5: Supplementary material 4, seismic line BGR06-112

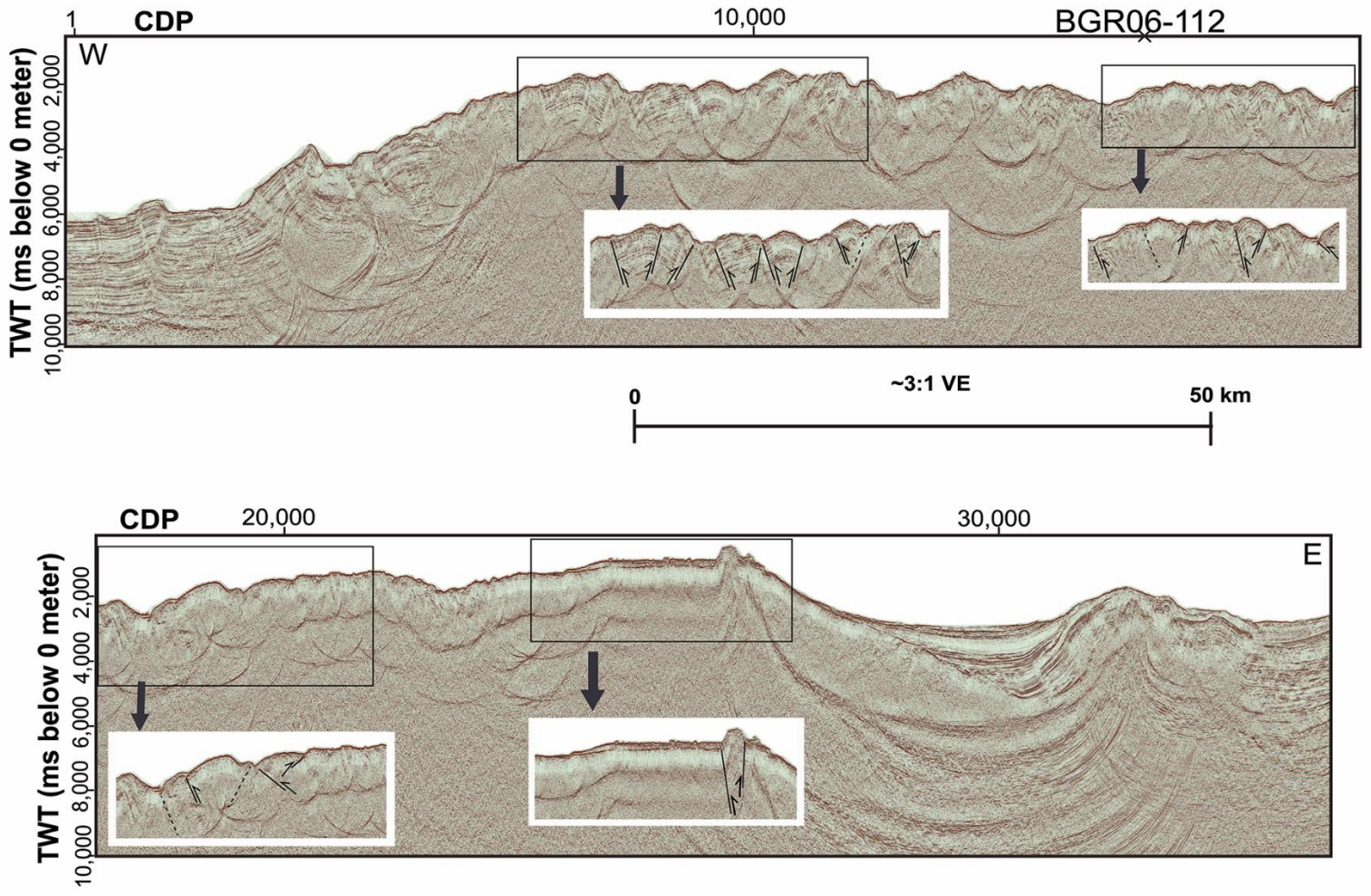

Figure A.6: Supplementary material 5, seismic line SUMUT-01

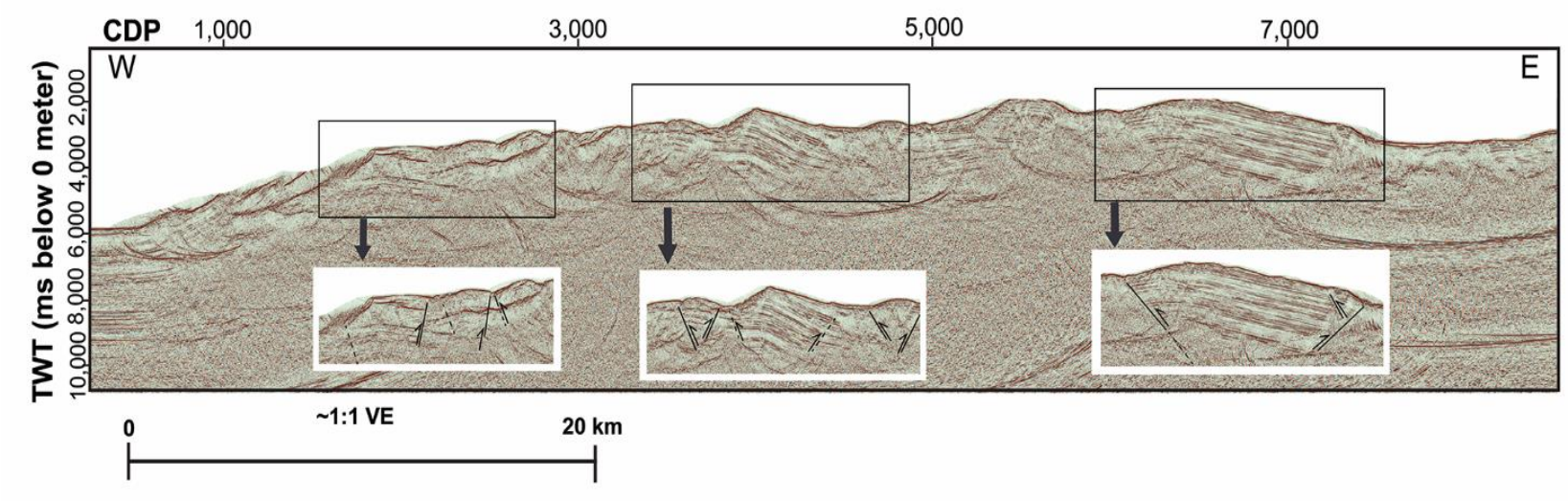

Figure A.7: Supplementary material 6, seismic line SUMUT-15

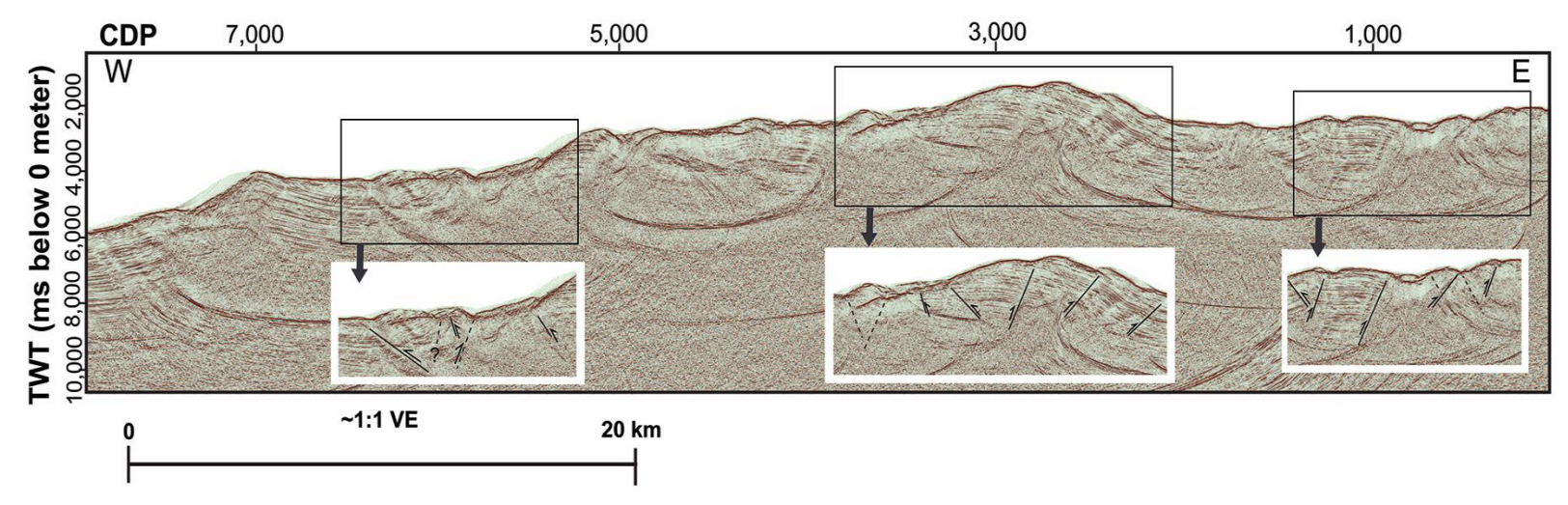

Figure A.8: Supplementary material 7, seismic line SUMUT-17

Appendix B: Supplementary materials for Chapter 3

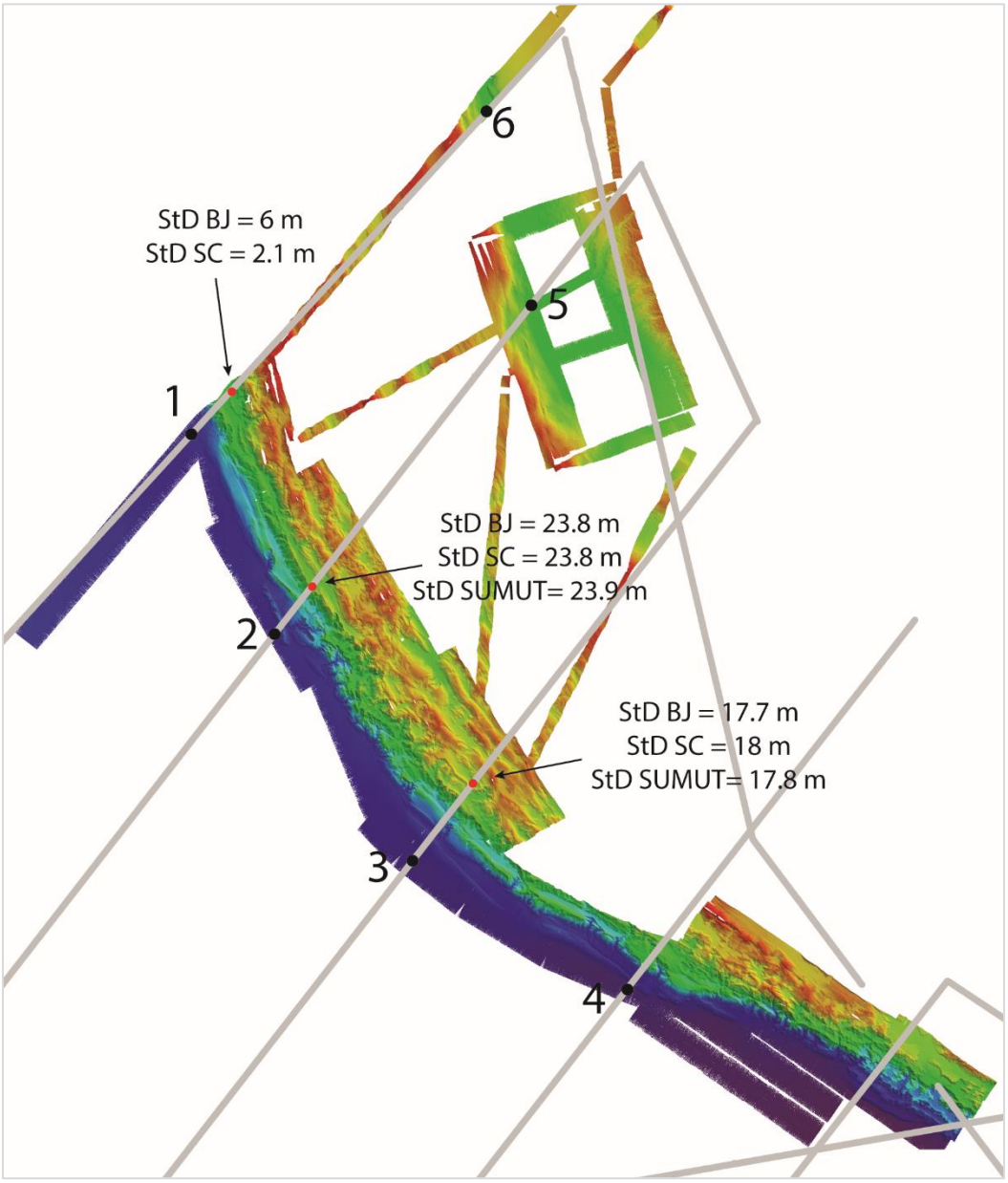

Figure B.1: Locations for determining vertical static shift between SC (2005) and BJ (1998) data. We chose the overlapped track lines (black dots) for measuring the depth difference. Average depth difference for these 6 locations is 0.9976 m. Red dots are locations for depth accuracy measurement.

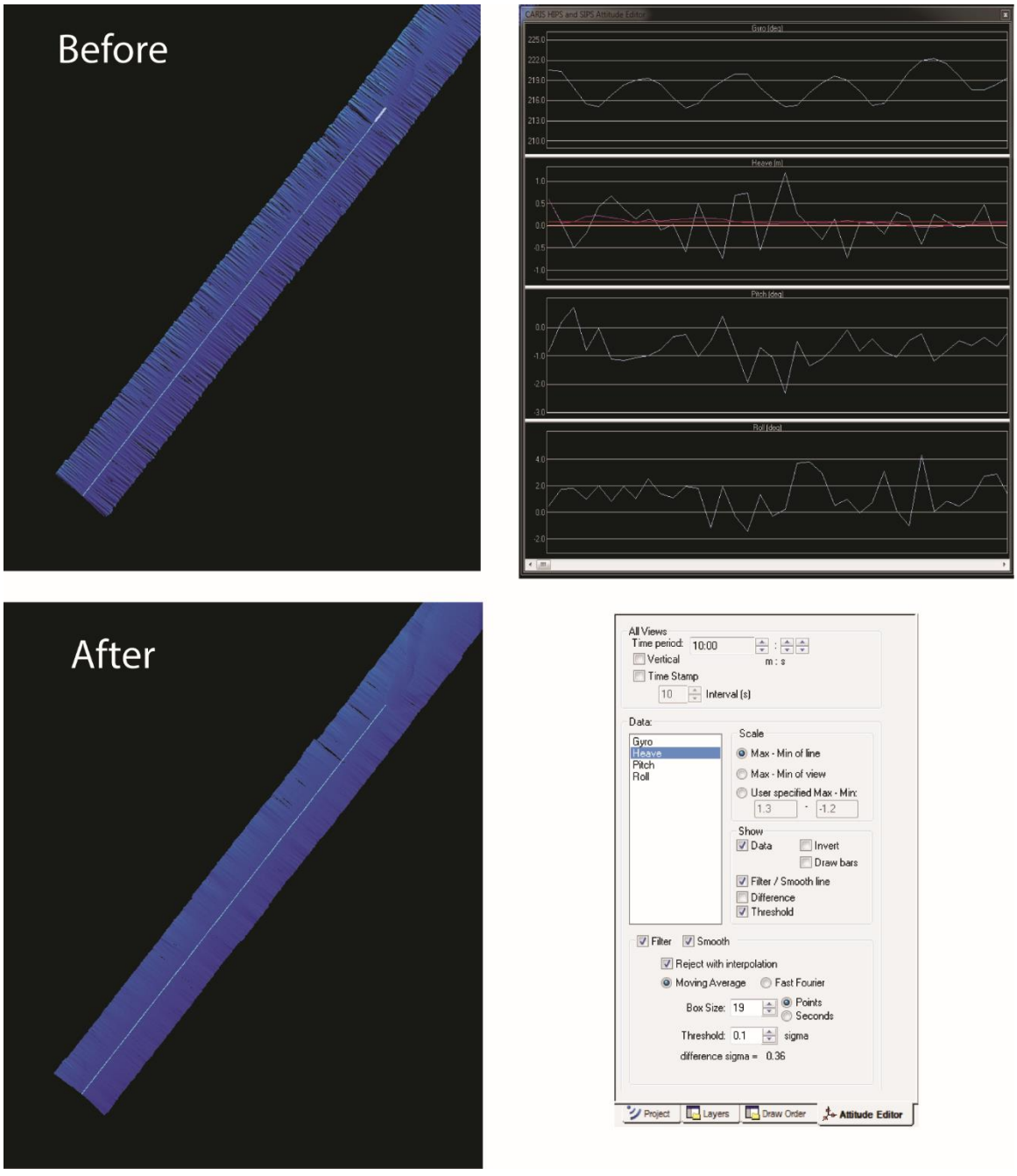

Figure B.2: Vessel attitude adjustments to minimize the ripple effects by applying a moving average to the heave, pitch, and roll values.

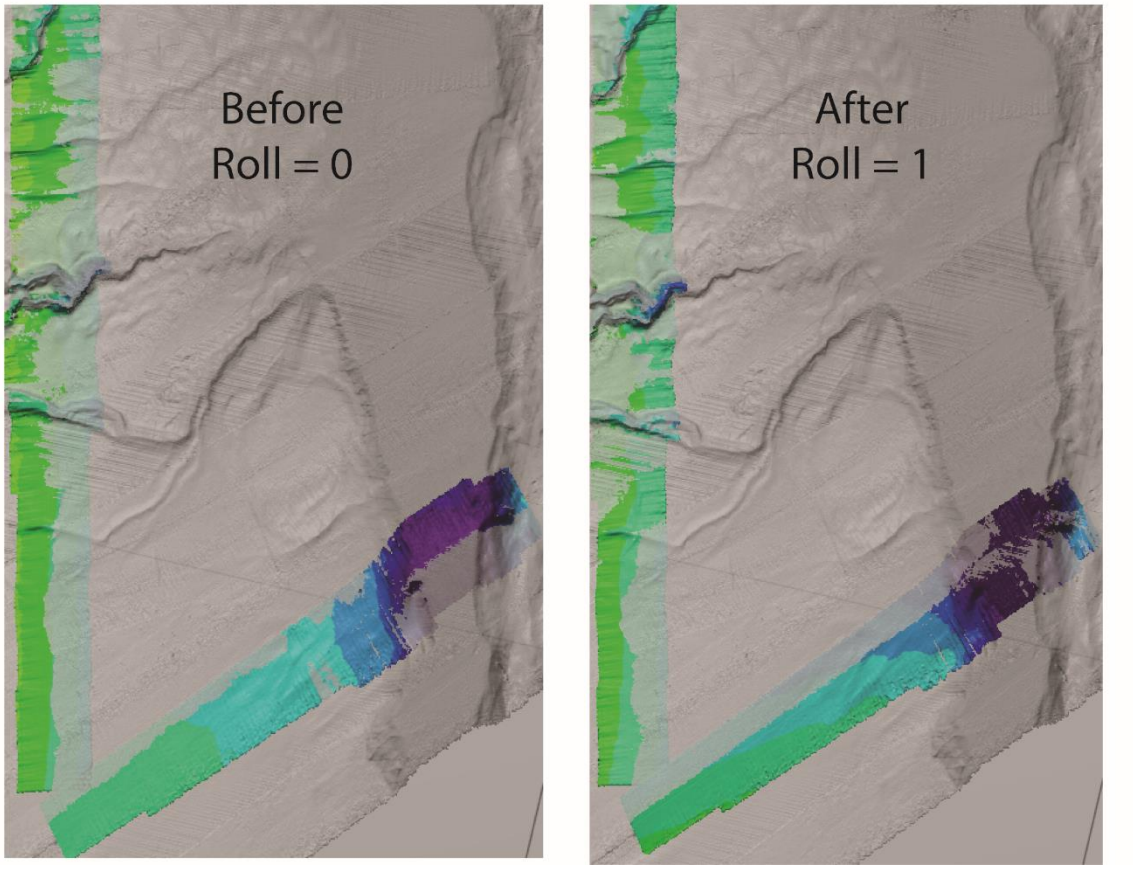

Figure B.3: Roll adjustment to minimize vessel listing. The background in greyscale is merged bathymetric data of 2005-2009 used as the reference.

Appendix C: Bathymetric processing

The processing sequence of multibeam data is following the manual of the MG&G course:

(1) Import/convert lines from their field format to Caris format

(2) Combine vessel and tide information for error processing

(3) Clean data using 'Swath Editor' and 'Subset Editor' tools

(4) Create and export a base surface

These are the steps I use for processing the SUMUT/Sonne data, using Caris Hips 7.

A. Create a project

Copy all raw data into folder pre-process under CARIS
File > project > new

Click on conversion wizard icon
A window Conversion wizard – step 1: Select the format of data, here we use Simrad, click next.
Step 2: Select create new survey lines and accept both carry over … and search directories …, click next
Step 3: File selection type: Raw data, select files in the appropriate PreProcess folder (select all data acquired on the same date), click next
Step 4: Select project, vessel and day, click vessel to add day and choose the date according to date of acquisition. Double clicking the date will create a new layer under the vessel layer, click next
Step 5: On Navigation coordinate type, select Ground and select UTM-WGS-84 and zone 46N, click next
Step 6: on navigation, select project file, accept depth, click next
Step 7: accept default for Simrad evethough it is written for EM3000, click next
Step 8: click on convert to start the process

Below is only when project and conversion of raw data was completed:
In directory CARIS/HIPS/71/HDCS _Data:

1. Create a directory containing multibeam data to process (i.e: sol198-1). This is the project name.
2. In folder sol198-1, copy file so198-1.hpf, and create folder sonne
3. Copy to folder sonne all files containing each track (ex. 2008_199 to 2008_207)
4. In folder HDCS_data/VesselConfig, put file sonne.hvf

B. Open project sol198_1

On project window show project sol198_1 and all tracks under sonne.

To begin correcting, need to create a fieldsheet.
Highlight (make a box) the track(s) or choose by clicking the layer(s) under sonne in the project window, the chosen track(s) is shown in yellow color, then click Proces-New Fieldsheet.

In New Field Sheet window (step 1 of 3), showing existing field sheets, be sure of the directory (using browse), write field sheet name.
Verify on scale (1:10,000), horizontal res (50 m), depth (1 m).
Click next

In New Field Sheet window (step 2 of 3), verify Projection and Datum (UTM-WGS84, zone UTM 46N). Click next

In New Field Sheet window (step 3 of 3), enter the geographic extent (field sheet area) or click monitor icon (lower left, blue) to take the area extent according to the displayed region. Click Finish

C. Opening the swath editor

Click to highlight on one of the line under track to process (ex. 2008-199, click 0001_20080717_010307_raw) on swath editor 
If no line is chosen, the icon swath editor is not active.

Then there are 6 displays:

- Overall window showing the whole field sheet

- 3D window, showing the chosen line from above, in this window one can manipulate the axis and height exaggeration to show relief. Also can manipulate the sun angle.
- Rear profile (showing all bathymetric line from the rear)
- Side profile (showing all bathymetric line from the side)
- Plan profile (showing all bathymetric line from above)
- Profile window, showing only 1 bathymetric line

The red color show left side of vessel and green is right side. Gray color is deleted part.

On profile window, to move from 1 line to the next, click on moving scroller on right side.

D. To start correcting

After clicking the file under day** so that swath editor is active, click the swath editor, there is another layer in the left named 'swath editor' with 2 tabs named: General and 3D View. For vertical exaggeration choose the number not more than 10. Usually 5 is fine.

Icons for corrections are: 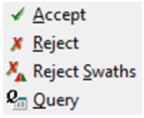

if click on RHM button or displayed in toolbar.
To delete a part of a line, choose 'reject' icon, where the curser will show an x, and highlight the part to delete. The deleted part is in gray color.

E. Correcting method

Delete any part that are not similar to adjacent lines, for example, any outliers, spikes, valleys or large bumps not similar to neighboring lines.
Inspect every line for the whole field sheet. If in doubt, any spike less than 100 m difference in height is to be allowed.

Choose accept button to allow any part of line that was deleted.

F. Finish correcting

When finish correcting a fieldsheet, click swath editor and save file.

G. Surface calculation

1. For first time surface calculation, choose the ‘Layers’ tab and choose the fieldsheet so the icon New Base Surface  is active.

On Base Surface Wizard window (step 1 of 3):
Write surface name, click next

On Base Surface Wizard window (step 2 of 3):
Choose resolution Single = 50 m, Surface type: swath angle (default), click next

On Base Surface Wizard window (step 3 of 3):
Accept the default and click finish
Then surface is calculated, after finish, there are 7 new layers under the surface name.
Click on ‘Depth’ and refresh icon  to display the colored bathymetry.

2. If surface is already calculated, need to do recomputed surface by clicking 

H. To export bathymetric data

Click on export wizard icon  or from menu File-Export-Export wizard.
On CARIS HIPS and SIPS Export Wizard – Step 1:
Choose BASE Surface to ASCII. Click next

On CARIS HIPS and SIPS Export Wizard – Step 2 of 5
Choose surface name and click next

On CARIS HIPS and SIPS Export Wizard – Step 3 of 5
Write output file in correct directory.
In Position units: Geographic DD and choose precision
Pick Depth available and Add to Active
Set Attribute precision and the delimiter (comma), click next

On CARIS HIPS and SIPS Export Wizard – Step 4 of 5
Select units of vertical length (meter) and click next

On CARIS HIPS and SIPS Export Wizard – Step 5 of 5
Click Export to start the process.

Appendix D: Steps of bathymetric difference

D.1 Calculate mean depth and standard deviation in CARIS Hips/Sips

To calculate the average depth and standard deviation of depth in CARIS has to be done when creating the base surface. Be sure to select the 'additional attribute' on step 3 when creating Base Surface. For BJ data, I use resolution 100 m, surface type: swath angle, vertical datum: unknown.

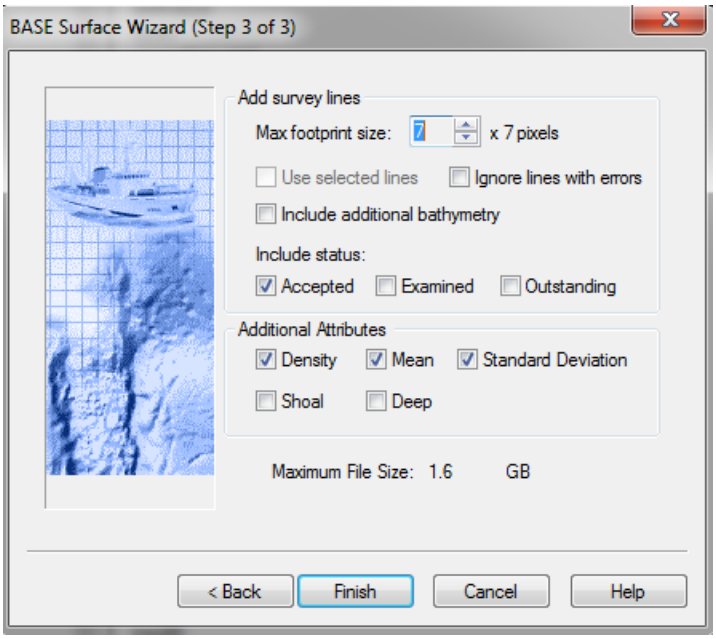

Figure D.1: The window to choose additional attributes.

$$\text{Depth Uncertainty} = \sqrt{a^2 + (b \times d)^2}$$

Standard deviation uses this equation:

a = constant depth error (sum of all constant error)

b = factor of depth dependent error,

d = depth

b*d = depth dependent error

The resulting surface and displaying the standard deviation layer looks like this:

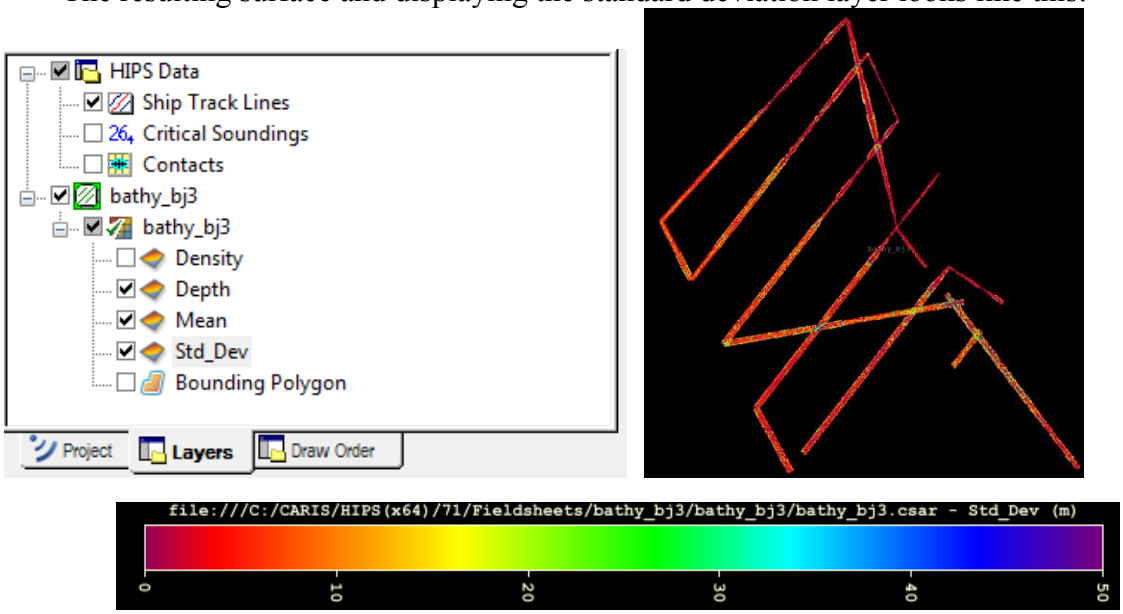

Figure D.2: Display of depth errors calculated.

To compute statistics of a layer, highlight/choose the layer to compute, and then click on main menu: Tools, Surfaces, Compute statistics, Entire dataset.

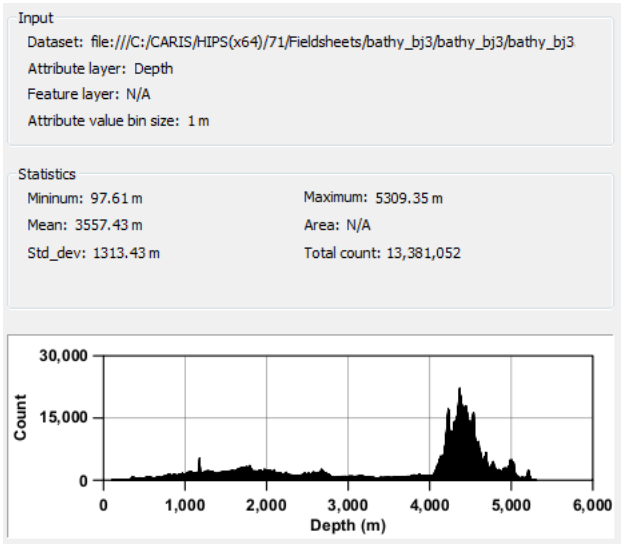

Figure D.3: Statistic result.

To export a surface into ASCII format, with the surface highlighted, on main menu choose File, Export, Surface to ASCII.

On Options, choose: geographic DD, Decimal degree 7 precision, Select all attributes, Output distance precision 4, Delimiter comma and include header, Down is positive.

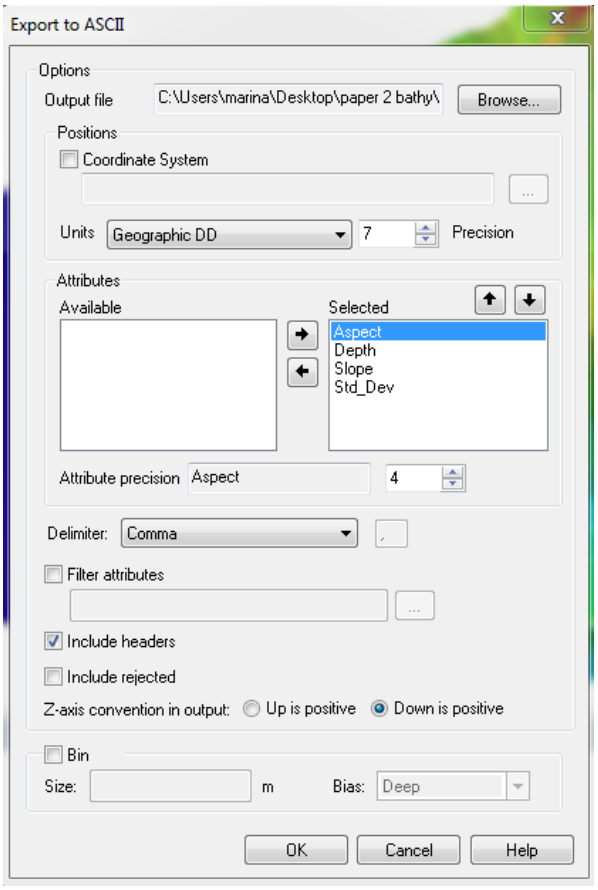

Figure D.4: A display for exporting to ASCII format.

D.2 Create surface difference in CARIS Hips/Sips

To calculate surface difference, make sure both surfaces are of the same cell resolution. From main menu: Tools, Surfaces, Difference, and then choose the surfaces to calculate.

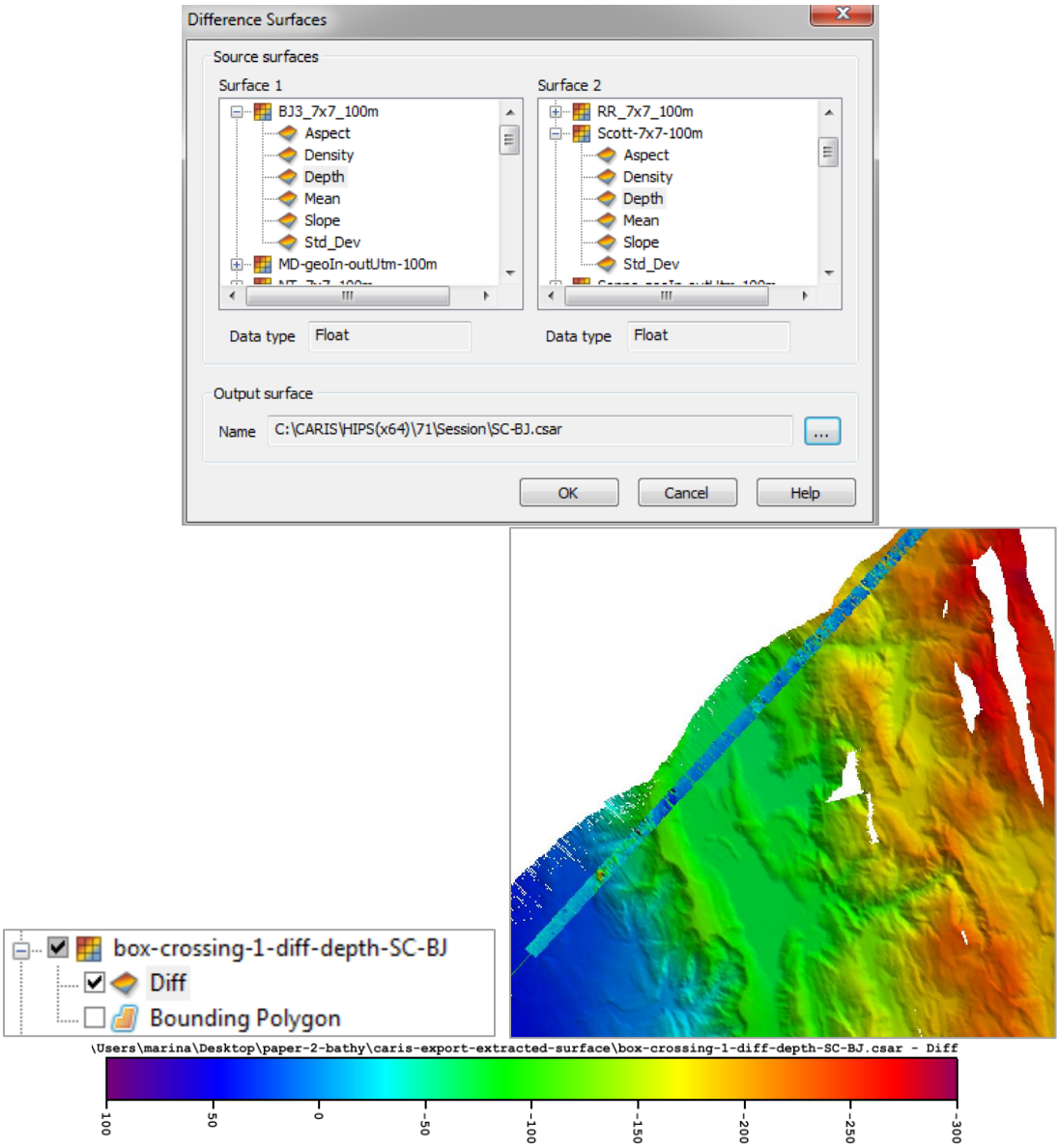

Figure D.5: The window to create surface difference and the result.

D.3 Create a surface profile in CARIS Hips/Sips

To create a depth profile along a line, from main menu: Tools, Profile, By digitation, and then choose the surfaces in the 'Profile Settings'. To create multiple profiles, choose the surface in this 'Profile settings'

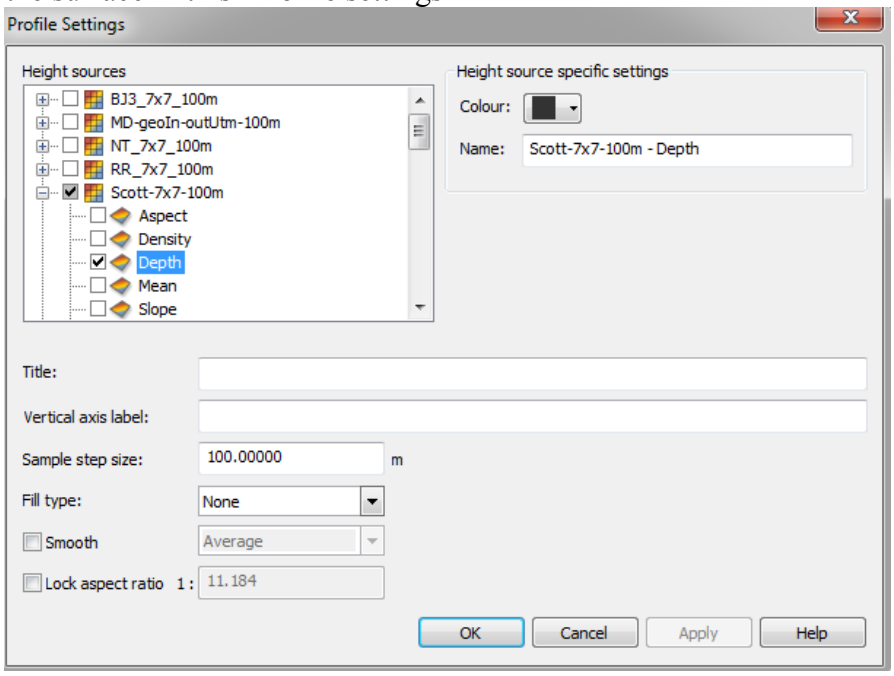

Below is a result along a transect line displaying depths and depth difference:

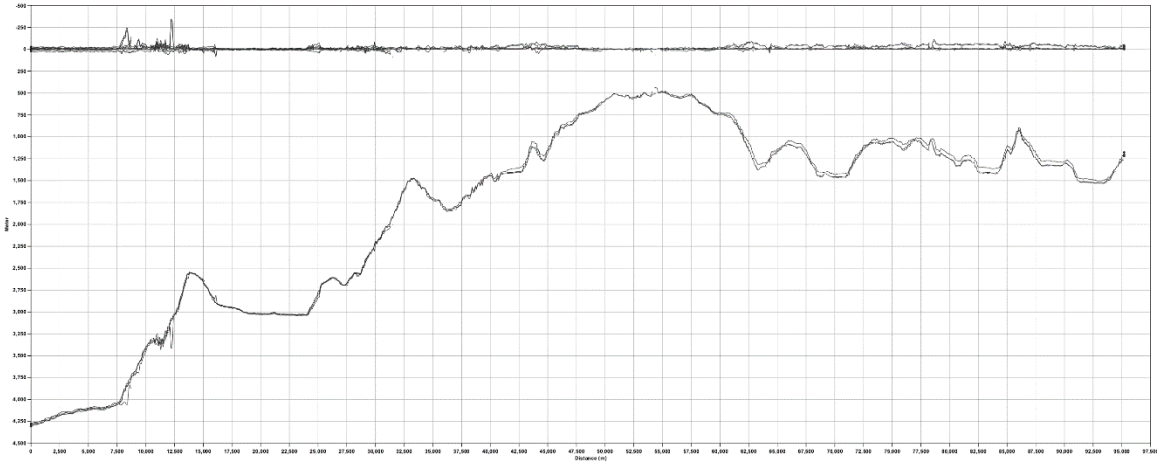

Figure D.6: The window for creating profile and the result.

D.4 A tool for looking at Simrad file

It is called HIP and SIPS Line utilities GUI. Open the GUI and choose the utility name: dumpem. Write output file and choose location to save. Choose to run simradFile.all (an example location for that file is: C:\CARIS\HIPS(x64)\71\HDCS_Data\bathy_bj3\ bathy_bj3\1997-358\1017_241297_150536_raw).

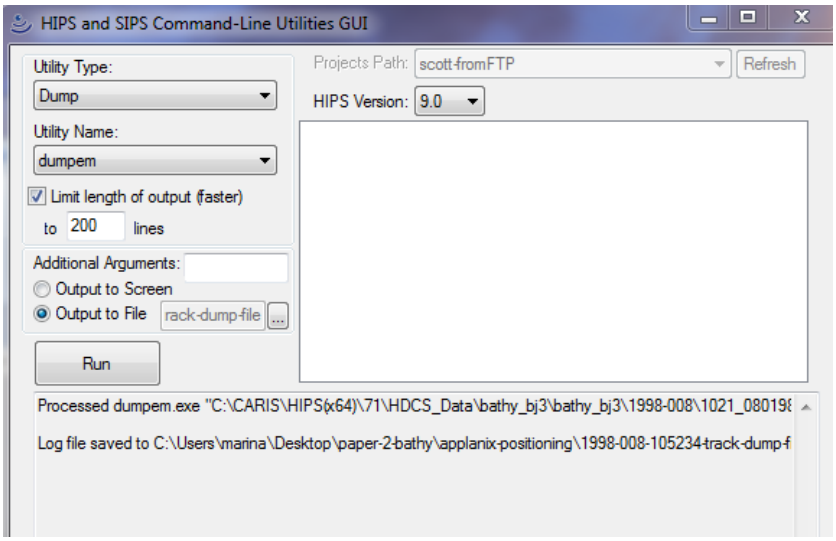

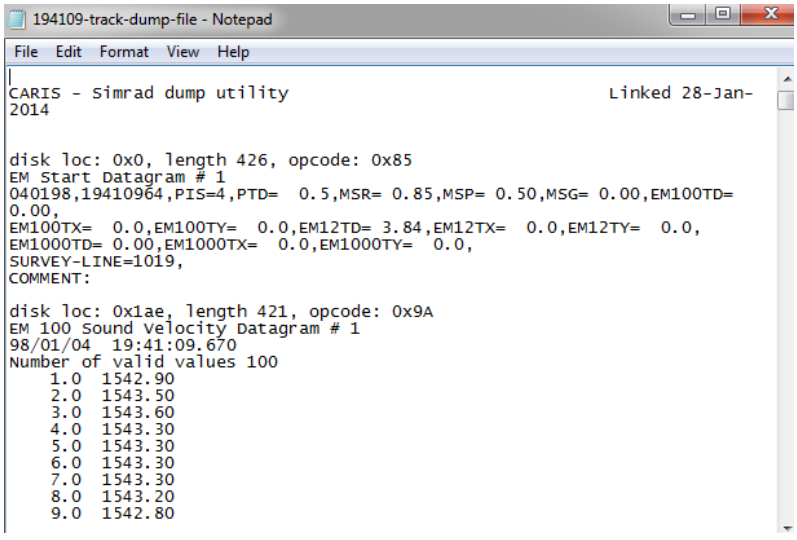

Figure D.7: The window to read a SIMRAD file and the result.

Use the dump file to look at the depth reading and the reading frequency and missing depth reading.

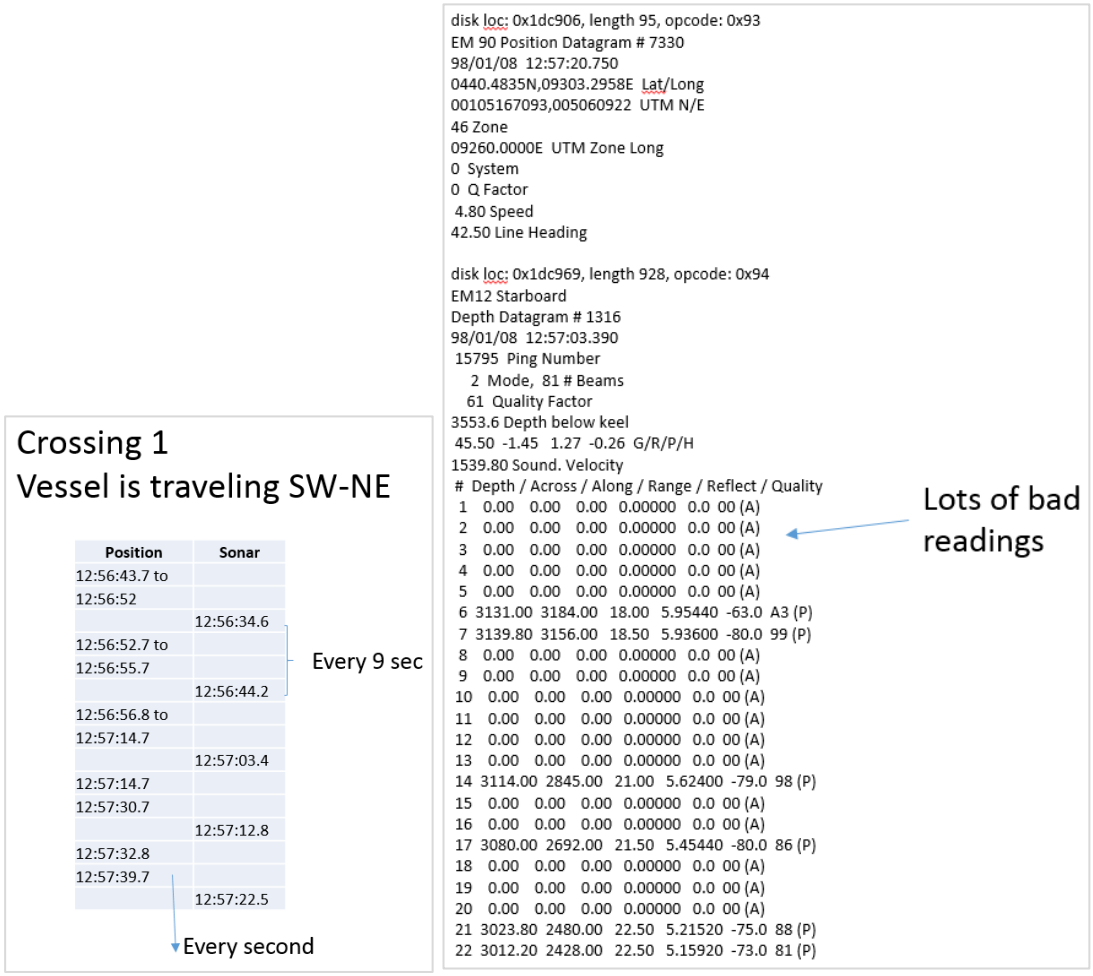

Figure D.8: A display to search for vessel information and depth readings.

D.5 To check on vessel speed and course in CARIS

Use the Navigation Editor for checking the speed and course.

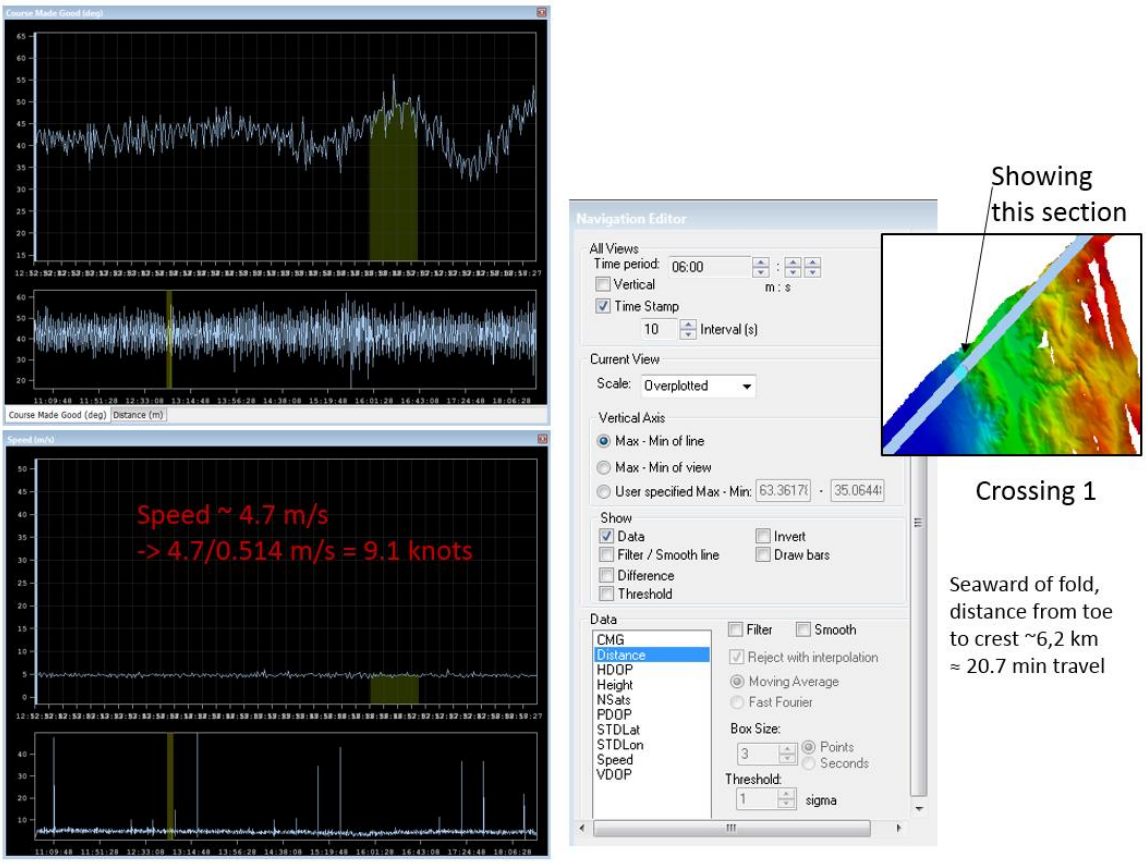

Figure D.9: A window showing the course and speed of vessel.

D.6 Display and smoothing of depth profiles in Matlab

Import ASCII of transects lines and the following is the steps to create a smoother depth and slope profiles in Matlab.

```
>> figure
>> ax=plotyy(Bjdist,Bjdepthsmo3,Bjdist,Bjslope1smo);
>> set(ax(1),'XLim',[6000 13000]);
>> set(ax(2),'XLim',[6000 13000]);
>> set(ax(1),'YDir','reverse');
>> set(ax(1),'YTick',0:1000:8000);
>> set(ax(2),'YTick',0:10:80);
>> set(ax(1),'YLim',[2000 6000]);
>> set(ax(2),'YLim',[0 100]);
>> set(ax(1),'YColor','k');
>> set(ax(2),'YColor','k');
>> axes(ax(1))
>> hold on
>> plot(Scdist,Scdepthsmo3,'g');
>> plot(Rrdist,Rrdepthsmo3,'r');
>> legend('BJ','SC','RR');
>> axes(ax(2))
>> hold on
>> plot(Scdist,Scslope1smo3,'g');
>> plot(Rrdist,Rrslope1smo3,'r');
>> xlabel('Distance (meter)');
>> set(get(ax(1),'YLabel'),'String','Seafloor Depth (meter)');
>> set(get(ax(2),'YLabel'),'String','Seafloor Slope (degree)');
```

Appendix E: Steps of seismic processing using ProMAX on Kodiak data

Basic sequences of seismic segy data processing, based on the manual written by John Miller of USGS, the steps include:

- Initial data input
- Geometry, where ProMAX use the 2D marine spreadsheet
- Assignment of geometry to traces using the Inline Geom Header Load module
- Pre-stack testing: include velocity analysis performed on CDP supergather, brute stack and pick velocities, migration using the Stolt F-K migration module
- Pre-stack depth migration using the Korchhoff Depth migration module
- Multiple suppression using the Radon analysis and Radon filter

Appendix F: Seismic SEGY and navigation file import to Landmark

F.1 Landmark 2D seismic import manual (PostStack/PAL method)

(This was originally Maureen Walton's cookbook, revised specifically for importing SEGY files around Kodiak processed in USGS Denver that were pre-stack depth migrated)
Note: start importing SEGY file then the navigation file.

1) Start OpenWorks menu (startow), select project
2) Applications -> Seismic processing -> PostStack/PAL
    a. Select 2D and PostStack
    b. Launch
    c. If there's an informational message, just click OK
    d. Select interp ID
3) In the session window…
    a. Make sure there is an empty process (add a process if there isn't, Edit -> Add)
    b. Input data -> SEGY -> parameters
    c. Click OK on any informational messages
4) In the SEG-Y Data Input window…
    a. Disk -> analyze
5) In the SEGY Analyzer window…
    a. File -> select to pick the segy files you want to import
    b. Press "start" at the top and segy information should populate the table. Choose 'both byte 21" as template header name
    c. Select the lines containing info for segy files you would like to import, and click "send selected" at the bottom. If you want to import all the files, click "send all."
    d. Keep this window open in case you need to import more files later
6) Back to the SEGY data input window…
    a. Select "Enter Linenames"
    b. The top line (should say "line 1") is extra. Select the top line, go to edit -> delete rows to remove it.
    c. Under "prefix," enter in what you would like the prefix of your line to be (commonly, it'll be the survey name with an underscore e.g. ew0408_). If

you have multiple lines you're importing, you can save yourself some steps by selecting all of the lines in the table and going to edit -> prefix linename to set a prefix for all of these lines.

   d. Under "linename," enter the specific linename you would like to use (typically just a number like 05, 24, etc).
   e. Hint: the prefix and the linename put together should match the common and unique linenames you entered when importing navigation data.
   f. On Data domain, choose depth
   g. Once you finish entering linenames, you can close out of the window file -> close.

7) Click OK on SEGY Data Input window, OK on smaller Input Data window
8) Back to Session window…
   a. Output data -> vertical -> parameters
9) In Vertical File Parameters window…
   a. Select "List," then search for a 32-bit dataset: depth 32 bit
   b. On vertical parameter window: format is floating point
   c. Click "Basemap Info" at the bottom
      i. Choose "not overwrite" especially if navigation file exist
      ii. Select the appropriate survey and input cartographic system (WGS 84 (4326), note to choose the one with space between WGS and 84.
      iii. Decimate shotpoints at 20 m
      iv. Duplicate shotpoints, last shot point
      v. Click close
10) Click OK on Vertical File Parameters, OK on the informational message, and OK on smaller Output Data window
11) Click Run
12) If you finish normally, great. If you finish with error, you can check out a detailed error message by going to the top of the Session window and clicking Job -> View.
13) Once you have a 32-bit dataset, you'll most likely need to convert it to 8 bit in order to more efficiently work with it in Landmark. It's a very similar process. Note: Landmark can display 32 bit, I didn't convert to 8 bit for Kodiak files.
14) In Session window…
   a. Input Data -> SeisWorks Seismic -> Parameters
15) In Seisworks Input window…

a. Select “list” at the top and choose the 32 bit dataset to which you just imported your segy files
b. Select the other “list” in the Seisworks window, choose the specific lines you would like to convert
c. Click OK

16) Click OK on the small Input Data window
17) Back to the Session window….
    a. Output data -> vertical -> parameters
18) In Vertical File Parameters window…
    a. Select “List,” then search for an 8-bit dataset you’d like to output to
    b. Format is 8 bit, scaling is Automatic
    c. Check “Scale each line independently,” 98 and 98 are fine for trace and dataset percentiles
    d. Click “Basemap Info” at the bottom
        i. Select the appropriate survey and input cartographic system (remember that you are inputting data from within the project now so it’ll have the project datum)
        ii. Decimate shotpoints at 20 m
        iii. Duplicate shotpoints, skip line
        iv. Click close
19) Click OK on Vertical File Parameters, OK on the informational message, and OK on smaller Output Data window
20) Click Run
21) If you finish normally, great. If you finish with error, you can check out a detailed error message by going to the top of the Session window and clicking Job -> View
22) Check out your lines in DecisionSpace Desktop and/or the Seismic Data Manager

F.2 Landmark navigation import manual

(This was originally Maureen Walton's cookbook, revised specifically for importing SEGY files around Kodiak processed in USGS Denver that were pre-stack depth migrated)

1) Start OpenWorks menu
2) Data -> Import -> Data import, select project (*GOA*) and interp ID (*LGC*)
3) "Data type" tab
    a. Import data type: "Seismic 2D line" (unless you are importing different data)
    b. Select file to import (one line at a time, or you may have a file that has different seismic lines separated by specific string).
    c. You can now choose whether to define a new import format. Definitely do this ("interactively define a new format") if you need to import a lot of files that are formatted similarly. Once you've defined and saved a format, you can use your saved format to save yourself a lot of steps later on. Usually, "scanning the data file to automatically discover the format" option is ineffective, but it may be worth a try if you have industry data.
    d. Click "continue" at the bottom.
4) "Format" tab
    a. In the left panel, if it's not already there, you can add "Seis 2D Line" as a data category using the + symbol
    b. "File layout" subtab
        i. Input data fields are: fixed width or delimited, depending on your data – fixed width has a bit more flexibility but is more tedious
        ii. (optional) select your delimeter
        iii. Usually comment defaults are ok. Update this if you have non-traditional comments or want certain lines of your data ignored
    c. "File section" subtab
        i. If you are just importing nav for one seismic line, select "Indicated by" and "one" (*I edit the navigation file to contain single line for each file)*
        ii. If you are importing multiple lines from one nav file, select "multiple" and enter the line separator
    d. "Data items" subtab – very important!!

i. Under “undefined data items”, select each item you’d like to define in turn. You MUST define each item with an *, as well as latitude, longitude, shotpoint, and trace. (*Common & unique are should be the same, ex: L-8-81-WG_102. Where L-8-81-WG is survey name and 102 is line name*)
ii. Decimation tolerance= 20 (or 10 for MGL1109-15d)
iii. Directory name and survey ID: click to choose appropriate survey
iv. Z-datum= 0
v. On edited navigation file, trace, CDP, shotpoint are on same column
vi. The rightmost panel is where you actually define values by either selecting a delimited column (if you selected delimited data earlier) or by highlighting the data in the first line that it appears (if you selected fixed width earlier). For both options, you’ll select these values from your previewed data in the bottom panel.

5) “2D Navigation” tab
    a. Use last shotpoint
    b. Check “calculate missing trace ranges from the input data”
6) “Conversions” tab
    a. Be sure to select the input datum under “cartographic reference system”, Geo coordinate system subtab, dega
    b. Measurement system should be “SPE Preferred Metric”
7) “Import Data” tab
    a. Click the green running man
    b. Once the import is completed, you can see any errors under the “Import Log” and “Error” tabs
8) Open Decision Space Desktop for GOA (*Alaska session*) and make sure the line is present
9) On Seismic Data Manager (Data> Management > Seismic Data manager) and check on Original CRS that it is in meters, if not need to convert. On Geo Coordinate System tab, choose 98 WGS1984 > 703 WGS 84 [4326]. Be sure to choose the one with space between WGS and 84.

Appendix G: Matlab script for MGL1109 gravity data

The gravity file does not contain the vessel's position, only time and gravity data. This script is to use the vessel's navigation data to calculate the vessel's position for each gravity reading.

```
>> grav_table=xlsread('C:\Users\marina\Desktop\kodiak-files\MGL1109_grav_magn\
gravity_data\gravity_only_4matlab.xlsx');
>> nav_table=xlsread('C:\Users\marina\Desktop\kodiak-files\MGL1109_grav_magn\
gravity_data\nav_only_4matlab.xlsx');
>> gravhms=[grav_table(:,2)];
>> navhms=[nav_table(:,1)];
>> grav_id_keep=[];
>> nav_id_keep=[];
>> for i=1:length(gravhms)
grav_tmp=gravhms(i);
diff_hms=navhms-grav_tmp;
diff_min=min(abs(diff_hms));
if diff_min <= 0.0002
id_tmp_nav=find(abs(diff_hms)==diff_min);
id_tmp_grav=i;
end
grav_id_keep=[grav_id_keep;id_tmp_grav];
nav_id_keep=[nav_id_keep;id_tmp_nav];
end
>> grav_new=grav_table(grav_id_keep,:);
>> nav_new=nav_table(nav_id_keep,:);
>> new_table=[grav_new,nav_new];
>> csvwrite('gravity.txt',new_table);
```

Appendix H: File archive in UTIG network

- Marina's PhD files: \\UTIG2\disk_staff\sean\sumatra_bgr
    - Bathymetry data: (1) Alaska consists of bathymetric data from GEOMAR and downloaded SRTM data and Alaska region digital DEM (Ardem), (2) Sumatra consists of the surveys I collected to create the merged bathymetry. Folders are listed under name of vessel and the cruise reports are included.
    - Dissertation files contains files and figures for the dissertation
    - EndNote contains list of references used in the dissertation
    - Kodiak seismic contains segy and navigation files
    - Paper - 1, contains files accepted in Tectonics
    - Softwares contain ArcGIS projects, CARIS projects, Fledermaus scenes, GMT scripts, and Kodiak's Matlab script.
    - Talks/presentations contains the power point files
- Marina's GMT scripts modified from Kylara Martin's: \\UTIG3\sg4\gmt_stuff
- Additional Sumatra seismic files: \\utig2\disk_staff\sean\Sumatra_seismic_files\
- Sumatra raw bathymetric files: \\UTIG2\disk_staff\sean\sumatra_bgr\raw-data
- Kodiak seismic files: \\utig2\disk_staff\sean\alaska\kodiak
- Kylara Martin's archives for Sumatra's related files: \\UTIG3\sg4\

References

Ammon, C. J., et al. (2005), Rupture process of the 2004 Sumatra-Andaman earthquake, *Science*, *308*.

Banerjee, P., F. Pollitz, B. Nagarajan, and R. Burgmann (2007), Coseismic Slip Distributions of the 26 December 2004 Sumatra-Andaman and 28 March 2005 Nias Earthquakes from GPS Static Offsets, *Bulletin of the Seismological Society of America*, *97*, S86-S102.

Bangs, N. L. B., S. P. S. Gulick, and T. H. Shipley (2006), Seamount subduction erosion in the Nankai Trough and its potential impact on the seismogenic zone, *Geology*, *34*, 701.

Barber, A. J., and M. J. Crow (2003), An Evaluation of Plate Tectonic Models for the Development of Sumatra, *Gondwana Research*, *6*, 1-28.

Barnes, P. M., G. Lamarche, J. Bialas, S. Henrys, I. Pecher, G. L. Netzeband, J. Greinert, J. J. Mountjoy, K. Pedley, and G. Crutchley (2010), Tectonic and geological framework for gas hydrates and cold seeps on the Hikurangi subduction margin, New Zealand, *Marine Geology*, *272*(1-4), 26-48.

Becker, J. J., et al. (2009), Global Bathymetry and Elevation Data at 30 Arc Seconds Resolution: SRTM30_PLUS, *Marine Geodesy*, *32*(4), 355-371.

Berglar, K., C. Gaedicke, R. Lutz, D. Franke, and Y. S. Djajadihardja (2008), Neogene subsidence and stratigraphy of the Simeulue forearc basin, Northwest Sumatra, *Marine Geology*, *253*, 1-13.

Berglar, K., C. Gaedicke, D. Franke, S. Ladage, F. Klingelhoefer, and Y. S. Djajadihardja (2010), Structural evolution and strike-slip tectonics off north-western Sumatra, *Tectonophysics*, *480*, 119-132.

Bowles, F. A., W. F. Ruddiman, and W. H. Jahn (1978), Acoustic stratigraphy, structure, and depositional history of the Nicobar Fan, Eastern Indian Ocean, *Marine Geology*, *26*, 269-288.

Briggs, R. W., et al. (2006), Deformation and slip along the Sunda megathrust in the great 2005 Nias-Simeulue earthquake, *Science*, *311*.

Brocher, T. M. (2005), Compressional and Shear Wave Velocity Versus Depth in the San Francisco Bay Area, California: Rules for USGS Bay Area Velocity*Rep.*, 1-58 pp, USGS.

Byrne, D. E., W.-h. Wang, and D. M. Davis (1993), Mechanical role of backstops in the growth of forearcs, *Tectonics*, *12*, 123-144.

Byrne, T., and J. Hibbard (1987), Landward vergence in accretionary prisms: The role of the backstop and thermal history, *Geology*, *15*(12), 1163.

Chadwell, C. D., P. Lonsdale, J. W. Kluesner, A. D. Sweeney, W. Weinrebe, J. H. Behrmann, J. L. Diaz-Naveas, and E. Contreras-Reyes (2010), An examination of ``before'' and ``after'' bathymetry for uplift of the sea floor following the Feb. 27, 2010 Maule, Chile Earthquake, paper presented at AGU Fall Meeting 2010.

Chauhan, A. P. S., S. C. Singh, N. D. Hananto, H. Carton, F. Klingelhoefer, J. X. Dessa, H. Permana, N. J. White, and D. Graindorge (2009), Seismic imaging of forearc

backthrusts at northern Sumatra subduction zone, *Geophysical Journal International*, *179*, 1772-1780.
Chaytor, J. D., U. S. ten Brink, A. R. Solow, and B. D. Andrews (2009), Size distribution of submarine landslides along the U.S. Atlantic margin, *Marine Geology*, *264*(1-2), 16-27.
Chlieh, M., et al. (2007), Coseismic Slip and Afterslip of the Great Mw 9.15 Sumatra-Andaman Earthquake of 2004, *Bulletin of the Seismological Society of America*, *97*(1A), S152-S173.
Clare, M. A., P. J. Talling, P. Challenor, G. Malgesini, and J. Hunt (2014), Distal turbidites reveal a common distribution for large (>0.1 km3) submarine landslide recurrence, *Geology*, *42*, 263-266.
Curray, J. R. (2005), Tectonics and history of the Andaman Sea region, *Journal of Asian Earth Sciences*, *25*(1), 187-232.
Curray, J. R., and D. G. Moore (1971), Growth of the Bengal deep-sea fan and denundation in the Himalayas, *GSA Bulletin*, *82*, 563-572.
Curray, J. R., and D. G. Moore (1974), Sedimentary and tectonic processes in the Bengal deep-sea fan and geosyncline, in *The geology of continental margins*, edited by C. A. Burk and C. L. Drake, pp. 617-627, Springer-Verlag, New York.
Dalrymple, G. B., D. A. Clague, T. L. Vallier, and H. W. Menard (1987), 40Ar/39Ar Age, petrology, and tectonic significance of some seamounts in the Gulf of Alaska, in *Seamounts,, Islands, and Atolls*, edited by B. H. Keating, P. Fryer, R. Batiza and G. W. Boehlert, pp. 297-315, American Geophysical Union, Washington, D. C.
Davis, D. M., J. Suppe, and F. A. Dahlen (1983), Mechanics of fold-and-thrust belts and accretionary wedges, *Journal of Geophysical Research*, *88*, 1153-1172.
Dean, S. M., L. C. McNeill, T. J. Henstock, J. M. Bull, S. P. S. Gulick, J. A. Austin, Jr, N. L. B. Bangs, Y. S. Djajadihardja, and H. Permana (2010), Contrasting décollement and prism properties over the Sumatra 2004-2005 earthquake rupture boundary, *Science*, *329*, 207-210.
Dominguez, S., J. Malavieille, and S. E. Lallemand (2000), Deformation of accretionary wedges in response to seamount subduction: Insights from sandbox experiments, *Tectonics*, *19*(1), 182-196.
Dorobek, S. L. (2008), Carbonate-platform facies in volcanic-arc settings: Characteristics and controls on deposition and stratigraphic development, *GSA Special paper*, *436*, 55-90.
Engebretson, D. C., A. Cox, and R. G. Gordon (1985), Relative motions between oceanic plates of the Pacific Basin, *Journal of Geophysical Research*, *89*, 10291.
Fine, I. V., A. B. Rabinovich, and R. E. Thomson (2005), The dual source region for the 2004 Sumatra tsunami, *Geophysical Research Letters*, *32*(16).
Finn, S. P., L. M. Liberty, P. J. Haeussler, and T. L. Pratt (2015), Landslides and megathrust splay faults captured by the late holocene sediment record of eastern Prince William Sound, Alaska, *Bulletin of the Seismological Society of America*, *105*, 2343-2353.

Fisher, D., D. C. Mosher, J. A. Austin, Jr, S. P. S. Gulick, T. Masterlark, and K. Moran (2007), Active deformation across the Sumatran forearc over the December 2004 Mw 9.2 rupture, *Geology*, *35*, 99.

Frederik, M. C. G., S. P. S. Gulick, J. A. Austin, and N. L. B. Bangs (2015), What 2-D multichannel seismic and multibeam bathymetric data tell us about the North Sumatra wedge structure and coseismic response, *Tectonics*, *34*, 1-17.

Fruehn, J., R. von Huene, and M. A. Fisher (1999), Accretion in the wake of terrane collision: The Neogene accretionary wedge off Kenai Peninsula, Alaska, *Tectonics*, *18*, 263-277.

Fujiwara, T., S. Kodaira, T. No, Y. Kaiho, N. Takahashi, and Y. Kaneda (2011), The 2011 Tohoku-Oki earthquake: displacement reaching the trench axis, *Science*, *334*, 1240.

Geersen, J., L. McNeill, T. J. Henstock, and C. Gaedicke (2013), The 2004 Aceh-Andaman Earthquake: Early clay dehydration controls shallow seismic rupture, *Geochemistry, Geophysics, Geosystems*, *14*(9), 3315-3323.

Geist, E. L., S. L. Bilek, D. Arcas, and V. Titov (2006), Differences in tsunami generation between the December 26, 2004 and March 28, 2005 Sumatra earthquakes, *Earth Planets Space*, *58*.

Goldfinger, C., L. V. D. Kulm, L. C. McNeill, and P. H. W. Atts (2000), Super-scale Failure of the Southern Oregon Cascadia Margin, *Pure and Applied Geophysics*, *157*, 1189-1226.

Graindorge, D., et al. (2008), Impact of lower plate structure on upper plate deformation at the NW Sumatran convergent margin from seafloor morphology, *Earth and Planetary Science Letters*, *275*, 201-210.

Gulick, S. P. S., A. M. Meltzer, and S. H. Clarke (1998), Seismic structure of the southern Cascadia subduction zone and accretionary prism north of the Mendocino triple junction, *Journal of Geophysical Research*, *103*, 27207-27222.

Gulick, S. P. S., N. L. B. Bangs, T. H. Shipley, Y. Nakamura, G. Moore, and S. Kuramoto (2004), Three-dimensional architecture of the Nankai accretionary prism's imbricate thrust zone off Cape Muroto, Japan: Prism reconstruction via en echelon thrust propagation, *Journal of Geophysical Research*, *109*, 1-12.

Gulick, S. P. S., J. A. J. Austin, L. C. McNeill, N. L. B. Bangs, K. M. Martin, T. J. Henstock, J. M. Bull, S. M. Dean, Y. S. Djajadihardja, and H. Permana (2011), Updip rupture of the 2004 Sumatra earthquake extended by thick indurated sediments, *Nature Geoscience*, *4*, 453-456.

Gulick, S. P. S., et al. (2015), Mid-Pleistocene climate transition drives net mass loss from rapidly uplifting St. Elias Mountains, Alaska, *Proceedings of the National Academy of Sciences*, 1-6.

Gunawan, E., et al. (2014), A comprehensive model of postseismic deformation of the 2004 Sumatra-Andaman earthquake deduced from GPS observations in northern Sumatra, *Journal of Asian Earth Sciences*, *88*, 218-229.

Gutscher, M.-a., N. Kukowski, J. Malavieille, and S. Lallemand (1998), Episodic imbricate thrusting and underthrusting: Analog experiments and mechanical analysis

applied to the Alaskan Accretionary Wedge, *Journal of Geophysical Research*, *103*, 10161-10176.
Gutscher, M.-a., D. Klaeschen, E. R. Flueh, J. Malavieille, and D. Kiel (2001), Non-Coulomb wedges, wrong-way thrusting, and natural hazards in Cascadia, *Geology*, *29*, 379-382.
Haeussler, P. J., P. A. Armstrong, L. M. Liberty, K. M. Ferguson, S. P. Finn, J. C. Arkle, and T. L. Pratt (2015), Focused exhumation along megathrust splay faults in Prince William Sound, Alaska, *Quaternary Science Reviews*, *113*, 8-22.
Hampton, M. A., H. J. Lee, and J. Locat (1996), Submarine landslides, *Reviews of Geophysics*, *34*(1), 33-59.
Henstock, T. J., L. C. McNeill, and D. R. Tappin (2006), Seafloor morphology of the Sumatran subduction zone: surface rupture during megathrust earthquakes?, *Geology*, *34*, 485.
Heuret, A., C. P. Conrad, F. Funiciello, S. Lallemand, and L. Sandri (2012), Relation between subduction megathrust earthquakes, trench sediment thickness and upper plate strain, *Geophysical Research Letters*, *39*, 1-6.
Hirata, K., K. Satake, Y. Tanioka, T. Kuragano, Y. Hasegawa, S. Hayashi, and N. Hamada (2006), The 2004 Indian Ocean tsunami: Tsunami source model from satellite altimetry, *Earth Planets Space*, *58*, 195-201.
Hu, Y., and K. Wang (2012), Spherical-Earth finite element model of short-term postseismic deformation following the 2004 Sumatra earthquake, *Journal of Geophysical Research*, *117*(B5).
Ishii, M., P. M. Shearer, H. Houston, and J. E. Vidale (2005), Extent, duration and speed of the 2004 Sumatra-Andaman earthquake imaged by the Hi-Net array, *Nature*, *435*, 933-936.
Jaeger, J. M., S. P. S. Gulick, Shipboard, Scientific, and Party (2014), https://iodp.tamu.edu/scienceops/expeditions/alaska_tectonics_climate.html, edited, IODP Publications, Last accessed March 7, 2016.
Karig, D. E. (1977), Growth pattern on the upper trench slope, *American Geophysical Union, Maurice Ewing Series*, *1*.
Karig, D. E., S. Suparka, G. F. Moore, and P. E. Hehanussa (1979), Structure and Cenozoic Evolution of the Sunda Arc in the Central Sumatra Region, *AAPG Memoir 29*, 1-15.
Kawamura, K., J. S. Laberg, and T. Kanamatsu (2014), Potential tsunamigenic submarine landslides in active margins, *Marine Geology*, *356*, 44-49.
Kawamura, K., T. Sasaki, T. Kanamatsu, A. Sakaguchi, and Y. Ogawa (2012), Large submarine landslides in the Japan Trench: A new scenario for additional tsunami generation, *Geophysical Research Letters*, *39*(5), 1-5.
Klingelhoefer, F., M.-a. Gutscher, S. Ladage, J.-X. Dessa, D. Graindorge, D. Franke, C. André, H. Permana, T. Yudistira, and a. Chauhan (2010), Limits of the seismogenic zone in the epicentral region of the 26 December 2004 great Sumatra-Andaman earthquake: Results from seismic refraction and wide-angle reflection surveys and thermal modeling, *Journal of Geophysical Research*, *115*, B01304.

Kodaira, S., T. No, Y. Nakamura, T. Fujiwara, Y. Kaiho, S. Miura, N. Takahashi, Y. Kaneda, and A. Taira (2012), Coseismic fault rupture at the trench axis during the 2011 Tohoku-oki earthquake, *Nature Geoscience*, *5*(9), 646-650.

Kopp, H., and N. Kukowski (2003), Backstop geometry and accretionary mechanics of the Sunda margin, *Tectonics*, *22*(6).

Kopp, H., et al. (2008), Lower slope morphology of the Sumatra trench system, *Basin Research*, *20*, 519-529.

Lallemand, S. E., J. Malavieille, and S. Calassou (1992), Effects of oceanic ridge subduction on accretionary wedges: Experimental modeling and marine observations, *Tectonics*, *11*, 1301-1313.

Lallemand, S. E., P. Schnurle, and J. Malavieille (1994), Coulomb theory applied to accretionary and nonaccretionary wedges: possible causes for tectonic erosion and/or frontal accretion, *Journal of Geophysical Research*, *99*, 12033-12055.

Laursen, J., D. W. Scholl, and R. v. Huene (2002), Neotectonic deformation of the central Chile margin: Deepwater forearc basin formation in response to hot spot ridge and seamount subduction, *Tectonics*, *21*, 1-27.

Locat, J., and H. J. Lee (2002), Submarine landslides : advances and challenges, *Canada Geotechnical Journal*, *39*, 193-212.

Lutz, R., C. Gaedicke, K. Berglar, S. Schloemer, D. Franke, and Y. S. Djajadihardja (2011), Petroleum systems of the Simeulue fore-arc basin, offshore Sumatra, Indonesia, *American Association of Petroleum Geologists Bulletin*, *95*, 1589-1616.

MacKay, M. E. (1995), Structural variation and landward vergence at the toe of the Oregon accretionary prism, *Tectonics*, *14*, 1309-1320.

MacKay, M. E., G. F. Moore, G. R. Cochrane, J. Casey Moore, and L. V. D. Kulm (1992), Landward vergence and oblique structural trends in the Oregon margin accretionary prism: Implications and effect on fluid flow, *Earth and Planetary Science Letters*, *109*, 477-491.

Madsen, J. K., D. J. Thorkelson, R. M. Friedman, and D. D. Marshall (2006), Cenozoic to recent plate configurations in the Pacific Basin: Ridge subduction and slab window magmatism in Western North America, *Geosphere*, *2*, 11-34.

Malod, J.-A., et al. (1993), Déformations du bassin d'avant-arc au Nord-Ouest de Sumatra: une réponse à la subduction oblique, *Multilingue*, *316*(6), 791-797.

Martin, K. M., S. P. S. Gulick, J. A. Austin, K. Berglar, D. Franke, and Udrekh (2014), The West Andaman Fault: A complex strain-partitioning boundary at the seaward edge of the Aceh Basin, offshore Sumatra, *Tectonics*, *33*(5), 786-806.

McAdoo, B. G., M. K. Capone, and J. Minder (2004), Seafloor geomorphology of convergent margins: Implications for Cascadia seismic hazard, *Tectonics*, *23*, 1-15.

McCaffrey, R. (2009), The Tectonic framework of the Sumatran subduction zone, *Annual Review of Earth and Planetary Sciences*, *37*, 345-366.

McNeill, L. C., and T. J. Henstock (2014), Forearc structure and morphology along the Sumatra- Andaman subduction zone, *Tectonics*, *33*, 1-23.

McNeill, L. C., T. J. Henstock, D. R. Tappin, and J. R. Curray (2006), Forearc morphology and thrust vergence, Sunda subduction zone, edited, EOS, Trans. Am. Geophys. Union 87 (52) Fall Meet. Suppl., Abstract U44A-07.

Moeremans, R., S. C. Singh, M. Mukti, J. McArdle, and K. Johansen (2014), Seismic images of structural variations along the deformation front of the Andaman–Sumatra subduction zone: Implications for rupture propagation and tsunamigenesis, *Earth and Planetary Science Letters*, *386*, 75-85.

Molnar, P., and P. Tapponnier (1975), Cenozoic tectonic of Asia: Effects of a continental collision, *Science*, *189*(4201), 419-426.

Moore, C., and A. Allwardt (1980), Progressive deformation of a Tertiary Trench Slope, Kodiak Islands, Alaska, *Journal of Geophysical Research*, *85*, 4741-4756.

Moore, G. F., N. L. B. Bangs, A. Taira, S. Kuramoto, E. M. Pangborn, and H. J. Tobin (2007), Three-dimensional splay fault geometry and implications for tsunami generation, *Science*, *318*, 1128-1131.

Moran, K., and D. R. Tappin (2005), SEATOS 2005 Cruise Report: Sumatra earthquake and tsunami offshore survey (SEATOS)*Rep.*

Moran, K., S. T. Grilli, and D. R. Tappin (2005a), An overview of SEATOS: Sumatra earthquake and tsunami offshore survey, paper presented at American Geophysical Union, Fall Meeting 2005, abstract #U14A-04.

Moran, K., J. A. J. Austin, and D. R. Tappin (2005b), Survey presents broad approach to tsunami studies, *EOS*, *86*, 430-431.

Mosher, D. C., J. A. Austin, Jr, D. Fisher, and S. P. S. Gulick (2008), Deformation of the northern Sumatra accretionary prism from high-resolution seismic reflection profiles and ROV observations, *Marine Geology*, *252*, 89-99.

Müller, R. D., M. Sdrolias, C. Gaina, and W. R. Roest (2008), Age, spreading rates, and spreading asymmetry of the world's ocean crust, *Geochemistry, Geophysics, Geosystems*, *9*(4).

Natawidjaja, D. H., K. Sieh, S. N. Ward, H. Cheng, R. L. Edwards, J. Galetzka, and B. W. Suwargadi (2004), Paleogeodetic records of seismic and aseismic subduction from central Sumatran microatolls, Indonesia, *Journal of Geophysical Research*, *109*(B4).

Natawidjaja, D. H., K. Sieh, J. Galetzka, B. W. Suwargadi, H. Cheng, R. L. Edwards, and M. Chlieh (2007), Interseismic deformation above the Sunda Megathrust recorded in coral microatolls of the Mentawai islands, West Sumatra, *Journal of Geophysical Research*, *112*, 1-27.

Park, J. O., T. Tsuru, Y. Kaneda, Y. Kono, S. Kodaira, N. Takahashi, and H. Kinoshita (1999), A subducting seamount beneath the Nankai accretionary prism off Shikoku, southwestern Japan, *Geophysical Research Letters*, *26*, 931-934.

Pedley, K. L., P. M. Barnes, J. R. Pettinga, and K. B. Lewis (2010), Seafloor structural geomorphic evolution of the accretionary frontal wedge in response to seamount subduction, Poverty Indentation, New Zealand, *Marine Geology*, *270*, 119-138.

Piper, D. J. W., P. Cochonat, and M. L. Morrison (1999), The sequence of events around the epicenter of the 1929 Grand Banks earthquake: initiation of debris flows and turbidity current inferred from sidescan sonar, *Sedimentology*, *46*, 79-97.
Plafker, G. (1969), Tectonics of the March 27, 1964, Alaska earthquake, edited, US Government Printing Office, Washington, D.C.
Pollitz, F. F., R. Bürgmann, and P. Banerjee (2011), Geodetic slip model of the 2011 M9.0 Tohoku earthquake, *Geophysical Research Letters*, *38*(L00G08), 1-6.
Prawirodirdjo, L., Y. Bock, J. F. Genrich, M. Green, and S. Sutisna (2000), One century of tectonic deformation along the Sumatran fault from triangulation and Global Positioning System surveys, *Journal of Geophysical Research*, *105*, 28343-28361.
Rea, D. K., I. A. Basov, and T. Janecek (1992), Ocean Drilling Program Leg 145 preliminary report North Pacific transect*Rep.*
Reece, R. S., S. P. S. Gulick, B. K. Horton, G. L. Christeson, and L. L. Worthington (2011), Tectonic and climatic influence on the evolution of the Surveyor Fan and Channel system, Gulf of Alaska, *Geosphere*, *7*, 830-844.
Reed, D. L., E. a. Silver, J. E. Tagudin, T. H. Shipley, and P. Vrolijk (1990), Relations between mud volcanoes, thrust deformation, slope sedimentation, and gas hydrate, offshore north Panama, *Marine and Petroleum Geology*, *7*, 44-54.
Rhie, J., D. Dreger, R. Burgmann, and B. Romanowicz (2007), Slip of the 2004 Sumatra–Andaman Earthquake from Joint Inversion of Long-Period Global Seismic Waveforms and GPS Static Offsets, *Bulletin of the Seismological Society of America*, *97*, S115-S127.
Rose, R. (1983), Miocene carbonate rocks of Sibolga Basin, Northwest Sumatra, in *Twelfth Annual Convention, Indonesian Petroleum Association*, edited, pp. 107-125.
Ruff, L., and H. Kanamori (1980), Seimicity and the subduction process, *Physics of the Earth and Planetary Interiors*, *23*, 240-252.
Ruff, L. J. (1989), Do trench sediments affect great earthquake occurrence in subduction zones?, *Pure and Applied Geophysics*, *129*, 263-282.
Sawyer, D., and R. DeVore (2015), Elevated shear strength of sediments on active margins: Evidence for seismic strengthening, *Geophysical Research Letters*, *42*, 10216-10221.
Sclater, J. G., and R. L. Fisher (1974), Evolution of the East: Central Indian Ocean, with emphasis on the tectonic setting of the Ninetyeast Ridge, *GSA Bulletin*, *85*(5), 683-702.
Seeber, L., C. Mueller, T. Fujiwara, K. Arai, W. Soh, Y. Djajadihardja, and M. Cormier (2007), Accretion, mass wasting, and partitioned strain over the 26 Dec 2004 Mw 9.2 rupture offshore Aceh, northern Sumatra, *Earth and Planetary Science Letters*, *263*, 16-31.
Seely, D. R. (1977), The significance of landward and oblique structural trends on trench inner slopes, in *Island arcs deep sea trenches and back-arc basins*, edited, pp. 187-198.

Seno, T., and K. Hirata (2007), Did the 2004 Sumatra-Andaman Earthquake Involve a Component of Tsunami Earthquakes?, *Bulletin of the Seismological Society of America*, *97*(1A), S296-S306.

Shulgin, A., H. Kopp, D. Klaeschen, C. Papenberg, F. Tilmann, E. R. Flueh, D. Franke, U. Barckhausen, A. Krabbenhoeft, and Y. Djajadihardja (2013), Subduction system variability across the segment boundary of the 2004/2005 Sumatra megathrust earthquakes, *Earth and Planetary Science Letters*, *365*, 108-119.

Sibuet, J.-C., C. Rangin, X. Lepichon, S. C. Singh, A. Cattaneo, D. Graindorge, F. Klingelhoefer, J.-y. Lin, J. A. Malod, and T. Maury (2007), 26th December 2004 great Sumatra–Andaman earthquake: Co-seismic and post-seismic motions in northern Sumatra, *Earth and Planetary Science Letters*, *263*, 88-103.

Sieh, K., et al. (2015), Penultimate predecessors of the 2004 Indian Ocean tsunami in Aceh, Sumatra: Stratigraphic, archeological, and historical evidence, *Journal of Geophysical Research: Solid Earth*, *120*(1), 308-325.

Singh, S. C., A. P. S. Chauhan, A. J. Calvert, N. D. Hananto, D. Ghosal, A. Rai, and H. Carton (2012), Seismic evidence of bending and unbending of subducting oceanic crust and the presence of mantle megathrust in the 2004 great Sumatra earthquake rupture zone, *Earth and Planetary Science Letters*, *321-322*, 166-176.

Singh, S. C., H. Carton, A. S. Chauhan, S. Androvandi, A. Davaille, J. Dyment, M. Cannat, and N. D. Hananto (2011), Extremely thin crust in the Indian Ocean possibly resulting from Plume-Ridge Interaction, *Geophysical Journal International*, *184*(1), 29-42.

Singh, S. C., et al. (2008), Seismic evidence for broken oceanic crust in the 2004 Sumatra earthquake epicentral region, *Nature Geoscience*, *1*, 777-781.

Smith, W. H. F., and P. Wessel (1990), Gridding with continuous curvature splines in tension, *Geophysics*, *55*, 293-305.

Smith, W. H. F., and D. Sandwell (1997), Global sea floor topography from satellite altimetry and ship depth soundings, *Science*, *277*, 1956-1962.

Storti, F., R. S. Marin, C. Faccenna, and A. C. Sainz (2001), Role of the backstop-to-cover thickness ratio on vergence partitioning in experimental thrust wedges, *Terra Nova*, *13*, 413-417.

Strasser, M., et al. (2013), A slump in the trench: Tracking the impact of the 2011 Tohoku-Oki earthquake, *Geology*, *41*(8), 935-938.

Strozyk, F., M. Strasser, A. Förster, A. Kopf, and K. Huhn (2010), Slope failure repetition in active margin environments: Constraints from submarine landslides in the Hellenic fore arc, eastern Mediterranean, *Journal of Geophysical Research*, *115*(B8).

Sultan, N., A. Cattaneo, J.-C. Sibuet, and J.-L. Schneider (2009), Deep sea in situ excess pore pressure and sediment deformation off NW Sumatra and its relation with the December 26, 2004 Great Sumatra-Andaman Earthquake, *International Journal of Earth Sciences*, *98*, 823-837.

Sumner, E. J., M. I. Siti, L. C. McNeill, P. J. Talling, T. J. Henstock, R. B. Wynn, Y. S. Djajadihardja, and H. Permana (2013), Can turbidites be used to reconstruct a paleoearthquake record for the central Sumatran margin?, *Geology*, *41*(7), 763-766.

Taira, A., et al. (1998), Thematic Article Nature and growth rate of the Northern Izu-Bonin (Ogasawara) arc crust and their implications for continental crust formation, *The Island Arc*, *7*, 395-407.

Talling, P. J. (2014), On the triggers, resulting flow types and frequencies of subaqueous sediment density flows in different settings, *Marine Geology*, *352*, 155-182.

Tan, E., L. L. Lavier, H. J. a. Van Avendonk, and A. Heuret (2012), The role of frictional strength on plate coupling at the subduction interface, *Geochemistry, Geophysics, Geosystems*, *13*, 1-19.

Tang, G., et al. (2013), 3-D active source tomography around Simeulue Island offshore Sumatra: Thick crustal zone responsible for earthquake segment boundary, *Geophysical Research Letters*, *40*, 48-53.

Tappin, D. R. (2010), Digital elevation models in the marine domain: investigating the offshore tsunami hazard from submarine landslides, *Geological Society, London, Special Publications*, *345*(1), 81-101.

Tappin, D. R., L. C. McNeill, T. J. Henstock, and D. C. Mosher (2007), Mass wasting processes - offshore Sumatra, paper presented at Submarine Mass Movements and their consequences: 3rd International Symposium, Springer.

Tappin, D. R., P. Watts, G. M. McMurty, Y. Lafoy, and T. Matsumoto (2001), The Sissano, Papua New Guinea tsunami of July 1998-offshore evidence on the source mechanism, *Marine Geology*, *175*, 1-23.

Tappin, D. R., S. T. Grilli, J. C. Harris, R. J. Geller, T. Masterlark, J. T. Kirby, F. Shi, G. Ma, K. K. S. Thingbaijam, and P. M. Mai (2014), Did a submarine landslide contribute to the 2011 Tohoku tsunami?, *Marine Geology*, *357*, 344-361.

ten Brink, U. S., H. J. Lee, E. L. Geist, and D. Twichell (2009a), Assessment of tsunami hazard to the U.S. East Coast using relationships between submarine landslides and earthquakes, *Marine Geology*, *264*(1-2), 65-73.

ten Brink, U. S., R. Barkan, B. D. Andrews, and J. D. Chaytor (2009b), Size distributions and failure initiation of submarine and subaerial landslides, *Earth and Planetary Science Letters*, *287*(1-2), 31-42.

Tsuji, T., K. Kawamura, T. Kanamatsu, T. Kasaya, K. Fujikura, Y. Ito, T. Tsuru, and M. Kinoshita (2013), Extension of continental crust by anelastic deformation during the 2011 Tohoku-oki earthquake: The role of extensional faulting in the generation of a great tsunami, *Earth and Planetary Science Letters*, *364*, 44-58.

Turner, D. L., R. B. Forbes, and C. W. Naeser (1973), Radiometric ages of Kodiak Seamount and Giacomini Guyot, Gulf of Alaska: Implications for Circum-Pacific tectonics, *Science*, *182*(4112), 579-581.

Urgeles, R., and A. Camerlenghi (2013), Submarine landslides of the Mediterranean Sea: Trigger mechanisms, dynamics, and frequency-magnitude distribution, *Journal of Geophysical Research: Earth Surface*, *118*(4), 2600-2618.

Völker, D., F. Scholz, and J. Geersen (2011), Analysis of submarine landsliding in the rupture area of the 27 February 2010 Maule earthquake, Central Chile, *Marine Geology*, *288*, 79-89.
von Huene, R. (1972), Structure of the Continental Margin and Tectonism at the Eastern Aleutian Trench, *GSA Bulletin*, *83*, 3613-3626.
von Huene, R. (1979), Structure of the Outer Convergent Margin Off Kodiak Island, Alaska, from Multichannel Seismic Records: Convergent Margins, edited.
von Huene, R., A. Fisher-Michael, and R. Bruns-Terry (1987), Geology and evolution of the Kodiak margin, Gulf of Alaska, in *Geology and resource potential of the continental margin of western North America and adjacent ocean basins, Beaufort Sea to Baja California*, edited, pp. 191-212.
von Huene, R., C. R. Ranero, and P. Watts (2004), Tsunamigenic slope failure along the Middle America Trench in two tectonic settings, *Marine Geology*, *203*, 303-317.
von Huene, R., J. J. Miller, and R. W. Weinrebe (2012), Subducting plate geology in three great earthquake ruptures of the western Alaska margin, Kodiak to Unimak, *Geosphere*, *8*, 628-644.
Von Huene, R., C. R. Ranero, W. Weinrebe, and K. Hinz (2000), Quaternary convergent margin tectonics of Costa Rica, segmentation of the Cocos Plate, and Central American volcanism, *Tectonics*, *19*, 314-334.
von Huene, R., L. D. Kulm, Shipboard, Scientific, and Party (1973), http://www.deepseadrilling.org/18/dsdp_toc. htm, edited, IODP Publications, Last accessed March 7, 2016.
Wang, K., and Y. Hu (2006), Accretionary prisms in subduction earthquake cycles: The theory of dynamic Coulomb wedge, *Journal of Geophysical Research*, *111*, 1-16.
Wang, K., and S. L. Bilek (2011), Do subducting seamounts generate or stop large earthquakes?, *Geology*, *39*, 819-822.
Wang, K., and S. L. Bilek (2014), Fault creep caused by subduction of rough seafloor relief, *Tectonophysics*, *610*, 1-24.
Wang, W., and D. M. Davis (1996), Sandbox model simulation of forearc evolution and noncritical wedges, *Journal of Geophysical Research*, *101*, 11329-11339.
Weinrebe, A., A. Behrmann, J. Hinrich, A. Chadwell, P. Lonsdale, A. D. Sweeney, J. L. Diaz-Naveas, and E. Contreras-Reyes (2010), High resolution seafloor bathymetry of the rupture area "before" and "after" the magnitude 8.8 Chilean earthquake of 2010, paper presented at AGU Fall Meeting 2010.
Wessel, P., and W. H. F. Smith (1991), Free software helps map and display data, *Eos, Transactions American Geophysical Union*, *72*, 441-441.
Wessel, P., and W. H. F. Smith (1998), New, improved version of generic mapping tools released, *Eos, Transactions American Geophysical Union*, *79*, 579-579.